



HAL
open science

Fundamental research using synchrotron X-rays on key technological materials

Xavier Biquard

► **To cite this version:**

Xavier Biquard. Fundamental research using synchrotron X-rays on key technological materials. Materials Science [cond-mat.mtrl-sci]. UGA - Université Grenoble Alpes, 2018. tel-02002058

HAL Id: tel-02002058

<https://hal.science/tel-02002058>

Submitted on 26 Nov 2020

HAL is a multi-disciplinary open access archive for the deposit and dissemination of scientific research documents, whether they are published or not. The documents may come from teaching and research institutions in France or abroad, or from public or private research centers.

L'archive ouverte pluridisciplinaire **HAL**, est destinée au dépôt et à la diffusion de documents scientifiques de niveau recherche, publiés ou non, émanant des établissements d'enseignement et de recherche français ou étrangers, des laboratoires publics ou privés.

**Fundamental research using
synchrotron X-rays on key
technological materials**

Par X. BIQUARD

**Soutenance de HDR effectuée
le mardi 23 octobre 2018 à 14 h**

Jury :

Olivier Thomas — rapporteur

Hubert Renevier — rapporteur

Gilles Patriarche — rapporteur

Bérangère Hyot — examinatrice

**René Guinebretière — examinateur –
président du jury**

Table of Contents

Introduction	1
I Phase-change materials	2
I.1 EXAFS	2
I.1.1 Physical effects	2
I.1.2 Origin of the EXAFS signal	3
I.1.3 Formalism	4
I.1.3.1 EXAFS Formula	4
I.1.3.2 Necessary hypothesis for EXAFS data adjustment	5
I.2 Properties and importance of PCM	6
I.2.1 Commutation	6
I.2.2 Congruence	6
I.2.3 Importance	7
I.3 Commutation speed	8
I.3.1 Study of GeTe	8
I.3.1.1 Amorphous GeTe	8
I.3.1.1.1 At the Te K-edge	8
I.3.1.1.2 At the Ge K-edge	9
I.3.1.1.3 Overall view of amorphous GeTe	10
I.3.1.2 Crystalline GeTe	10
I.3.1.2.1 Diffraction data	10
I.3.1.2.2 EXAFS data	11
I.3.1.2.3 β -GeTe phase does not exist! order-disorder transition	12
I.3.1.3 Structural changes during amorphous/crystalline cycle	13
I.3.2 Study of GST = $\text{Ge}_2\text{Sb}_2\text{Te}_5$	13
I.3.2.1 Amorphous GST	13
I.3.2.2 Crystalline GST	14
I.3.2.3 Structural changes during amorphous/crystalline cycle	15
I.3.3 Conclusion	15
I.4 Super-resolution effect with InSb	15
I.4.1 Experimental conditions	16
I.4.2 Results	17
I.4.2.1 50 nm InSb: test study	17
I.4.2.2 20 nm InSb with ZnS-SiO ₂	17
I.4.2.3 20 nm InSb with ZrO ₂	18
I.4.2.4 Best super-resolution effect	18
II The μLaue setup	19
II.1 The first setup	19
II.1.1 Presentation	19
II.1.2 Copper interconnects problematic	20
II.1.3 Camera calibration	20
II.2 Measurements on copper line	22
II.2.1 1 μm wide copper line	22
II.2.2 260 nm wide copper line	23
II.2.3 Conclusion	24

II.3 Upgraded setup	24
III High-performance IR detection	26
III.1 Introduction to IR and HgCdTe	26
III.2 Extrinsic p-type doping	27
III.2.1 As implantation	28
III.2.2 Diffraction specificities	28
III.2.3 As-implanted and annealed μ Laue results	29
III.3 Strain	31
III.3.1 Stretching the μ Laue to its limits	32
III.3.1.1 CCD positioning	32
III.3.1.2 Optimised fitting routine on asymmetrical peak	32
III.3.1.3 Sample positioning	33
III.3.1.4 Camera calibration	34
III.3.1.5 The latest tweaks to achieve 10^{-5} resolution	34
III.3.2 Validation of our strain measurement method	35
III.3.3 Sb-doped and annealed sample	37
III.4 Local orientation	38
III.5 Overall comparison between local strain and orientation	40
IV Research perspectives	43
IV.1 Technical developments to study the relaxed zone	43
IV.2 Defect-free and dislocation zones study	44
IV.2.1 MBE samples: fundamental research oriented	45
IV.2.2 LPE samples: applied research oriented	47
CONCLUSION	50
Bibliography	51
Index of Tables	54
Illustration Index	55

Introduction

While writing this HDR manuscript, I took the opportunity to look back on my professional carrier to realise I had conducted numerous studies of fundamental research using different synchrotron techniques. I think I am fundamentally curious and therefore I like to discover new or emerging fields of research since it challenges my understanding and possesses a large exploration aspect. As a consequence, I am not a specialist dedicated to one field of research but I develop collaboration with various groups: I've been working on a wide range of research fields, each research field being linked to the problematic of the group I develop collaboration with. And looking back on those years, I noticed that in my collaborations, my contribution was always to provide understanding of key technological material under development, hence the title of this manuscript.

Despite it will not be fully developed in this manuscript, there was also a very nice engineering aspect to my career since I have significantly contributed to the construction of two French beamlines at ESRF. From 1999 to 2003, I help built the forth French CRG beamline at ESRF named BM30B-FAME (French Absorption spectroscopy beamline in Material and Environmental sciences) with the complete definition of required beamline characteristics for EXAFS studies on diluted systems (<10 ppm), as well as its components tuning once operational. From 2004 to 2012, I help refurbish the historical first French CRG beamline at ESRF BM32-IF (InterFace) with full re-definition and construction of all beamline optical elements as well as the development of the first European whitebeam (4-40 keV) of submicronic size and its dedicated μ Laue station for which I will give some details.

Thanks to these two beamlines, I was able to become competent in two emblematic synchrotron techniques that are EXAFS and white beam Laue microdiffraction. Emblematic since they require a continuously adjustable and very bright X-ray energy on a very broad energy range, a challenge only synchrotron may take up.

Among all my collaborations, two of them were really long-term collaborations and I choose to present them with some details. The first long-term collaboration is the object of chapter 'I-Phase-change materials', was dedicated to the study of phase-change materials, covers the 1999→2012 period and makes extensive use of the EXAFS technique. The second long-term collaboration is presented chapter 'III-High-performance IR detection', is dedicated to IR material, covers the 2006→2018 period, is still ongoing and makes extensive use of the white beam Laue microdiffraction detailed into part 'II-The μ Laue setup'.

And finally, because research appears to me as an exciting never-ending journey into wonderland, I will expose in part 'IV-Research perspectives' some of my research perspectives.

I Phase-change materials

In this chapter, I will detail several studies that were conducted on phase-change materials and make extensive use of EXAFS. They were conducted during a 13-year long 1999→2012 fruitful collaboration with Bérangère Hyot from CEA/LETI: PhD thesis of B. Hyot [1], JC Bastien [2] and A. Bastard [3] were successfully defended using presented results as well as the HDR of B. Hyot mid-2011.

A phase-change material (PCM hereafter) is a material that can be reversibly commuted between amorphous and crystalline phases. To this reversible phase change corresponds a large variation in both optical and electrical properties of the material, leading to a large optical and electrical contrast. The most well-known PCM are chalcogenide material (Mendeleev group VIA elements) like bulk Te. Studied since the 50s ([4], [5]), a huge outburst of interest occurred around 1985 [6] (kind of arbitrary date) where it was discovered that mixing the chalcogenide Te with Ge and Sb, stabilises its amorphous phase at RT, enables fast crystalline-to-amorphous commutation in the 100 ns range with physical property contrast withstanding at least 10^6 cycles.

This had far-reaching implications and gave birth to revolutionary CD-RW and DVD-RW in the 90's. At present time, PCM are studied as an alternative for world-wide used flash-memory¹ to overcome flash specific downscaling difficulties. Indeed, Phase-change Random Access Memory (PRAM) is a promising candidate [7] for a kind of universal memory that combines three main qualities: the high speed of Static Random Access Memory (SRAM), the non-volatile nature of Flash-memory and the density of Dynamic Random Access Memory (DRAM). In July 2015, major microelectronics actors Intel and Micron Technology announced the 3D Xpoint, a non-volatile memory technology based on PCM. And recently in July 2017, 3D XPoint Solid State Drive (SSD) comes to the client and consumer market in the form of the Intel Optane SSD, a product made of 20 nm 3D Xpoint PCM that is so fast, it may even be used as memory [8], [9]!

I.1 EXAFS

EXAFS (Extended X-ray Absorption Fine Structure [10]) is an emblematic synchrotron technique since it requires a continuously adjustable X-ray energy on a very broad range, a challenge only synchrotron may take up. Less known than diffraction, EXAFS possesses two intrinsic features missing to diffraction. First it has chemical selectivity and information is selectively gathered on the different chemical element constituting the material, a great asset when studying separately components of alloys or the effect of doping. And secondly, it works on any type of condensed matter should it be liquid, amorphous or crystalline and is therefore particularly suited to study PCM which reversibly commute between amorphous and crystalline phases.

More precisely, EXAFS consists in recording the sample's absorption coefficient as a function of photon energy around the ionisation energy of one of the sample's chemical element. EXAFS chemical selectivity stems from the choice of the ionisation energy, and typically EXAFS requires a continuously adjustable energy on a large range of 1 keV around an ionisation energy that varies from 4 to 40 keV for elements heavier than Calcium. EXAFS gathers information on a short-range (while diffraction on a long-range) and provides the average *local* chemical environment around the studied chemical element, with a sensitivity range of typically 7 Å at room temperature (RT).

I.1.1 Physical effects

If we consider an incoming photon of energy E greater than the ionisation energy E_0 of one of the sample's chemical element, absorption occurs and a photo-electron of energy $E-E_0$ is ejected. As core electrons are ejected from the absorbing atom (1s electrons for K-edge absorption or 2s/2p electrons for L-edge), the hollow ion will very quickly decay (picoseconds time scale [11]) either with non-radiative Auger or cascade radiative processes from higher-energy occupied electronic

¹ Flash is a diminutive for Flash-erasable EEPROM (Electrically-Erasable Programmable Read Only Memory). First demonstration was conducted by Toshiba in 1984: electric charges are stored inside a single poly-silicone floating gate sandwiched between control and tunnelling oxides.

levels given rise to several fixed-energy fluorescence lines. If the sample is transparent enough, absorption coefficient will be measured thanks to the transmitted intensity. But in our case, substrate is much too thick compared to the active layer to allow any meaningful measurement with transmission. Therefore, we will use an energy-resolved X-ray detector that will measure a chosen fixed-energy fluorescence line intensity: its ratio to the incident intensity will be the sample's absorption coefficient.

The resulting spectra (from [12]) is represented in figure 1. The absorption jump is clearly visible but it is not a simple step function as could be expected. Clearly, after the edge, there is an oscillatory component superimposed on a slowly decreasing and smooth baseline: this oscillatory component constitutes the EXAFS signal and starts roughly 50-100 eV after the edge E_0 . E_0 is usually evaluated as the inflection point of absorption edge situated near the middle height.

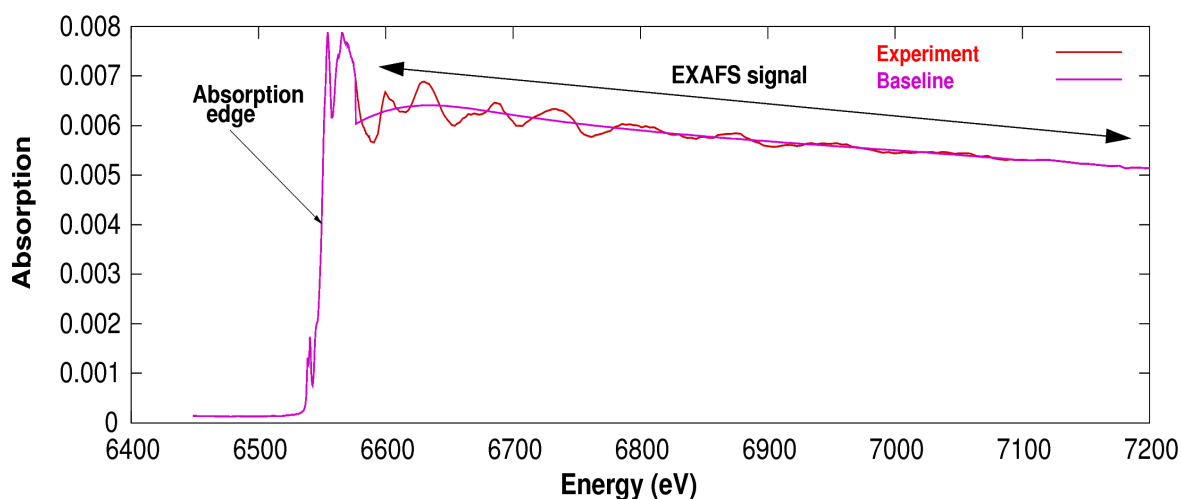


Figure 1: Example of recorded EXAFS spectra (K-edge of Mn)

I.1.2 Origin of the EXAFS signal

Understanding the origin of the EXAFS signal will teach us capacities and limitations of the EXAFS technique. First of all, no EXAFS signal is visible for gazes: EXAFS specifically characterises locally ordered environment. And in a locally ordered environment, the ejected photo-electron of energy $E-E_0$ will bump into neighbouring atoms. In an analogy, each absorbing atom of the sample is converted into an omnidirectional active radar (figure 2):

- the wave associated to the photo-electron will be backscattered by neighbouring atoms
- the returning echo will interfere with the emission
- and results in a modulation of the studied chemical element's absorption.

This modulation (EXAFS) « senses » the environment: phase-shift and intensity of the echo both depend on the distance but also on the size (chemical nature) and number of backscatterers. EXAFS signal is therefore a sum of sinusoids, each sinusoid being characteristic of a single shell regrouping all backscatterers of the same chemical nature and at the same distance.

EXAFS is a very versatile technique since any kind of locally ordered material is suited (crystalline, polycrystalline, amorphous, liquid, protected surface, multi-layered, quantum dots, wires ...) and it has the capacity to determine the surrounding shells of the absorbing atom. This capacity has a limited range though since the shell echo intensity strongly diminishes with distance d : to the classical $1/d^2$ damping effect from geometric consideration, one must add the thermal vibration effect which causes incoherence between echoes of individual atoms constituting the same shell, thus damping them.

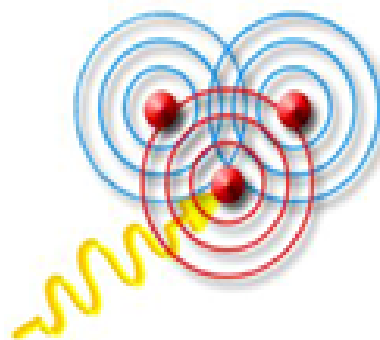


Figure 2: The radar effect: once incident photon (yellow) is absorbed, ejected photo-electron wave (red) is backscattered (blue) by neighbouring atoms and interferes with emission thus modulating the absorption.

I.1.3 Formalism

I.1.3.1 EXAFS Formula

As EXAFS signal is constituted by the sum of several sinusoids — each being characteristic of a single backscattering shell — a Fourier transform (FT) is applied on the EXAFS signal to separate contribution from individual backscattering shell. This FT is taken on the largest possible range of k value as limited by recorded data quality, where $k(\text{\AA}^{-1})$ is the photo-electron wavenumber

$$k = \frac{\sqrt{2m(E - E_0)}}{\hbar}$$

To avoid FT artefacts arising from a limited k -range, k limits are taken at

EXAFS signal zero-crossings and a smooth apodization function is applied. Traditionally, the EXAFS signal itself is presented alongside with the modulus of the FT, see figure 3. This graph perfectly illustrates all the interest of the EXAFS technique. Simply taking the modulus of the FT of the EXAFS signal previously shown on figure 1 renders backscattering shells visible: in our example, the seven first shells become clearly visible under the form of seven distinct bumps!

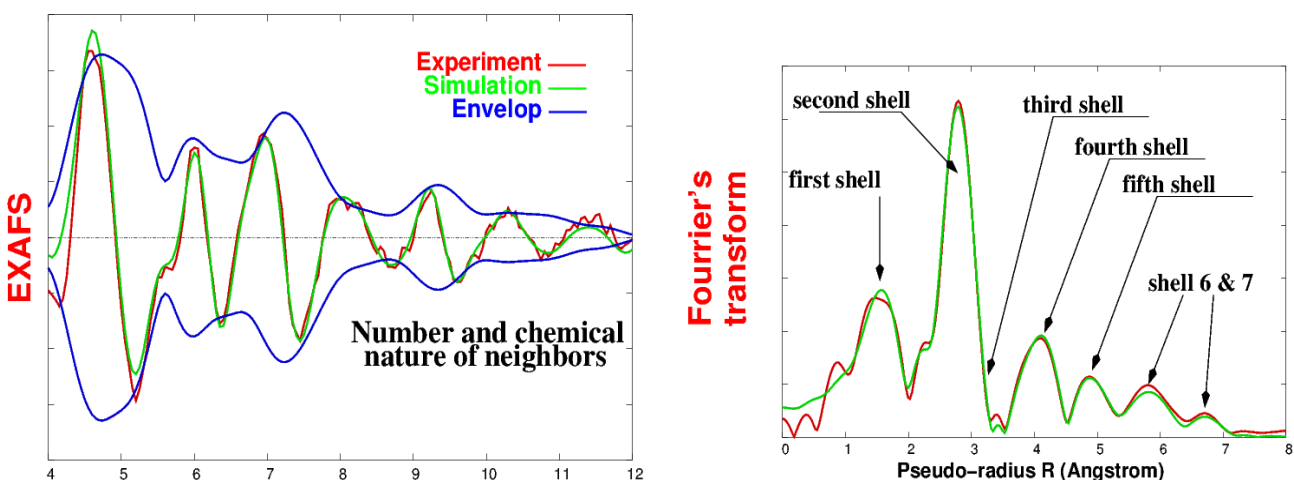


Figure 3: Recorded EXAFS spectra (here 2% Mn dopant inside GaN) along with the modulus of its FT. Comparison of experiment with data simulation is also provided

On the right of figure 3, we observe the absence of signal below 1 Å. This is a logical finding since atoms are roughly of this size: no neighbour may be that close. And indeed this property is used to determine the smooth decreasing baseline for EXAFS oscillation extraction: baseline minimises residual contribution in the low $R < 1$ Å range, a property implemented in the ATHENA software [13] used to extract EXAFS signal.

Let us now derive simply the EXAFS formula:

- Sensitivity to distance is the major strength of EXAFS. Let “ R_i ” be the distance between the absorbing atom and “ N_i ” backscatterers “ i ” of the same chemical nature forming shell “ i ”. EXAFS signal will be the sum of “ $N_i \sin(2kR_i)$ ” sinusoids. The farther away is “ i ”, the smaller the oscillation period.
- For interference to occur, a certain degree of coherence must be kept between emitted and backscattered wave: the farther away the backscatterer, the less coherence. If “ $\lambda(k)$ ” is the photoelectron mean free path (it is not the photoelectron wavelength), EXAFS oscillations are damped by an “ $\exp(-2R_i/\lambda(k))$ ” factor. This damping washes out high- k oscillations compared to low- k ones. To compensate for it and therefore equilibrate oscillation intensities on the whole k range, EXAFS is usually weighted by a factor k or k^2 . It may be k^3 -weighted for high- k part study or not weighted when only the low- k part is relevant.
- Speaking of coherence, thermal motion will make “ R_i ” a distribution of distance thus weakening even more coherence. If thermal motion is small and Gaussian, it may be demonstrated that EXAFS oscillations are damped by “ $\exp(-2k^2\sigma_i^2)$ ” where “ σ_i ” is the Debye-Waller (DW) factor. As a generalisation, “ σ_i ” incorporates all sources of “ R_i ” distribution like structural disorder for example.

- As each sinusoid is specific to a dedicated shell “i”, amplitude and phase of sinusoid depends on the chemical nature of the backscatterers constituting the shell. Indeed, as the photo-electron goes through the electronic clouds of absorbing and backscattering atoms, its wave undergoes a phase-shift “ $\delta_i(k)$ ” and is backscattered with an amplitude “ $t_i(2k)/k^2$ ” depending on the “size” of the backscatterer².

Putting now all contributions together, we get the classical (single scatterer approximation) EXAFS oscillation $\chi(k)$ formula:

$$\chi(k) = S_0^2 \sum_{\text{shell } i} N_i \frac{t_i(2k)}{k^2 R_i^2} \exp(-2k^2 \sigma_i^2) \exp\left(\frac{-2R_i}{\lambda(k)}\right) \sin(2kR_i + \delta_i(k))$$

where “ S_0^2 ” is a constant (usually fixed at 0.8) called the reduction factor that reflects EXAFS damping by spectator electrons. All data treatment were conducted using the well-known and extensively used Artemis [13] and Iffeffit software suite [14].

I.1.3.2 Necessary hypothesis for EXAFS data adjustment

As the EXAFS formula shows, before any adjustment to data can be made, “ $t_i(2k)$ ” and “ $\delta_i(k)$ ” must be determined: the chemical nature of every shell must be fixed. **Therefore, EXAFS data adjustment requires making the fundamental assumption of a spatial arrangement around absorbing atom and then checks if the foreseen spatial arrangement is coherent with experiment.**

Once the spatial arrangement defined, “ $t_i(2k)$ ” and “ $\delta_i(k)$ ” are calculated using world-reference FEFF6-FEFF8³ programs. Data adjustment then consists in fitting the 3 parameters “ N_i ”, “ R_i ” and “ σ_i ” for each shell. We also use a supplementary global parameter “ ΔE_0 ” which represents the energy offset between the first-principle calculated Fermi level of the *neutral* absorbing atom and the measured E_0 of an eventually charged absorbing atom.

To make a reasonable assumption on the spatial arrangement, the simplest case occurs when we possess a model for this spatial arrangement like the elementary lattice for a crystal for example. If no model is available, oscillation maximum intensities with k will indicate if backscatterers are rather light, medium or heavy (see footnote 2). An information combined with the fact that only certain chemical elements are present in the sample, that may well determine the nature of the backscatterers.

Finally, EXAFS data adjustment requires 1 global + 3 parameters per shell, and gathers a great number of informations: the chemical nature of the neighbours ($\Delta Z \geq 2^4$), their number ($\pm 10\%$) as well as their distances ($\pm 1\%$) for each and every shell. And also an evaluation of the absorbing atom degree of oxidation thanks to the “ ΔE_0 ” energy shift from neutral atom.

2 As sinusoid of shell “i” is affected by a phase-shift “ $\delta_i(k)$ ”, its |FT| maximum will not be at “ R_i ” but at a lower R value: abscissa of |FT| graph is therefore labelled pseudo-radius $R(\text{\AA})$, not radius $R(\text{\AA})$ (right of figure 3). Concerning amplitude “ $t_i(2k)$ ”, we note that its maximum tends to follow the weight of the backscatterer: at low k for light element and at high k for heavy elements.

3 FEFF6/FEFF8 are world-reference ab initio XAFS simulation programs. They specifically include multiple-scattering since — in the case of a well-ordered environment — the photoelectron may describe a trajectory where it is multiply backscattered from different backscatterers (same or different nature or shell) before returning to absorbing atom. Moreover, shadowing or enhancing effect that occurs when a shorter distance atom is situated between absorbing atom and backscatterer are taken into account.

4 It occurs that the backscattering properties of 2 atoms having $\Delta Z=1$ are too similar to be distinguished

I.2 Properties and importance of PCM

I.2.1 Commutation

The beauty of the commutation principle lies in its simplicity as shown on figure 4: obtaining either amorphous or crystalline phase is as simple as delivering a single heat pulse (using either laser or electrical power).

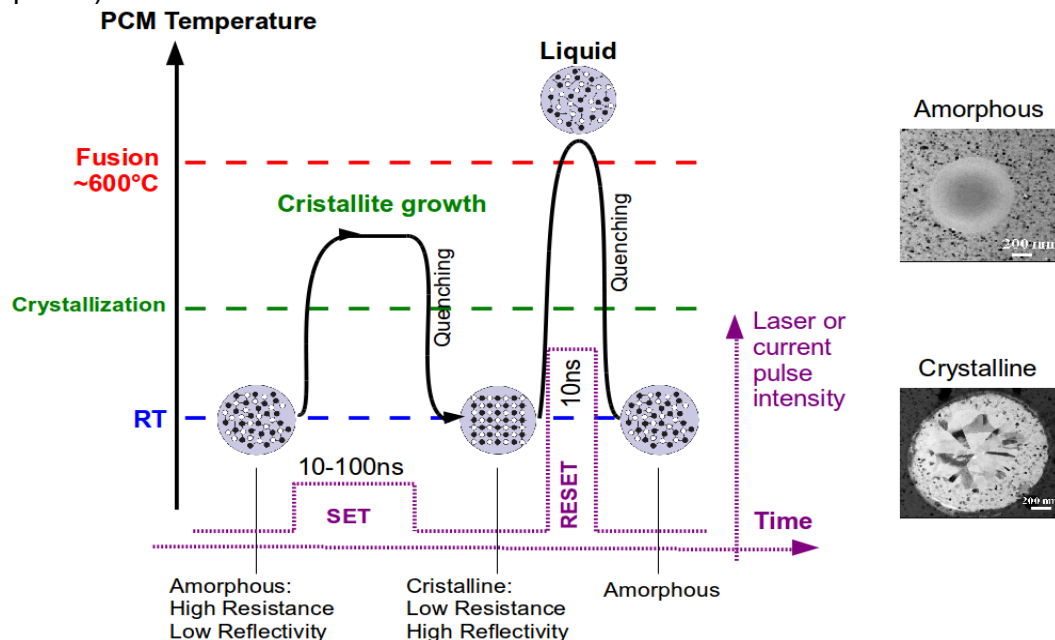


Figure 4: PCM commutation mechanism principle

The trick is to permanently connect the PCM to a (passive) heat sink so that thermal quenching will follow the heat pulse. If the heat pulse is intense enough (RESET pulse), PCM temperature rises above fusion temperature, PCM becomes liquid and subsequent thermal quenching freezes it as an amorphous glass phase. If the heat pulse is of medium intensity (SET pulse) and lasts long enough, PCM temperature rises above crystallisation temperature, crystallites are given some time to grow and subsequent thermal quenching freezes it as a (poly)crystalline phase.

I.2.2 Congruence

To be interesting, a PCM must withstand a very high number (typically $> 10^6$) of phase commutations while keeping stable properties. Therefore, interesting PCMs are congruent: their liquid stoichiometry is identical to the solid one. And any deviation from congruence will result — after a sufficient number of commutations — in a congruent stoichiometry with excess elements being segregated. In the ternary Ge:Sb:Te diagram (see figure 5), the two main congruent stoichiometries are GeTe and Sb_2Te_3 and therefore GeSbTe phase-change alloys were mainly studied along the pseudo-binary line GeTe- Sb_2Te_3 . Along this line, $Ge_2Sb_2Te_5$ is the reference composition since it has the highest possible crystallisation temperature and will be noted GST hereafter. References [15] and [16] provide nice review articles on all significant PCM alloys.

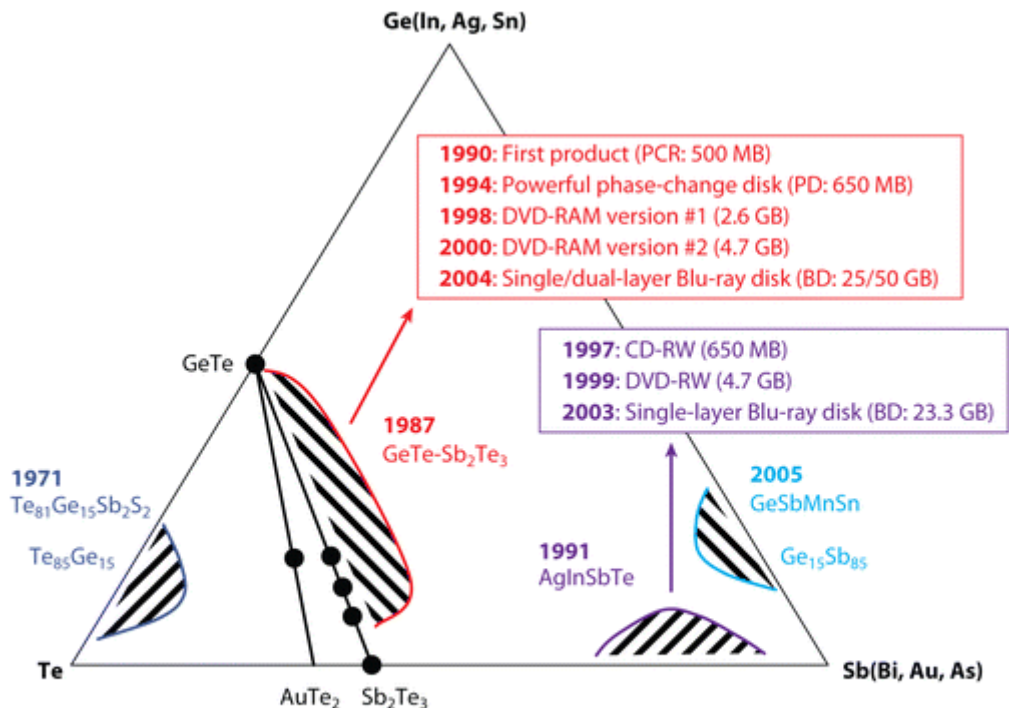


Figure 5: Ternary phase diagram depicting different phase-change alloys, discovery year and use in different optical storage products

1.2.3 Importance

As shown on figure 5, PCM alloys are of utter-most importance in our world. Using a laser to probe the optical contrast and commute between amorphous and crystalline phase, PCM alloys constitute the active layer of all *rewritable* optical storage products: yesterday's first-generation products CD-RW (650MB), second-generation products like DVD-RW (4.7Gb) and nowadays third-generation single/double-layer Blu-ray Disk products (25/50Gb). At each generation, a jump in media capacity occurs while the surface of the product stays roughly the same: data is stored with smaller minimum data mark length, track pitch and laser wavelength, see figure 6.

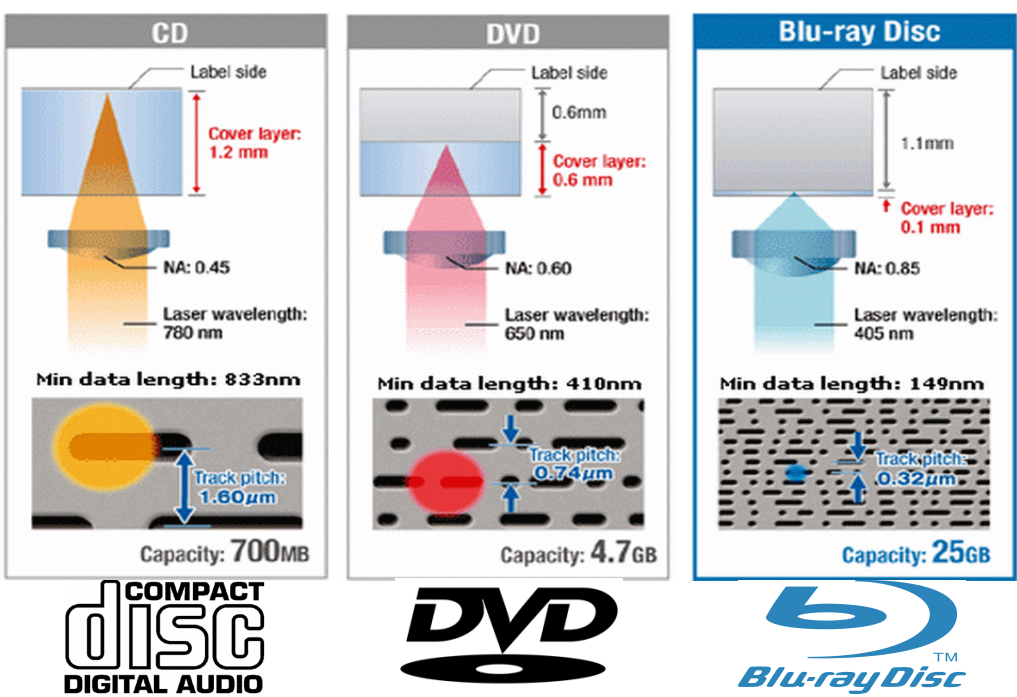


Figure 6: Comparison of optics, recording densities, capacities and disk structures used for CD, DVD and BD. Recording density increased by a factor of 7 going from CD to DVD (2.8 Gb/in²) and a factor 5 going to BD (14.7 Gb/in²). Active PCM layer is 20 nm thick.

I.3 Commutation speed

In year 2001, the situation in the optical storage data field was quite paradoxical since GST was used for commercially available DVD-RW media but the structure of the amorphous phase remained mostly unknown, as well as structural changes taking place inside the material during phase change. It was also unknown why GST commuted in the 100 ns range while GeTe commuted in the 300 ns range [6], [17] and [18]. To address both issues, we needed to be able to characterise the structure of a PCM layer in both its crystalline and amorphous states: EXAFS was naturally chosen.

For these precursory studies [19], 300 nm amorphous layer of GeTe or GST were deposited by magnetron sputtering on a glass substrate and were eventually made crystalline by laser annealing. EXAFS studies were conducted in 2001 on BM29 at ESRF at the K-edge of Ge (11103 eV), Sb (30491 eV) and Te (31814 eV). Sample was put at low incidence to increase the X-ray trajectory length inside PCM layer, thus increasing X-ray absorption. X-ray footprint was several cm^2 .

In a real DVD, amorphous phase is obtained by quenching the melt phase and is therefore called "melt-quenched". It is made of a series of amorphous spots (less than $\varnothing 1 \mu\text{m}$) on a crystalline surface: with a several cm^2 footprint, X-ray beam will necessarily cover both melt-quenched and crystalline zones. So, to avoid any crystalline / amorphous mixing, we will study the continuous amorphous phase that is naturally created when making the deposit, called "as-dep" (as deposited). And it is reasonable to assume as-dep and melt-quench amorphous PCM are not too much different since sputtered ion impact causes a local temperature increase.

I.3.1 Study of GeTe

We will first focus on amorphous GeTe and I will detail the complete EXAFS analysis procedure including qualitative aspects that suggest spatial arrangement around absorbing atom, oxidation contamination removal using inverse Fourier transform and quantitative data adjustment.

I.3.1.1 Amorphous GeTe

I.3.1.1.1 At the Te K-edge

Data recorded at the Te K-edge are shown in figure 7. Clearly, a single major frequency dominates EXAFS oscillations $k\chi(k)$ and indeed a single bump is visible on $|\chi(R)|$ around pseudo-distance $R=2.2 \text{ \AA}$.

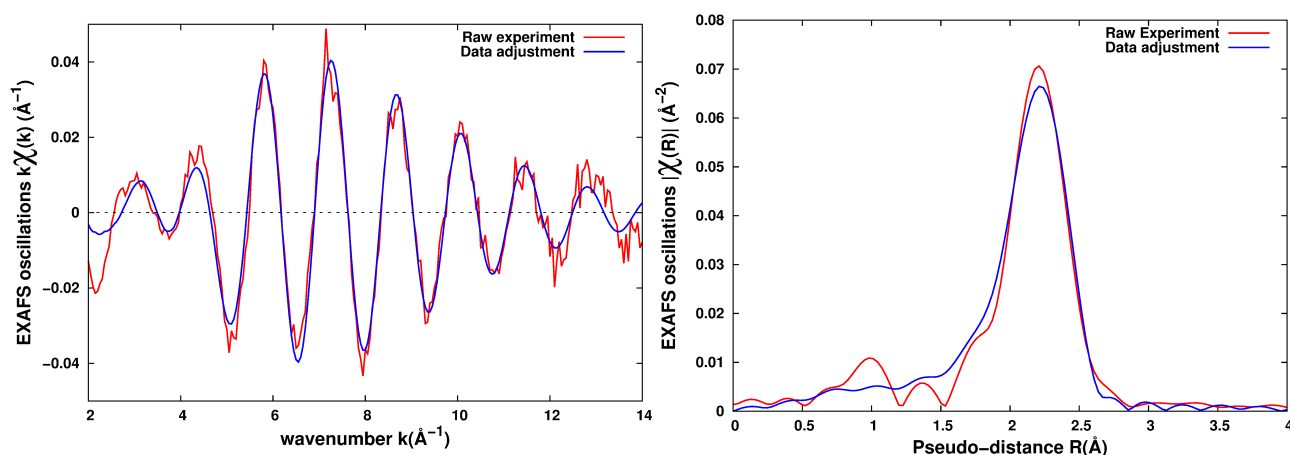


Figure 7: Data adjustment (blue) of amorphous GeTe EXAFS (red) at the Te K-edge

This is a logical finding for amorphous material: ordering does not expand beyond first shell and therefore EXAFS signal originates from first shell only. This property makes of EXAFS a technique of choice for amorphous material. As $k\chi(k)$ amplitude is made of a single large bump at high- k (around 7 \AA^{-1}), the first shell is only constituted of a single type of medium or heavy backscatterer:

a logical finding since GeTe is made of medium Ge ($Z=32$) and heavy Te ($Z=52$) elements. To distinguish between Ge and Te as backscatterer, we have calculated backscattering amplitudes shown on figure 8: the heavier the backscatterer, the higher the k value for the amplitude maximum. As maximum amplitude for Te-Ge is around 7 \AA^{-1} , data adjustment could be successfully conducted using only Ge as backscatterer as shown on figure 8 (blue curve) with numeric adjustment values detailed on table 1:

Amorphous GeTe at Te K-edge, data adjustment conducted on $R \in [1.6-3.4] \text{ \AA}$						
Overall				Ge backscatterer		
r-factor of fit (%)	ΔE_0 (eV)	k-range (\AA^{-1})	k-weight	Num	Distance (\AA)	σ^2 (10^{-3} \AA^2)
1.4	-0.79 ± 0.95	[2.5-14]	1	2.16 ± 0.18	2.61 ± 0.005	6.30

Table 1: Data adjustment of amorphous GeTe at Te K-edge. r-factor of fit indicates a good quality data adjustment. ΔE_0 range of value includes 0 eV, which is perfectly reasonable for neutral Te.

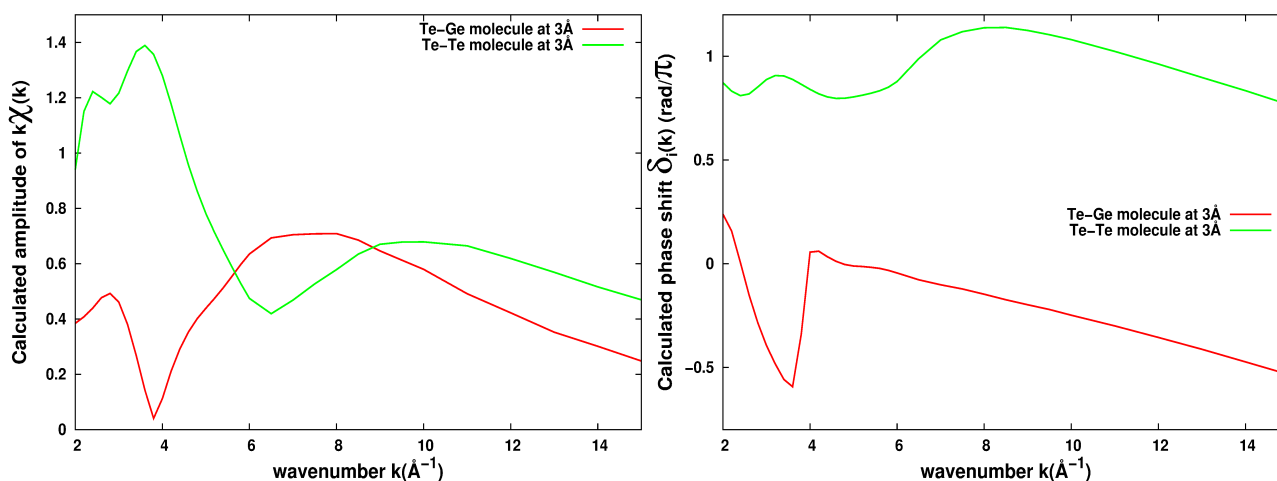


Figure 8: Calculated backscattering amplitude and phase-shift of Ge and Te as backscatterer for Te. For a meaningful comparison, the same 3 \AA distance was chosen for the two backscatterers.

1.3.1.1.2 At the Ge K-edge

Figure 9 shows recorded EXAFS signal at the Ge K-edge. In contrast, with the Te K-edge, the

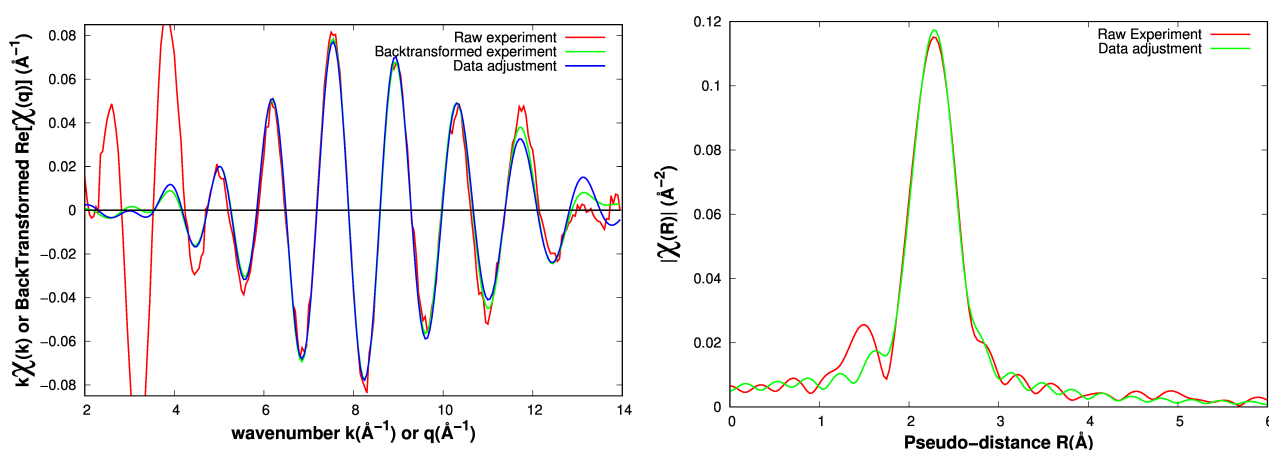


Figure 9: Check of the data adjustment (blue) of amorphous GeTe back-transformed EXAFS (green, $R \in [1.8-3.9] \text{ \AA}$) at Ge K-edge. Original signal (dashed) displayed for comparison.

$k\chi(k)$ amplitude is made of two bumps: an intense and thin first one with maximum at low- k ($\#2.5 \text{ \AA}^{-1}$) and a second large one with maximum at high- k ($\#8 \text{ \AA}^{-1}$). Finding a first thin and intense bump at low- k is characteristic of a lightweight backscatterer which is quite surprising since there should only be medium Ge or heavy Te in GeTe. This clearly indicates a contamination of GeTe with a lightweight element, probably an oxidation (GeO_2) given the natural affinity of Ge for oxygen.

As O has a small ionic radius and high electronegativity — generally speaking — oxides are short bound molecules: oxide contribution falls in both low-R/low-k domains. In contrast, Ge and Te are medium/heavy atoms, their ionic/covalent radius are large and first Ge/Te shell will be at greater distance giving rise to the main peak around the pseudo-distance $R=2.3$ Å. Fitting oxide raises by four the number of parameters: the three usual ones (number, distance, DW factor) plus a dedicated ΔE_0 since oxides are ionised species. Thus, it is best to suppress the oxide contribution. To achieve this selection, we simply conduct data adjustment on the Fourier back-transformed (FT^{-1}) EXAFS oscillations (noted $\chi(q)$) calculated on a reduced R range, [1.8-3.9] Å in this case. Data adjustment is of good quality as shown in table 2 and FT^{-1} has efficiently left out the oxide contribution that is visible as a thin low-k bump on figure 9.

Amorphous GeTe at Ge K-edge, data adjustment conducted on FT^{-1} with $R \in [1.8-3.9]$ Å									
Overall				Ge backscatterer			Te backscatterer		
r-factor of fit (%)	ΔE_0 (eV)	k-range (Å^{-1})	k-weight	Num	Dist (Å)	σ^2 (10^{-3}Å^2)	Num	Dist (Å)	σ^2 (10^{-3}Å^2)
0.13	1.29 ± 2.11	4.25- 13.75	1	1.02 ± 0.15	2.47 ± 0.008	1.94 ± 1.3	1.14 ± 0.19	2.64 ± 0.018	5.0 ± 1.2

Table 2: Data adjustment of amorphous GeTe at Ge K-edge. r-factor of fit indicates a good quality data adjustment. ΔE_0 overall value of 1.29 ± 2.11 eV is coherent with neutral Ge.

1.3.1.1.3 Overall view of amorphous GeTe

In addition to GeTe, we found that a Germanium oxide was probably present but no Tellurium oxide. Using the Rutherford BackScattering (RBS) technique, we measured a $\text{Ge}_{53}\text{Te}_{47}$ stoichiometry on deposited GeTe: it is probable that excess Ge from congruent $\text{Ge}_{47}\text{Te}_{47}$ stoichiometry has segregated [20] and was oxidised. Finally, we found that Ge is roughly 1 time coordinated with Ge at 2.47 Å and with 1 Te at 2.64 Å, while Te is 2 times coordinated to Ge at 2.61 Å, a distance coherently close to 2.64 Å.

It may seem strange that the Te environment with its 2 Ge does not respect the GeTe 1:1 stoichiometry. If stoichiometry binds crystal primary cell because crystals are made of a 3D replication of the primary cell, it is not the case for amorphous material where only first neighbours are defined. For example, we could view amorphous GeTe as a random superposition of roller chains made with flexible (and stoichiometric) Te-Ge-Ge-Te links, Te from one link being bound to the Ge of the next link.

These results contrast with liquid GeTe studies ([21] and [22]) where Ge and Te are found to be 4 times coordinated but in these studies, only Ge-Te bonds are assumed, no Ge-Ge bonds ... Clearly, the amorphous phase cannot be seen as a freezed liquid and our study shows that taking into account Ge-Ge bonds is the key parameter to understand the local environment in amorphous GeTe.

1.3.1.2 Crystalline GeTe

1.3.1.2.1 Diffraction data

Crystals are naturally studied using diffraction which has determined the GeTe phase diagram ([23] and [24]) shown in figure 10. There are two possible crystalline phases for GeTe depending on the temperature: a rhombohedral phase called α -GeTe which is stable at RT and a cubic phase of the NaCl type called β -GeTe which is stable at high temperature above $T_{\alpha-\beta}=705 \text{ K}=432^\circ\text{C}$ [25]. Rhombohedral phase α -GeTe corresponds to a cubic β -GeTe that has been elongated along its diagonal with an off-centre displacement of the inner atom along the same direction, see figure 11. In DVD, crystalline phase is obtained by quenching a crystalline phase that has grown *during* the heat pulse where temperature is high. Therefore, the DVD crystalline phase — even measured at RT — is probably the β -GeTe phase, not the RT stable α -GeTe phase. But experiments will surprisingly prove this is wrong!

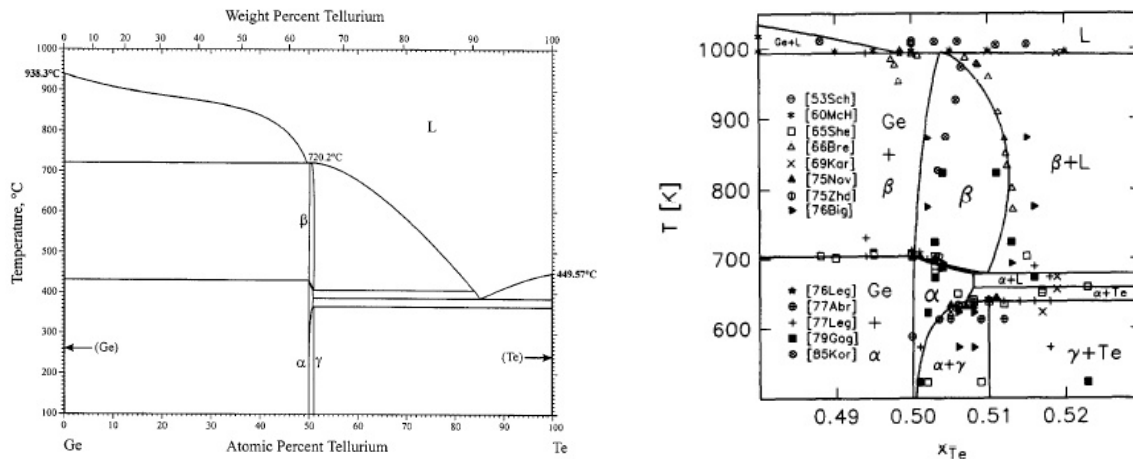


Figure 10: Ge-Te phase diagram with detailed view around congruent $Ge_{50}Te_{50}$ stoichiometry

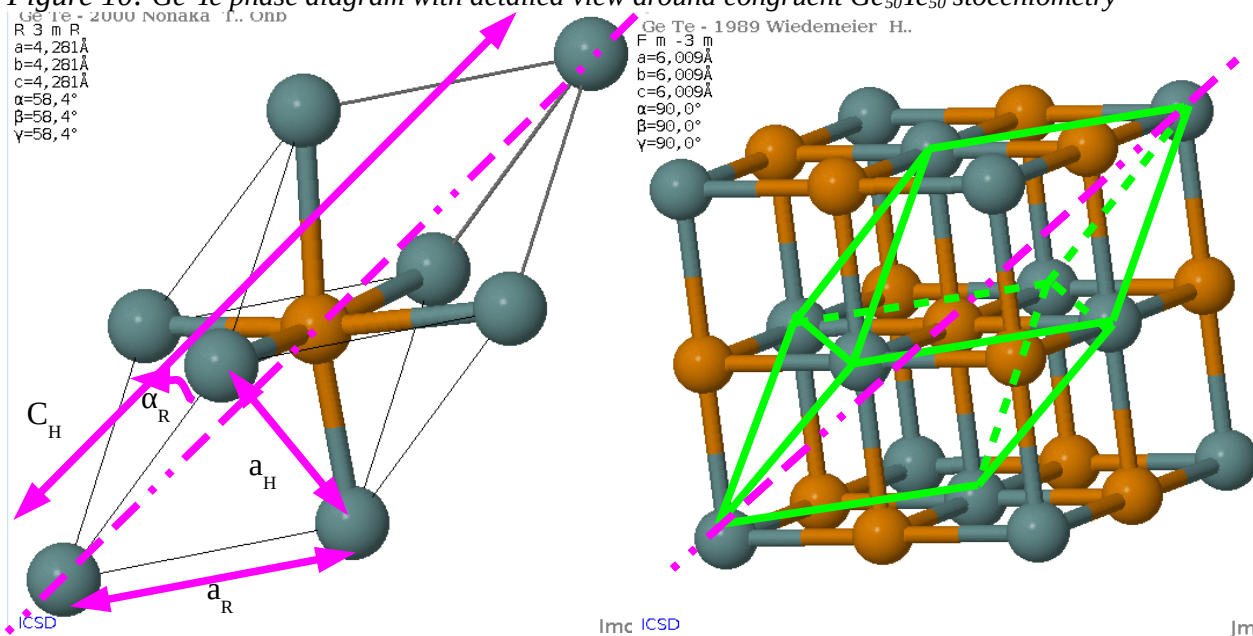


Figure 11: Left: α -GeTe (RT) rhombohedral unit cell with rhombohedral parameter (subscript R) and corresponding hexagonal ones (subscript H). Right: β -GeTe (HT) classical cubic four cfc unit-cell structure, with corresponding rhombohedral unit cell in green.

1.3.1.2 EXAFS data

Recorded EXAFS spectra are of poor signal-to-noise ratio because it appears that shell contributions are badly separated, as if EXAFS oscillations were broadened. We believe this indicates that crystalline GeTe suffers from a large structural disorder. Consequently, EXAFS could only be used to check whether α -GeTe or β -GeTe is obtained, not to precisely determine the characteristics of shells around absorbing atom. Moreover, we have concentrated on the first shell only and in order to maximise its contribution, the Ge K-edge was studied since the heaviest backscatterers are Te. In the case of β -GeTe, we have a cubic crystal of the NaCl type [25]: there are 6 equidistant 3.000 Å GeTe bonds. $|\chi(R)|$ of first shell is expected to show a single intense contribution around pseudo- $R \approx 2.8$ Å. For α -GeTe, we have a rhombohedral crystal [26]: there are 3 short 2.85 Å and 3 long 3.15 Å GeTe bonds. $|\chi(R)|$ of first shell is expected to show a double contribution, two times less intense and situated on both side of the single β -GeTe one.

Experimental $|\chi(R)|$ of first shell at Ge K-edge is shown on figure 12, and we clearly see two peaks at pseudo- $R = 2.6$ Å and 3.1 Å, unambiguously showing that α -GeTe is obtained⁵. Moreover, despite a low quality EXAFS signal, it is remarkable that EXAFS data adjustment is still able to be quite accurate on distances since it gives a first shell constituted by 3 ± 1 Te at 2.84 Å (2.85 Å awaited for α -GeTe) and 3 ± 1 Te at 3.16 Å (3.15 Å awaited for α -GeTe).

⁵ Please note that the left-out low-R peak probably comes from Ge oxidation, just like for amorphous GeTe

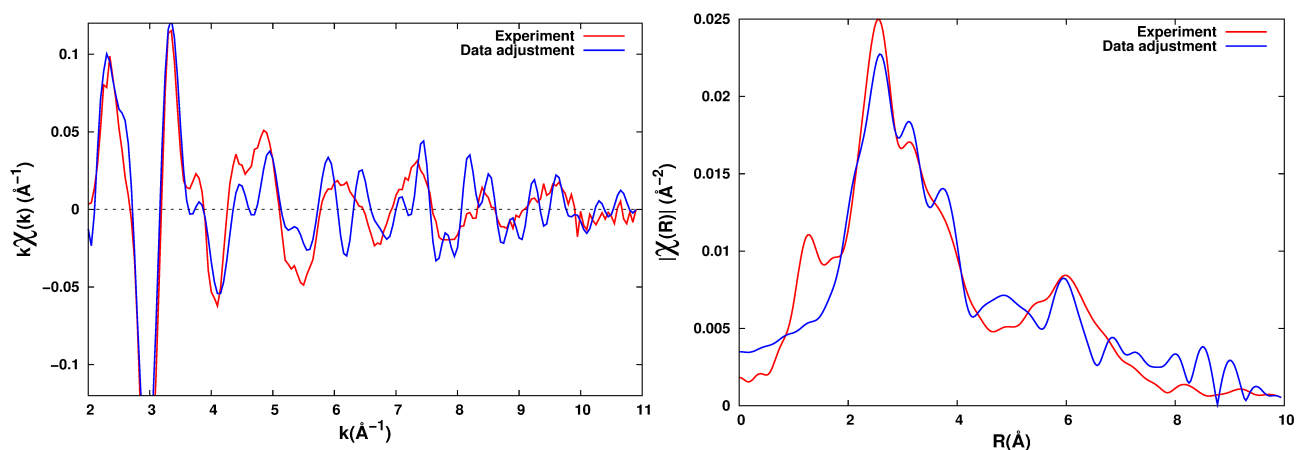


Figure 12: Data adjustment of crystalline GeTe EXAFS signal collected at the Ge K-edge with α -GeTe crystal: first neighbours are 3 Te at 2.84 Å + 3 Te at 3.16 Å.

But how is it possible to form an α -GeTe phase at high temperature when the β -GeTe is stable according to the phase diagram (see figure 10)? Simply because the β -GeTe phase does not exist!

1.3.1.2.3 β -GeTe phase does not exist! order-disorder transition

Indeed, it was assumed until recently that GeTe undergoes around $T_{\alpha-\beta}=705$ K an α to β phase transition, an interpretation that was supported by numerous X-ray and neutron diffraction studies [25] as summarised in the phase diagram of figure 10. But in 2010, our EXAFS study was extended in temperature and completed by X-ray total scattering studies ([27] and [28]) that showed this interpretation is false. In the hypothesis of a classical smooth transition going from α to β phase, the 3 short and 3 long Ge-Te distances (2.83 Å and 3.15 Å at RT) found inside rhombohedral α phase would merge into 6 identical distances (3.02 Å at transition temperature $T_{\alpha-\beta}$) inside the β phase. EXAFS studies unambiguously show this is not the case as illustrated in figure 13.

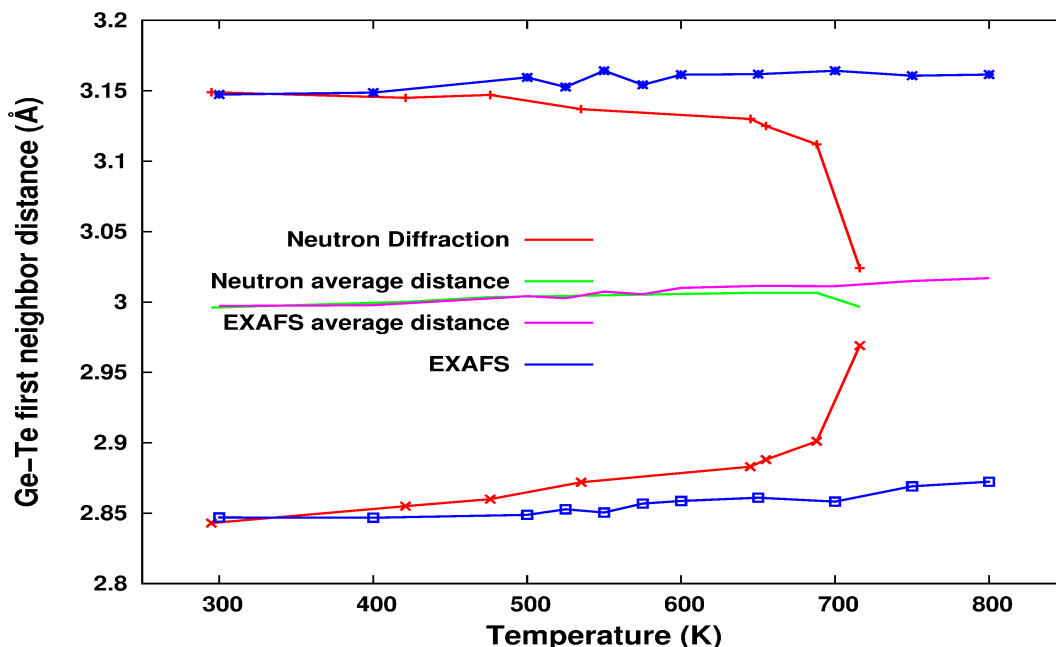


Figure 13: Comparison of GeTe distance as measured directly by EXAFS [27] and as inferred from neutron diffraction [25]. Both methods see the same average distance evolution with temperature, but diffraction wrongly sees short and long bond length becoming the same while EXAFS shows they remain different.

Indeed, the local distortion — elongation along the $\langle 111 \rangle$ axis with an off-centre displacement of the inner atom along the same direction — which is characteristics of the rhombohedral phase, essentially remains unchanged with temperature while average distances found by EXAFS and diffraction are the same. This illustrates the fact that (neutron or X-ray) diffraction only “sees” an average or global structure at large length-scale (typically >10 nm). Rising temperature will

increase *orientational* disorder until the average large length-scale structure has become symmetric at 705 K while local structure as seen by EXAFS at short length-scale (<1 nm) remains distorted. To summarise, crystalline GeTe is constituted with well-defined rhombohedral building blocks that are all the more randomly oriented in space than the temperature is high. There is no β -GeTe phase stabilisation above 705 K but an order-disorder transition where these rhombohedral building blocks are fully randomly oriented in space and GeTe “appears” as cubic for diffraction / neutrons.

Similar effects exist in solid semiconductor solution (see for example [29]) where X-Ray Diffraction (XRD) shows that the lattice parameter follows linearly the relative concentrations of mixed elements (the so-called Vegard's law) while EXAFS shows that short and long bonds still exist: the XRD Vegard's law was only a large length-scale view of the two different small length-scale bond lengths.

1.3.1.3 Structural changes during amorphous/crystalline cycle

During GeTe amorphous \leftrightarrow crystalline cycle, we found the following evolution of neighbours:

	Around Ge		Around Te	
	Coordination	Bonds	Coordination	Bonds
Amorphous GeTe	2 (1+1)	1 Ge-Ge at 2.49 Å 1 Ge-Te at 2.66 Å	2	2 Te-Ge at 2.61 Å
Crystalline GeTe α -GeTe	6 (3+3)	3 Ge-Te at 2.85 Å 3 Ge-Te at 3.15 Å	6 (3+3)	3 Te-Ge at 2.85 Å 3 Te-Ge at 3.15 Å

Table 3: Short-range ordering evolution of GeTe during amorphous \leftrightarrow crystalline cycle

Therefore, the structural rearrangement taking place during a GeTe amorphous \leftrightarrow crystalline cycle is not a simple density change that would only require distance evolution. Indeed, if existing Ge-Te bonds only elongate, existing Ge-Ge bonds must first be broken before a spatial re-ordering occurs where Ge migrates through Te first shell to become second shell.

1.3.2 Study of GST = Ge₂Sb₂Te₅

We have conducted on GST the same complete EXAFS studies than on GeTe. These studies won't be detailed, only their specifics. And indeed, as Sb (Z=51) and Te (Z=52) only differ by one valence electron, they are indistinguishable as *backscatterer* and will be noted [Sb|Te]. Nevertheless, they remain distinguishable as *absorbing atoms* since their absorption edges exhibit a large 1400 eV difference.

1.3.2.1 Amorphous GST

Good quality EXAFS spectra were recorded at the three absorption edges Ge, Sb and Te and determined characteristics of the chemical environment in amorphous GST are shown in table 4:

Absorbing atom	backscatterer	Minimal Number	Distance (Å)	σ^2 (10^{-3}Å^2)	r-factor of fit (%)
Ge	Ge	0.84 \pm 0.36	2.49 \pm 0.01	5.8 \pm 4	0.65
	[Sb Te]	2.86 \pm 0.09	2.625 \pm 0.004	6.6 \pm 0.4	
Sb	Ge**	2.0 \pm 1.6**	2.70 \pm 0.02**	16.0 \pm 8.6**	1.1
	[Sb Te]	3.0 \pm 0.20	2.83 \pm 0.03	6.6 \pm 0.4	
Te	Ge	1.38 \pm 0.2	2.66 \pm 0.003	7.1 \pm 1.2	0.37
	[Sb Te]	0.89 \pm 0.06	2.81 \pm 0.010	10.1 \pm 1.6	

Table 4: Amorphous GST chemical environment. ** denotes large data uncertainty

At each absorption edge, only two backscatterers need to be tested: Ge and [Sb|Te]. We observe that a low-k/low-R contribution is always present: this probably corresponds to oxide of Ge, Sb and Te and was left-out using FT^{-1} (as for GeTe, see I.3.1.1.2) with a minimal R varying between 1.4 and 1.6 Å. And our values were found to be compatible with later published reference [30].

I.3.2.2 Crystalline GST

XRD on powder shows that laser crystallized $Ge_2Sb_2Te_5$ is not the thermodynamically stable hexagonal phase but is of the metastable NaCl type structure with Te atoms occupying the first cfc sublattice while the Ge/Sb atoms take place randomly on the second cfc sublattice along with 20% vacancies. These 20% vacancies account for the 2:2:5 atomic ratio between Ge, Sb and Te at GST congruent composition. With $a=6.0117$ Å [26], Ge, Te and Sb expected first neighbours distances are identical and equal to 3.01 Å. Our recorded EXAFS spectra of crystalline GST at the three absorption edges were of poor quality, and we could not check these values. Just like with GeTe (see I.3.1.1.2), it seems we experience a large crystalline distortion, maybe caused by the huge 20% vacancies. Some years later in 2004, an EXAFS study [31] was successfully conducted on GST and showed that laser-crystallized GST was not of the admitted NaCl type but was constituted by well-defined rigid blocks that were fully randomly oriented thus averaging as a cubic NaCl structure. GST at RT is a completely randomised crystal, a characteristic it shares with GeTe but only above $T_{\alpha-\beta}$ as seen in I.3.1.2.3. In these rigid blocks, Ge is in a highly distorted O_h octahedral structure, thus explaining why recorded EXAFS spectra have a poor signal-to-noise ratio: Ge has several neighbours situated at various distances with average lengths of Ge-[Te|Sb]=2.83 Å and Sb-[Te|Sb]=2.91 Å.

Despite recorded EXAFS spectra of GST are of poor quality, they could nevertheless be used to characterise eventually segregated amorphous Ge, Te or Sb. Indeed, generally speaking, EXAFS signal of any crystal results from the interference of numerous paths: direct backscattering paths between the absorbing atom and its surrounding shells situated in the first 7 Å (8 shells here) but also multi-scattering paths implying 3 or more backscatterers (18 paths here). And most importantly, all these interferences cannot be fully constructive since they correspond to different distances. By contrast, EXAFS signal of amorphous phase comes from first neighbour shell only without any supplementary interference-induced damping. As a consequence, EXAFS amplitude of crystal decreases much faster with k than amorphous one. At high-k, recorded EXAFS spectra on crystalline GST would be dominated by the eventual presence of an amorphous phase. And this is indeed the case since for $k > \sim 7$ Å⁻¹, EXAFS oscillations at Sb K-edge could be nicely adjusted with amorphous [Sb|Te] at 2.9 Å, a perfectly coherent finding with [32] that suggests the presence of amorphous Sb at GST grain boundaries. Figure 14 and table 5 show data adjustment values.

Crystalline GST at Sb K-edge, data adjustment conducted on $R \in [2.2-3.2]$ Å, high-k part only						
Overall				[Sb Te] backscatterer		
r-factor of fit (%)	ΔE_0 (eV)	k-range (Å ⁻¹)	k-weight	Num	Distance (Å)	σ^2 (10 ⁻³ Å ²)
1.2	-1.9±1.8	5.6-14.0	1	1.0±0.17	2.90±0.007	3.9±0.8

Table 5: Chemical environment of an amorphous Sb-[Sb|Te] phase present in GST sample

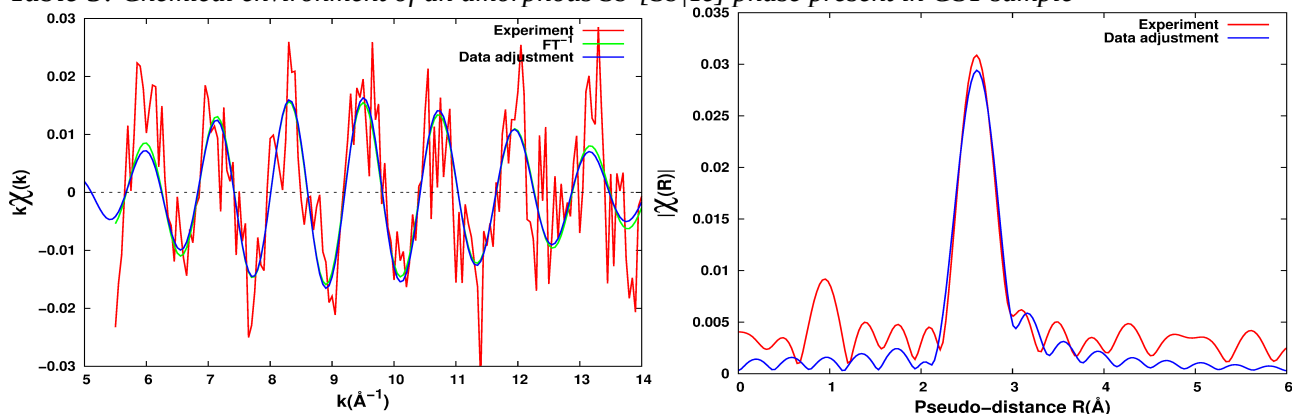


Figure 14: Data adjustment on the high-k part of the EXAFS of GST at the Sb K-edge.

I.3.2.3 Structural changes during amorphous/crystalline cycle

During GST amorphous↔crystalline cycle, we found the following evolution of neighbours:

	Around Ge	Around Sb	Around Te
Amorphous GST	1 Ge-Ge at 2.49 Å 3 Ge-[Sb Te] at 2.63 Å	3 Sb-[Sb Te] at 2.84 Å Sb-Ge low contribution	1.5 Te-Ge at 2.66 Å 1 Te-[Sb Te] at 2.81 Å
Crystalline GST	6 Ge-[Sb Te] at 2.83 Å	6 Sb-[Sb Te] at 2.91 Å	?? Te-[Sb Te] at 2.91 Å ?? Te-Ge at 2.83 Å

Table 6: Short-range ordering evolution of GST during amorphous ↔ crystalline cycle

As can be seen, structural rearrangement taking place during GST amorphous↔crystalline cycle is almost like a density change but for the presence of Ge-Ge bonds: as for GeTe, only the Ge-Ge bonds prevent the amorphous↔crystalline cycle to be a pure density change and require atomic rearrangement.

I.3.3 Conclusion

Firstly, in amorphous material GeTe or GST, we logically found the same distances between atoms whatever the energy edge: Ge-Ge at 2.49 Å, Ge-[Sb|Te] at 2.63 Å and [Sb|Te]-[Sb|Te] at 2.83 Å. And coherently, the heavier the atom, the larger its covalent radii, the longer its bonding distance. Secondly, we found that the amorphous↔crystalline cycle could be a simple density change but for the presence of the Ge-Ge bonds in the amorphous phase: disappearance of Ge-Ge bonds is something costly in energy and time since Ge-Ge bonds must first be broken and then Ge atoms must diffuse through the surrounding [Sb|Te] shell. Moreover, based on the crystallisation temperature (RT, 180°C, 450°C) for amorphous [Sb|Te], GeTe and Ge, the Ge-Ge bond appears as the most stable. For each Ge in amorphous GeTe and GST, there is one Ge-Ge bond. As GST contains a smaller percentage (20%) of Ge than GeTe (50%), amorphous↔crystalline cycle requires less Ge diffusion, and we believe this explains why GST commutes faster than GeTe. Therefore, adding Sb to binary GeTe to make GST does not accelerate crystallisation but rather prevents the formation of speed limiting Ge-Ge bonds. The common key feature is what we were the first to see: for fast switching, Ge-Ge bonds must be avoided in the amorphous phase.

Following our study, several other studies have been conducted on the origin and limitation of speed of amorphous↔crystalline cycle. Notably, the umbrella-flip model ([31] and [33]) was proposed in 2004 by A. Kolobov. But this did not settle the question and various interpretations were proposed like bond constraint theory, distortion and ring structure transformation ([30], [15] and [34]). And still nowadays in 2018, there is a large debate on the origin and optimisation of the GST fast amorphous↔crystalline cycle [35]–[38].

I.4 Super-resolution effect with InSb

Beside speed, we have studied another way to enhance PCM performances: a new PCM layer that diminishes the minimum readable spot size and thus enhance information density. This is called the super-resolution effect, a key technological effect since it enables commercially-available laser reading head to overcome their diffraction-limited spatial resolution.

The interesting and specific property of InSb PCM comes from its solid to liquid phase change at 800 K which abruptly multiplies by 10^6 its density of carriers, see left of figure 15. This semiconductor to metal change leads to a non-linear variation of its optical properties which creates a sub-pupil on the laser focusing spot, see figure 16: a standard commercial Blu-ray head ($\lambda=405$ nm with 0.85 numerical aperture) which has a diffraction-limited resolution of 120 nm, will see its resolution boosted by the super-resolution effect down to 80 nm!

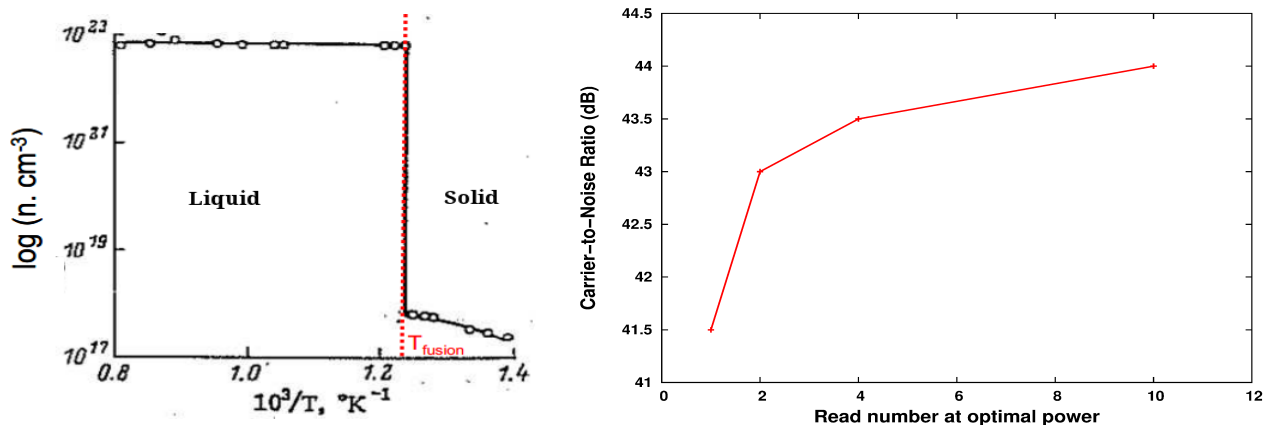


Figure 15: Left: evolution of InSb carrier density near fusion point from [64]. Right: improvement of the CNR with the number of reads realised at optimum power

And InSb brings also another nice feature: we observe an improvement of the carrier-to-noise ratio (CNR) with the number of read, see right of figure 15. As the origin of this improvement was completely mysterious, we decided to conduct grazing incidence diffraction studies on the active layer, and notably as a function of the number of reads.

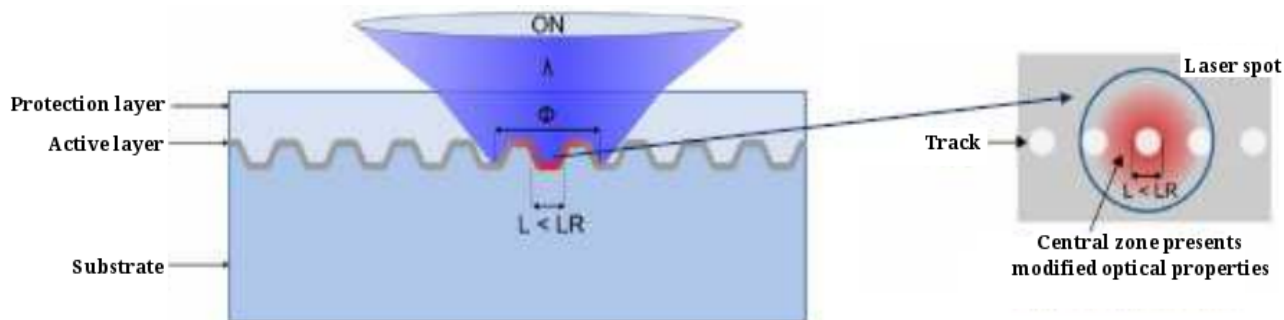


Figure 16: The super-resolution effect: using an optical non-linear active InSb layer, central zone with modified optical properties boosts optical resolution beyond the resolution limit

1.4.1 Experimental conditions

Data were collected on samples that were the closest possible to the real Super-REsolution Near-field Structure (Super-RENS) with a 20 nm thick InSb active layer sandwiched between either anti-diffusion insulating ZnS-SiO₂ or ZrO₂ (+5%Y₂O₃) barriers. Super-RENS were read in conditions where the super-resolution effect occurs, that is with a continuous Blu-ray laser at optimal 1.35 mW power with a 3.3 m/s track linear speed. Samples were held either in horizontal or vertical position in order to measure diffraction signal in the three possible directions:

- along the sample thickness, that is in the perpendicular direction
- in-plane along the laser reading track, that is in the longitudinal direction
- in-plane but perpendicular to the reading track, that is in the radial direction

Diffraction experiments were conducted on the synchrotron beamline BM32 (IF) of ESRF using a classical 5-circle goniometer (GMT experimental station). Given the very thin layer, expected signal is very low: diffraction studies were conducted under grazing incidence at 8.048 keV (identical to laboratory diffractometer 1.54 Å). Of course, to collect good quality diffraction data, we must have a good angular resolution: instead of closing detection slits and lose much signal, we used a Ge(111) analyser crystal in front of our photomultiplier to record data. This analyser is indeed a main asset since we achieved (including beam convergence) a 1/100° angular resolution — negligible compared to diffraction peak FWHM — while collecting photons from the whole footprint.

Whenever the signal allows it, we have recorded the three main diffraction peaks of InSb which are [111], [220] and [311] in decreasing intensity order. Bragg diffraction peaks were fitted using the usual pseudo-Voigt function with a linear background function: peak position, amplitude and integral width β were fitted. As experimental resolution is negligible in front of β , β value were not corrected. We assumed that peak broadening comes from crystallite size only, neither microstrain

nor lattice imperfections were considered so that the well-known Scherrer's law was used to determine average crystallite size: $s = \frac{\lambda}{\beta \cos(\theta)}$.

I.4.2 Results

I.4.2.1 50 nm InSb: test study

Because good signal-to-noise is hard to achieve on a 20 nm thick layer, we have first conducted a test study using a thicker InSb layer of 50 nm. Figure 17 shows results of these studies. Clearly, crystallite size increases with the number of reads both perpendicularly and radially, going roughly from 30 to 50 nm when the number of reads goes from 1 to 16. And for 16 reads, crystallite size in the perpendicular direction reaches the layer thickness. This suggests that the CNR improvement with the number of reads comes from the crystallite size growing up.

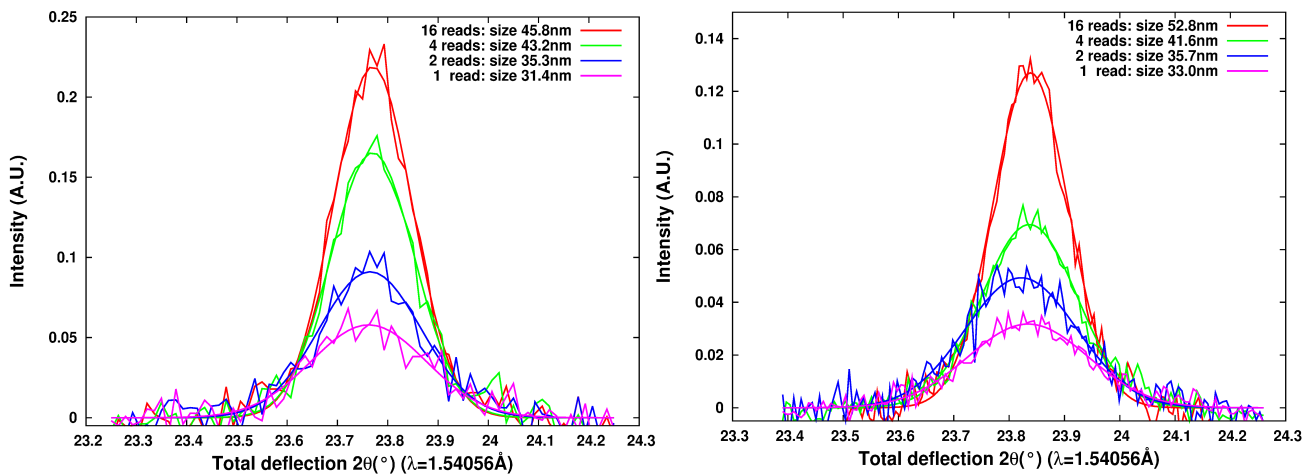


Figure 17: Crystallite perpendicular (left) and radial (right) sizes deduced from the integral width of [111] diffraction peaks. Sample is made of 50 nm InSb sandwiched between ZnS-SiO₂ layers. Crystallite sizes increase with the number of read, perpendicular and radial sizes are found equal at ±10%.

I.4.2.2 20 nm InSb with ZnS-SiO₂

Table 7 summarises all results found on a 20 nm InSb layer sandwiched between ZnS-SiO₂. After just 4 reads (which could simply be incorporated to the PCM initialisation process), we found that crystallite thickness reaches the layer thickness while radial size grows from 40 nm to 55 nm when

	Grazing angle (°)	[111]	Grazing angle (°)	[220]	Grazing angle (°)	[311]	Average size
PERPENDICULAR crystallite size (nm)							
4 reads	0.3	19.2					19.2
16 reads	0.3	20.2	0.3	bad quality			20.22
	0.5	20.3					
	0.5	20.7	0.5	bad quality	0.5	19.7	
RADIAL crystallite size (nm)							
1 read			4	bad quality			
2 reads	4	bad quality	4	42.8	4	35.9	39.4
4 reads	4	bad quality	4	47.7	4	45.1	46.4
16 reads	4	bad quality	4	55.4	4	bad quality	55.4

Table 7: Diffraction studies results on 20 nm InSb layer sandwiched between ZnS-SiO₂ layers.

going to 16 reads. Clearly, these results are coherent with previous ones on 50 nm thick layer, also showing that the CNR improves with radial size: at optimal CNR, crystallites are thick disks.

I.4.2.3 20 nm InSb with ZrO₂

To increase cyclability of the super-resolution layer, trial and error showed that ZrO₂ layers (classically stabilised by 5% Y₂O₃) are more efficient than ZnS-SiO₂. Table 8 gives results found on a 20 nm InSb layer sandwiched between ZrO₂ layers which was read 16 times. Clearly, the use of ZrO₂ instead of ZnS-SiO₂ leads to smaller crystallite sizes but still in the perpendicular direction, they reach the full layer thickness.

	Grazing angle (°)	[111]	Grazing angle (°)	[220]	Grazing angle (°)	[311]	Average value
PERPENDICULAR crystallite size (nm)							
16 reads	0.5	18.3	0.5	bad quality	0.5	18.0	18.15
RADIAL crystallite size (nm)							
16 reads	2.5	29.2	2.5	29.8	2.5	bad quality	29.5
LONGITUDINAL crystallite size (nm)							
16 reads	6	25.7	6	25.1	6	bad quality	25.4

Table 8: Diffraction studies results on 20 nm InSb layer sandwiched between ZrO₂ layers.

I.4.2.4 Best super-resolution effect

In conclusion, the best super-resolution effect is achieved with a high granulometric InSb layer constituted with crystallites that are arranged side by side, not juxtaposed since they occupy the whole thickness. As this InSb super-resolution effect doubles the BD capacity without requiring development of a new reading head, it has large potential applications and a patent [39] was logically deposited in France, extended to Europe, US and Japan.

Based on this patent, a consortium including CEA, Samsung, Mitsubishi and AIST has successfully produced and demonstrated by the end of 2009 the performance of an SR (Super-RENS single-face Blu-ray disc) of 50Gb capacity by simultaneously displaying 4 Full-HD video flux with a 5.10⁻⁵ error reading rate (10 times better than required for commercialisation). This was a worldwide first! And Mitsubishi to conclude: "Video content was successfully replayed with no motion freeze and no block noise on display during playback both at 36 and 72 Mbps with 50 GB SR discs", see figure 22. This demonstration was a major contribution to the European funded project FP7-SURPASS and the SR technology was chosen to decrease the minimum mark length as well as the track pitch on the disc: Super-RENS will be the 4th-generation of optical storage devices [40].



Figure 18: Demonstration of a Super-RENS single-face Blu-ray disc of 50Gb capacity in 2009.

II The μ Laue setup

Since the beginning of this manuscript, we have been using EXAFS and diffraction techniques. Let us now focus on a third technique that is both emblematic of synchrotron and extends classical diffraction: submicronic Laue diffraction. Indeed, for this special diffraction technique, we simultaneously need an intense X-ray beam of continuous energy over a very broad range with a submicronic spot size, a challenge only synchrotron may take up.

In the case of classical diffraction, X-ray energy is fixed and to get specific sample's crystalline planes to diffract, one must either move the detector or the sample or both. More precisely, if the beam size is really large compared to crystallites sizes — which was the case until now since beam spot size was millimetric while crystallites were nanometric — there is no need to move the sample: there will always exist a crystallite among all those illuminated that is correctly oriented (powder diffraction case). But when the beam size gets close to the crystallite size, sample must first be scanned to adequately orient at least one illuminated crystallite before detector scan may show any diffraction peaks (monocrystal diffraction case).

In the case of Laue diffraction, the X-ray energy range is large and a lot of sample's crystalline planes will naturally diffract without demanding any specific orientation prior to diffraction. This fundamental advantage that has Laue diffraction to make any crystal diffract whatever its orientation, has long been known and made Laue diffraction the technique of reference to determine crystal orientation. More precisely for Laue diffraction — and contrary to classical diffraction — it is best if the beam size gets close to crystallite size so that only a single (or at least a reasonably small number of) crystallite will diffract. Consequently, spatial resolution of the Laue diffraction is given by the beam spot size, and we have developed a dedicated setup called the “ μ Laue setup” to make the beam spot size as small as possible.

The first setup was developed and financed with a main foreseen application concerning diagnostic of copper interconnects as used in the whole micro-electronic industry: given interconnect dimensions, a submicronic beam was mandatory. But in fact, it may be used on any kind of (poly-)crystalline material whose typical characteristic length is of the micron size. And indeed in the vast domain of high-performance IR detection, we use the extremely low dislocation density single-crystal HgCdTe material under the form of arrays of pixels whose typical dimension are 10 μm . Therefore, once the first setup was upgraded, we would use it to study the HgCdTe high performance IR detection material.

II.1 The first setup

II.1.1 Presentation

The principle of a μ Laue experiment is rather straightforward as shown on figure 19: it consists in sending a submicronic X-ray beam with a continuous and sufficiently large spectral range onto the sample. This white submicronic beam will then be diffracted along all energy accessible diffraction direction of the sample by all illuminated grains. All these diffraction directions will be measured simultaneously (usually more than 50!) using a large area CCD camera positioned above the sample.

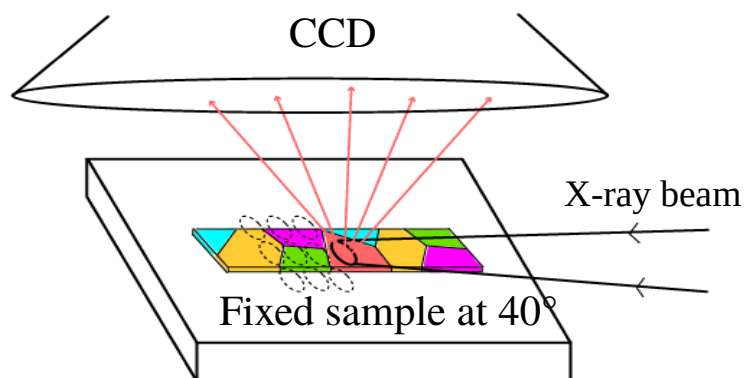


Figure 19: Principe of a μ Laue experiment

To obtain the X-ray white submicronic beam, we have implemented a two-step demagnification. The first demagnification transforms the ESRF's 270x80 μm^2 source into a spot 32.3 m later where

only the central part is selected using a high-precision adjustable slit, thus creating a secondary X-ray source of typically 20 μm size. Using classical Kirkpatrick-Baez (KB) focusing mirrors with adjustable curvature, this secondary source is then demagnified 30-40 times into our small X-ray white submicronic beam, and we were able to achieve a $0.5 \times 0.7 \mu\text{m}^2$ white beam of [4-25] keV energy range [41]. When created, this tool was unique in Europe and still is!

The two main assets of using a white beam instead of a monochromatic beam is that a full diffraction diagram requires less than 5s to measure without any sample movement: no need to rapidly rotate the sample on itself with a sphere of confusion of one tenth of the beam size! Sample movement is only required to achieve sample mapping. For each grain, using the position of several diffraction peaks (at least 5), the crystallographic orientation (3 Miller indexes) as well as the deviatoric part of the strain/stress tensor are determined (5 out of the 6 parameters of the strain/stress tensor). The hydrostatic part of the strain/stress tensor requires the determination of at least one diffraction peak energy: this is implemented thanks to the first demagnification step where our beamline's monochromator may be inserted (see section II of publication [41]).

Let us now look at some submicronic Laue diffraction studies that were conducted on copper interconnects to assess the measurement capabilities of the μLaue setup.

II.1.2 Copper interconnects problematic

Concerning copper interconnects, the first aspect to be studied concerns the source of interconnect failure. Indeed, copper interconnects display high strain originating from the different anneals requested in the manufacturing process as well as electrodeposition. The eventual relaxation of this stress may form voids (leading to circuit break) or hillocks (leading to short circuit) and thus induce failure. And the same stands for the electrical current flow that induces electro-migration of copper. The second aspect concerns interconnect resistivity. As the semiconductor technology continues to scale down, the resistivity of narrow lines exhibits pronounced size effects and tends to increase, an increase which is linked to both grain sizes (bigger is better) and texture (resistivity at grain boundary highly depends on orientation change). Providing both grain orientation and stress tensor, the μLaue setup is perfectly suited for interconnect study. And in 2006, we have performed our first μLaue measurements on a 1 μm wide interconnect for integrated circuit. A 60 μm long portion of the line was mapped with a 2 μm step. The goal was to validate both the equipment and the analysis software of the μLaue by comparing obtained results at microscopic scale with previous results obtained at a macroscopic scale on a network of parallel 1 μm copper lines.

II.1.3 Camera calibration

A typical diffraction image is presented in figure 20. The vast majority of diffraction spots naturally belongs to Silicon: the massive 600 μm thick Si(001) substrate diffracts far more intensively than our 250 nm thin copper line! But beyond the simple intensity difference, Si and Cu spots have quite different shapes: if Cu diffraction spots are all round, most Si spots are elongated along the incoming beam direction with a round top edge and a long bottom tail. This effect is specific to white beam diffraction: since a large range [4-25] keV of X-ray energy is present, different diffraction orders coexist (from order 1 up to 6) and μLaue diffraction spots might be the superposition of various diffraction orders. This may have a great impact of spot shape since the higher the order, the higher the energy, the higher the penetration length into the material, the more elongated along the incoming beam direction is the diffraction volume and consequently the diffraction spot.

Such effect is clearly visible for our massive 600 μm thick Si where round top edge comes from fundamental energy diffraction which has the lowest penetration length while the long bottom tail comes from high energy harmonics which have higher penetration length. In contrast, as our Cu 250 nm thickness is much smaller than X-ray penetration length, whatever the diffraction order, diffraction volume is constant and maximal: Cu spot shapes are constant and round.

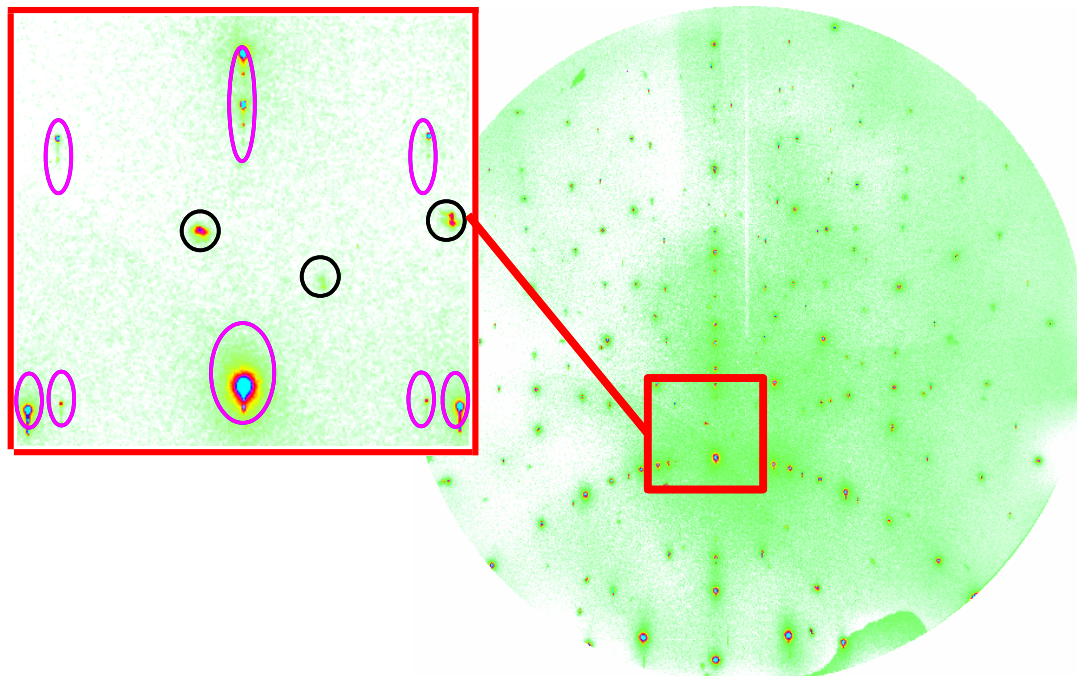


Figure 20: Diffraction image of 1 μm wide interconnect. Left insert shows a zoom of the central part: Si elongated spots are evidenced with light magenta and Cu round spots with black.

For data treatment, we have used the world reference program XMAS [42] (X-ray Microdiffraction Analysis Software) of Nobumichi Tamura from the Advanced Light Source. Data analysis only requires taking into account the position of the diffraction spot on the CCD: image is transformed into a list of spot positions. But spot position must be well determined with typically a 1/10th of pixel precision. Therefore, Si diffraction spots are badly suited for this job! Si diffraction spots with a low fundamental energy diffraction display numerous harmonics leading to a long bottom tail that will artificially displace its centre towards the bottom. And high fundamental energy diffraction spot will indeed be single but with a high penetration length, spot will be totally elongated! This effect is crippling: taking into account the 143 visible diffraction spots obtained using a stress-relieved monocrystalline Si(001) wafer, the smaller residual von Mises stress we could obtain by adjusting all the 6 camera parameters (3 angles + 3 positions) was 231 MPa instead of 0!

Therefore, we must use a more absorbing element that will limit the penetration length in our energy range: since Ge is heavier and denser than Si, we used a fully relaxed monocrystalline Ge(111) wafer. And indeed as shown on figure 21, Ge(111) diffraction spots are round whatever the energy! Taking into account the 111 visible diffraction spots, we get a residual von Mises stress of 4.95 MPa corresponding to a residual strain in calibrating sample smaller than $2 \cdot 10^{-5}$: using Ge, we are able to calibrate with an excellent precision the position of the camera relative to the incoming X-ray beam. Now that camera position has been precisely calibrated using Ge(111) wafer, we may now proceed with measurements on interconnects.

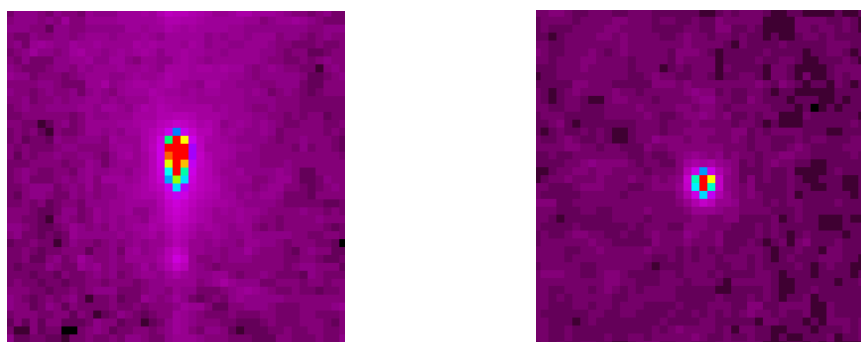


Figure 21: At high 21 keV energy, we observe that Ge diffraction spot (right) stays nicely round while Si spot (left) is highly elongated.

II.2 Measurements on copper line

Samples are constituted by a series of several millimetres long single damascene copper lines of 250 nm height with variable width (from 250 to 1000 nm), deposited on a Si wafer. Damascene copper lines were fully functional since they constitute a working electrical device. Copper lines have thus undergone all necessary manufacturing processes: annealing steps, O flashes, Ta/TaN barrier as well as copper overburden removal using chemical mechanical polishing.

II.2.1 1 μm wide copper line

In recorded images (see figure 20), there is simultaneously Cu and Si spots, but as already said we are only interested in Cu spots. As Si spots come from the wafer, their positions do not depend on X-ray beam position onto the copper line. Therefore, the straightforward method is to determine the position of all spots in an image and then suppress from this list, spots belonging to Si to obtain the list of Cu spots; the Si spot list being easily obtained recording an image outside of the copper line. But this method suffers a nasty drawback: as Cu spots are less intense than Si spots, their position is influenced by the eventual presence of a nearby Si spot as shown in figure 22. To avoid this artefact, we systematically subtract a pure Si reference image to Si/Cu images. And it is the resulting images that will then be treated by XMAS: Cu diffraction spots above background will be fitted to deduce their positions. And XMAS will deduce from this series of positions, the orientation and deviatoric tensor of all visible Cu grains (up to 9 per image).

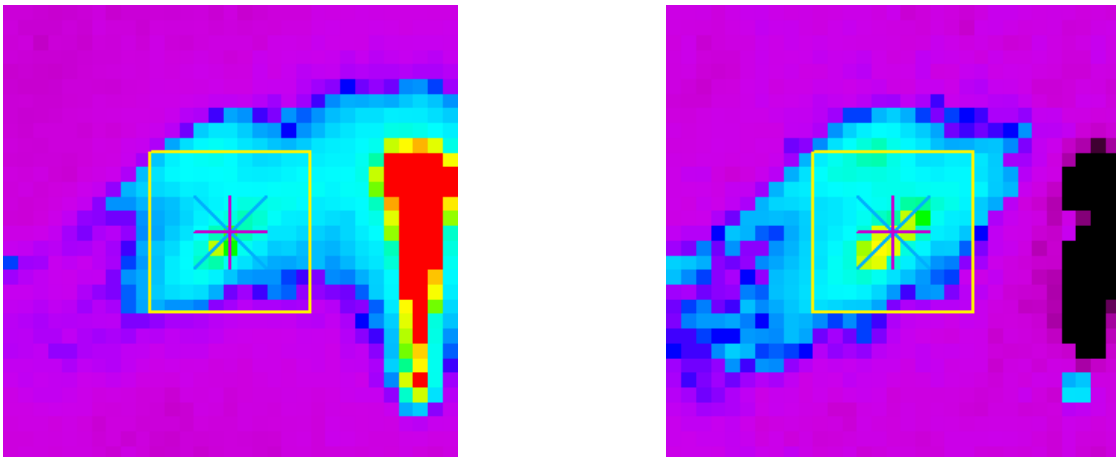


Figure 22: The presence of a highly intense Si spot near the Cu spot makes its position artificially drift towards the Si spot, an artefact suppressed when a reference Si image is subtracted first

But this usually leads to a high level of uncertainties in orientation and deviatoric tensor. To improve results, XMAS will take into account Cu grain orientation to calculate the expected positions of missing diffraction spot. And around the expected position, a second pass is made with a two times smaller threshold. This boosts a lot the number of spot per grain and considerably improves orientation and deviatoric tensor precision for each grain.

Nevertheless, some post-treatment is still necessary to enhance again data quality. First of all, we must suppress some non-sense diffraction spot. Indeed, as stress is adjusted, even if a diffraction spot is far from its theoretical relaxed position, there always exists a high-enough strain that will generate its position. We will therefore limit angular deviation between strain peak and strain-free position. Secondly, XMAS makes the assumption that any diffraction spot belongs only to a single grain, an unjustified hypothesis for us since twins may be present. We will compensate for it. Finally, a sufficiently high number of diffraction spots must be taken into account for each grain to be declared as valid. A custom external program does all this post-treatment before reinjecting data into XMAS for final orientation and strain refinement.

Figure 23 and 24 present obtained results on the 1 μm wide Cu interconnect: we were able to orient and determine the deviatoric tensor for each grain constituting the 1 μm wide copper interconnect line. Figure 23 clearly shows that this line is a succession of various elongated grains whose length extends up to 6 μm with at most three grains constituting the section: μLaue

measurements are clearly adapted to study interconnect lines. This interconnect line is constituted by a majority of grains having their normal orientation along the [111] direction and a minority along [001]. A result that was coherently found using a millimetric X-ray beam on a network of parallel 1 μm interconnects.



Magenta = close to [111] Red = close to [001] Gray = other

Figure 23: Normal orientation of the grains constituting a 1 μm wide and 60 μm long copper interconnect line (not represented to scale). Mapping was conducted every 2 μm .

Figure 24 shows that in average, the [001] grains have the smallest von Mises stresses. On 15 [111] grains, we find a von Mises stress varying between 100 and 500 MPa with an average 283 MPa value. This value is very close to the 245 MPa value extracted from macroscopic measurements [43] and [44]. Therefore, μLaue results are consistent with previous measurements performed at a macroscopic scale: both the μLaue setup and the analysis software are validated.

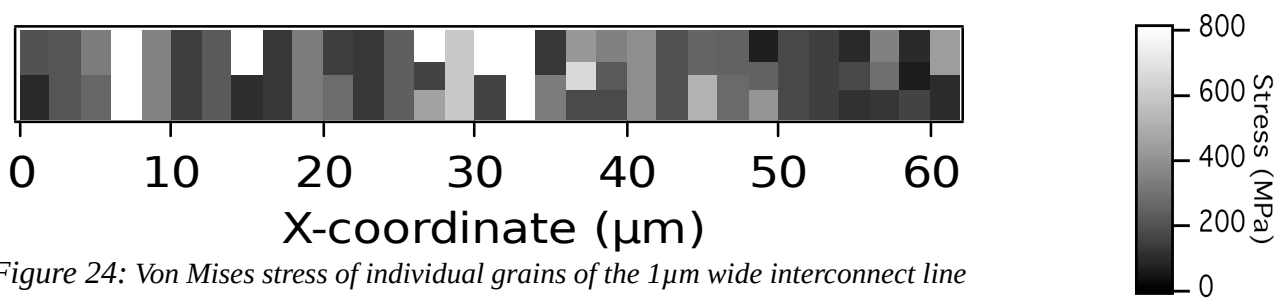


Figure 24: Von Mises stress of individual grains of the 1 μm wide interconnect line

II.2.2 260 nm wide copper line

After the 1 μm wide interconnect line, it was important to go down to smaller line width because different technology nodes in the microelectronics roadmap coexists (around 100 nm in 2007 down to 10 nm in 2017 [45]). In particular, there is a strong need to understand the microstructure evolution (recovery, recrystallisation, grain growth): in the objective to diminish interconnect resistivity, the largest possible grains are desirable. Figure 25 shows the result of the measurement on a fully functionalized interconnect line of 250x260 nm^2 section. For each measurement, only a single grain is clearly visible: the bamboo structure of the interconnect line is clearly visible, in contrast with the 1 μm wide line. At 250x260 nm^2 section, interconnect line is a succession of elongated grains of length varying between 0.5 and 5 μm . The [111] normal orientation dominates.

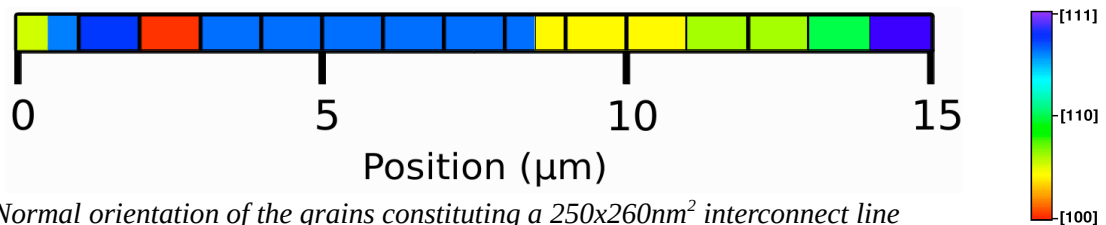


Figure 25: Normal orientation of the grains constituting a 250x260 nm^2 interconnect line

All these measurements were obtained with the submicronic white beam which provides us with the deviatoric part of the stress tensor for each measurement. To obtain the full stress tensor, the hydrostatic stress must be determined and at least one of the diffraction spots energy must be determined. To this end, we have inserted our monochromator in the first demagnification step (see section II of publication [41]) and obtained an energy adjustable submicronic monochromatic beam. We have chosen to determine the energy of the (206) diffraction spot from the [0.316, 0, 0.949] oriented grain. It was determined as 0.57148 \AA instead of 0.57162 \AA when relaxed.

Hydrostatic stress is therefore 418 MPa, and the full stress tensor of this grain is thus:

$$\begin{pmatrix} 594 & -135 & -27 \\ -135 & 277 & -249 \\ -27 & -249 & 383 \end{pmatrix} \text{MPa}.$$

II.2.3 Conclusion

Measurements carried on 1 μm and 260 nm wide interconnect line of 250 nm height clearly demonstrates that the μLaue setup is fully operational. This tool provides us with a mean to measure grain individual orientation and full stress tensor with a submicronic resolution. After four years of use of the μLaue setup, a lot of different kind of samples were successfully studied like UO₂, CdTe, Cu pillars, GeTe ... and the time had come to upgrade the setup.

II.3 Upgraded setup

By extrapolating the signal-to-noise ratio of copper interconnects, we estimate that the μLaue setup may ultimately measure down to 100 nm wide copper interconnects. But in years 2010, interconnect lines were even smaller than 100 nm, and we have updated the μLaue setup with the goal to be able to measure such small objects. Figure 26 shows some pictures of it. Ultimately, the limiting factor when looking down to small object is the intensity of the diffraction spots which must emerge from the smooth varying background signal mainly due to sample surface diffusion.

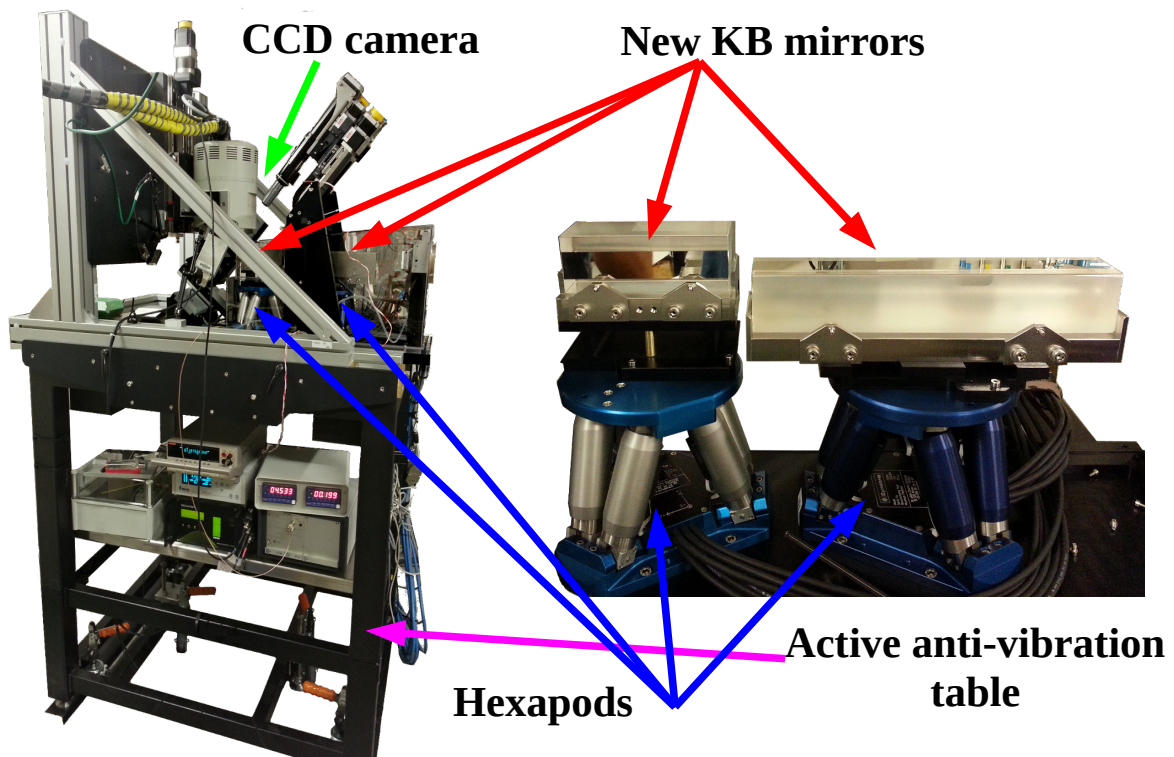


Figure 26: Views of the updated μLaue setup with X-ray beam coming from the right. The left part shows an overall view while the right part shows a detailed view of the KB system. Both perpendicular KB mirrors are mounted on ultra-precise encoded hexapods.

Therefore, the update design goal was to enhance the photon density compared to the first μLaue setup. This is usually achieved by lowering the beam spot size while simultaneously raising the photon flux. Concerning beam spot size, our experience feedback on the μLaue setup showed that we must first raise the optical demagnification factor. Therefore, we used new KB mirrors which are much more compact since they are elliptically fixed-shaped mirrors (avoiding any mechanical bender oversize) and placed much closer to the sample, achieving a 130*50 demagnification.

Secondly, the μ Laue setup is now fixed on an active anti-vibration system to limit as much as possible vibration-induced spot broadening. Previously, we illuminated only one third of the mirror length in order to avoid mirror parts whose shape errors were too strong. As our new mirrors were polished with ultra-low shape error ($\#0.5 \mu\text{rad}$), we are now able to lighten the full mirror length thus greatly raising photon flux as well as shrinking beam spot size as shown in figure 27.

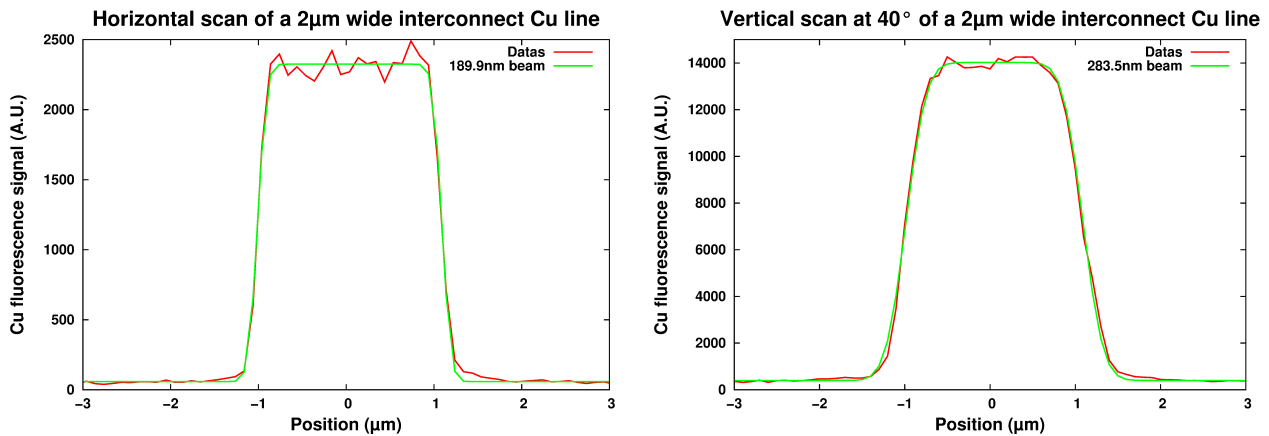


Figure 27: Scan of a 2 μm wide interconnection Cu line to evaluate our white X-ray beam size. Interconnect line was considered as a boxcar function while X-ray beam was modelled as a Gaussian. Data adjustment gives a 2.08 μm wide interconnect line with a beam FWHM of 190 nm in horizontal and 285 nm in vertical with a more than 50 signal-to-noise ratio.

Since September 2012, the updated setup is fully operational and has now replaced the first μ Laue setup. In terms of performance, the updated μ Laue setup routinely delivers a $\text{Ø}300 \text{ nm}$ [4-25] keV white beam with a photon density increase of more than a factor of 10 compared to the first μ Laue setup! With such upgraded performances, the μ Laue setup was perfectly suited to study high-performance IR detectors.

III High-performance IR detection

In this chapter, I will detail several studies that were conducted on high-performance IR detection materials, and these studies make extensive use of the μ Laue setup (see II). They were conducted on a 12-year long 2006→2018 fruitful collaboration with P. Ballet from CEA/LETI: PhD thesis of A. Tuaz [46] that we have co-directed was successfully defended using presented results.

III.1 Introduction to IR and HgCdTe

Generally speaking, because our air is full of water and CO₂, the transmission of IR is separated into three IR domains named SWIR, MWIR and LWIR (Short resp. Medium resp. Long Wavelength InfraRed) as illustrated in figure 28. Currently, application domains for IR are also split into three domains: civilian, military and spatial as illustrated in table 9. In the civilian domain, we need low cost detector so that we deal with low performance detector dedicated to a single IR domain. On the contrary for military and spatial applications, the price is not the main decisional factor, and we will seek high performance detector working on a very large IR domain: these high-performance pixel detectors are liquid nitrogen cooled and detection is based on the photoelectric effect where the active detection zone is a p-n junction.

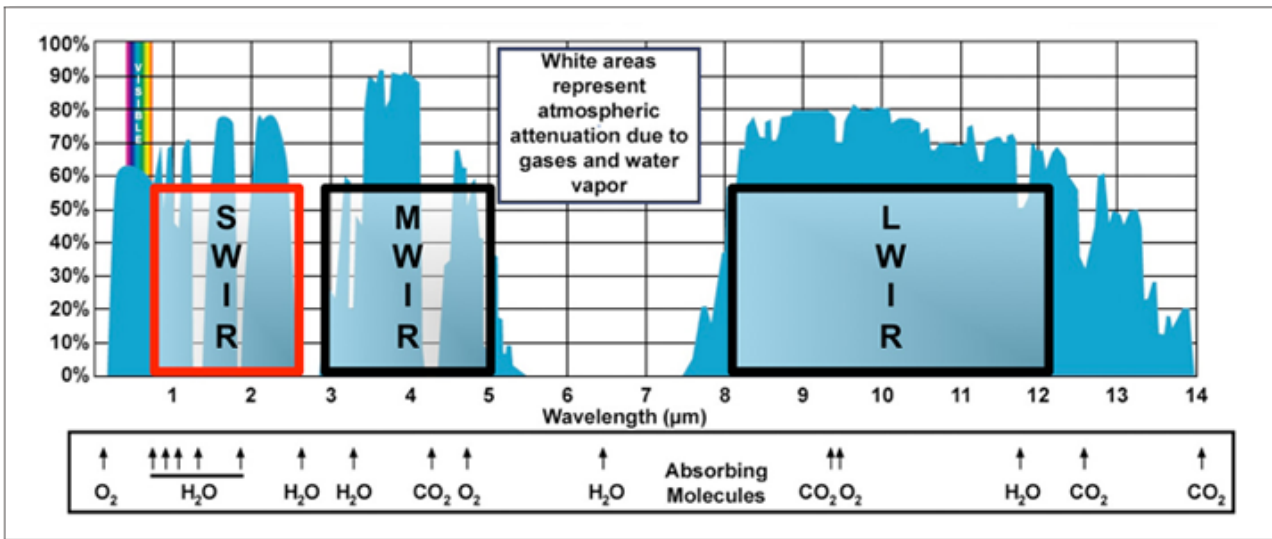


Figure 28: IR atmospheric transmission windows and corresponding absorption molecules


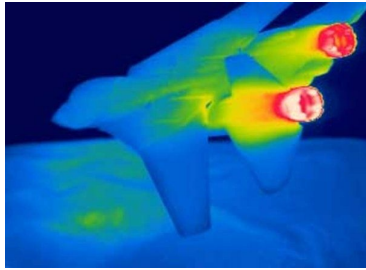
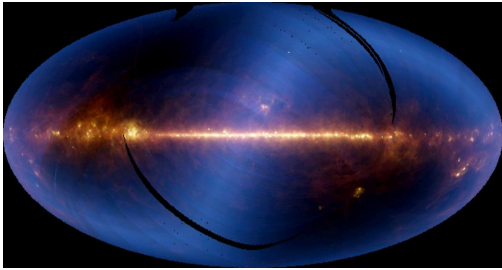
		
Civilian applications like thermal leak study	Military applications like threat detection	Spatial applications like IR mapping of our galaxy

Table 9: IR application domains

Now figure 29 shows all available choice for such a material and despite the vast number of possibilities, clearly the HgTe/CdTe alloy is the material of choice. Indeed, — depending on its composition — the band gap may be adjusted to cover all possible IR domains and moreover HgTe and CdTe have very close lattice parameter thus favouring homogeneous and low defect crystal.

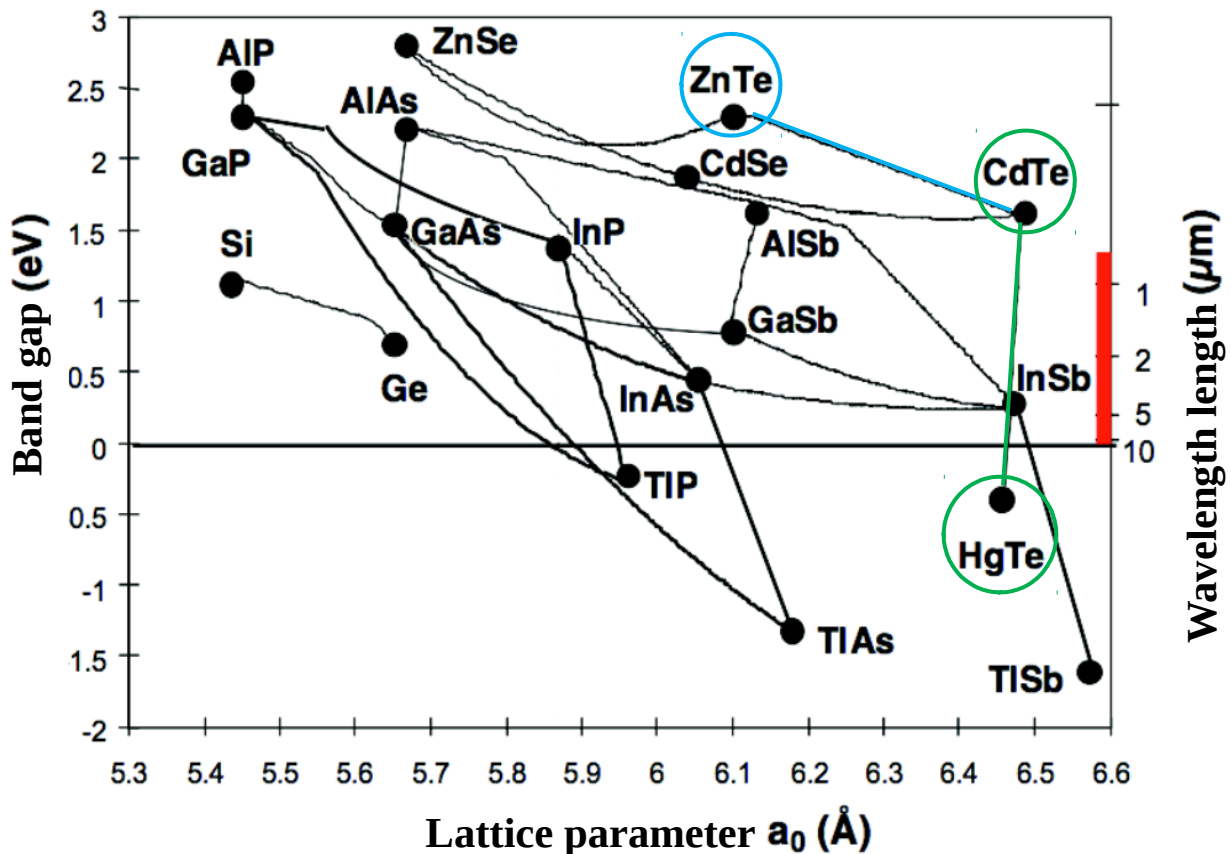


Figure 29: Band gap and cut-off wavelength of various semiconductors and their alloys as a function of lattice parameter (from [65])

With a typical thickness in the μm range, the HgCdTe alloy must be grown onto a much thicker substrate that is transparent to IR. ZnTe/CdTe alloy is a nice solution since it is IR transparent while its crystalline parameter may be matched to that of HgCdTe whatever its composition by tuning the percentage of added ZnTe. Finally, detectors are made of a thin 1-10 μm $\text{Hg}_{1-x}\text{Cd}_x\text{Te}$ detection layer deposited onto a thick $\text{Cd}_{1-y}\text{Zn}_y\text{Te}$ substrate, with x being chosen as a function of the targeted detection domain (LWIR, MWIR or SWIR) and y to match lattice parameters.

III.2 Extrinsic p-type doping

Because a p-n junction is needed for pixel detector, a lot of effort was devoted to achieve doping into HgCdTe [47]. If n or p intrinsic doping as well as extrinsic n doping (using Indium) is quite mastered, extrinsic p-type doping is still a challenge. And it is a challenge worth addressing since it would allow to raise the detector working temperature from liquid N_2 (77 K) to 150 K without impairing performances, thus matching requirements for the next third-generation detectors. The list of potential p-type dopant is quite long since it includes all chemical elements from columns IA, IB and V (H, Li, Na, Rb, Cu, Ag, Au, N, P, As, Sb and Bi). Among these, column V elements are the most promising because of their low diffusion coefficient: As is the dopant of choice for extrinsic p-type doping [48] while Sb is the second best choice.

III.2.1 As implantation

For our study to be meaningful, we decide to manufacture samples that were as close as possible as those of high-performance MWIR pixel detectors. Therefore, As was incorporated inside $\text{Hg}_{72}\text{Cd}_{28}\text{Te}$ using ionic implantation at 360 keV with a 2.10^{14} at.cm⁻² dose, and $\varnothing 8 \mu\text{m}$ pixels at a step of $15 \mu\text{m}$ were implanted using a dedicated mask. To be able to compare implanted and not-implanted zone, we used a focused ion beam (FIB) to extract $4 \mu\text{m}$ wide slices containing two pixels while the sample was vertically placed on the μLaue setup so that the X-ray beam enters the sample through its side (figure 30). Two samples were made: a first one simply as-implanted while the second one underwent a 1 H activation annealing around 400°C under saturated Hg vapor.

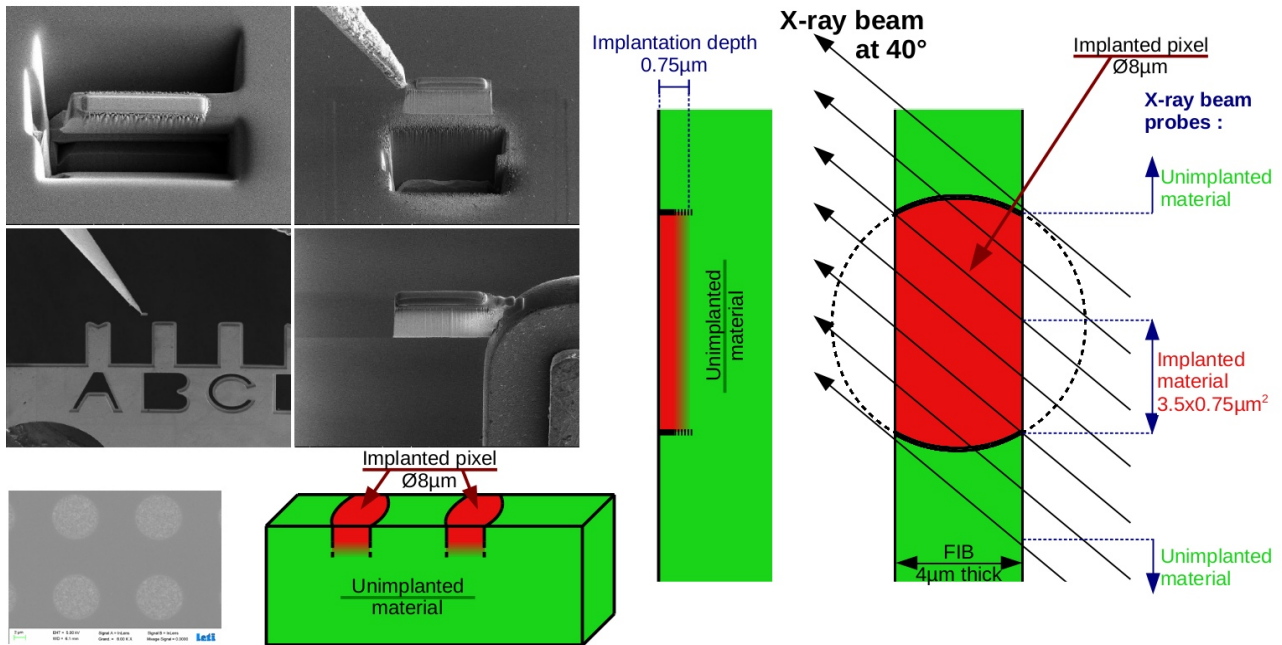


Figure 30: Four top-left images show FIB extraction of a slice containing two pixels and its welding on a dedicated support. Bottom-left image shows implanted spots with contrast obtained through a chemical revelation of the implantation-induced extended defects. Right: X-ray beam trajectories inside sample showing zones where only implanted or not-implanted material is probed.

III.2.2 Diffraction specificities

The ternary alloy $\text{Hg}_{1-x}\text{Cd}_x\text{Te}$ is of the ZincBlende type and is constituted by 2 face-centered cubic sub-lattices (named A and B afterwards) offsetted by $[\frac{1}{4}, \frac{1}{4}, \frac{1}{4}]$ with the anion sub-lattice made of Tellurium while the cation sub-lattice hosts either Hg or Cd, see figure 31. Consequently, (hkl) reflections are only allowed if Miller indexes h, k and l have the same parity and their sum is either odd (odd indexes) or equal to $4n / 4n+2$ (even indexes).

Concerning their intensities, there is a major difference for even Miller indexes. As HgCdTe has a Zinc-Blende AB structure, (hkl) reflections with $h+k+l=4n$ have an amplitude proportional to the square of the sum of atomic form factor $(f_A+f_B)^2$ while $h+k+l=4n+2$ have an amplitude proportional to the square of the difference of atomic form factor $(f_A-f_B)^2$: $4n$ reflections are strong while $4n+2$ reflections are weak. But despite their weakness, they must be carefully studied: as atomic form factors of Cd(48) and Te(52) are similar and almost two times smaller than much heavier Hg(80), $4n+2$ reflections are indeed highly sensitive to the local Hg concentration.

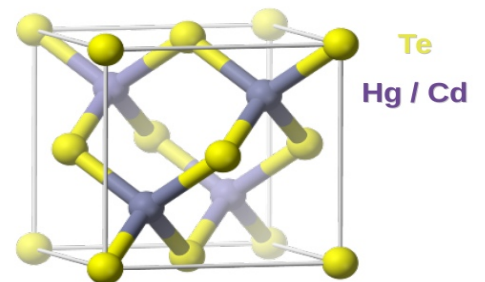


Figure 31: ZincBlende structure of the ternary alloy $\text{Hg}_{1-x}\text{Cd}_x\text{Te}$

Of course from an electrical point of view, As is the main element. But from a diffraction point of view, because its maximum atomic density of $1 \cdot 10^{19}$ at.cm⁻³ is neglectable compared to the $1.5 \cdot 10^{22}$ at.cm⁻³ atomic density of HgCdTe , As impact is negligible.

III.2.3 As-implanted and annealed μ Laue results

Table 10 shows a comparison between diffraction intensity repartition for as-implanted and annealed samples. For each sample, we pick among more than 50 diffraction peaks, the most intense weak one and also a strong one that is closest in energy to avoid any penetration length distortion. Technically, the diffraction peak integral is calculated using two concentric circles around the diffraction peak's most intense pixel position. The inside circle radius is manually adjusted to fully include the peak (typically 7-10 pixels range) while pixels situated less than 3 pixels away (arbitrary value) from inside circle are averaged to evaluate the background level. The sum of all pixels values of the inside circle, diminished from background level, is taken as the integral of the peak. This method is quite robust and reliable since it doesn't depend on the peak shape or any shape fitting.

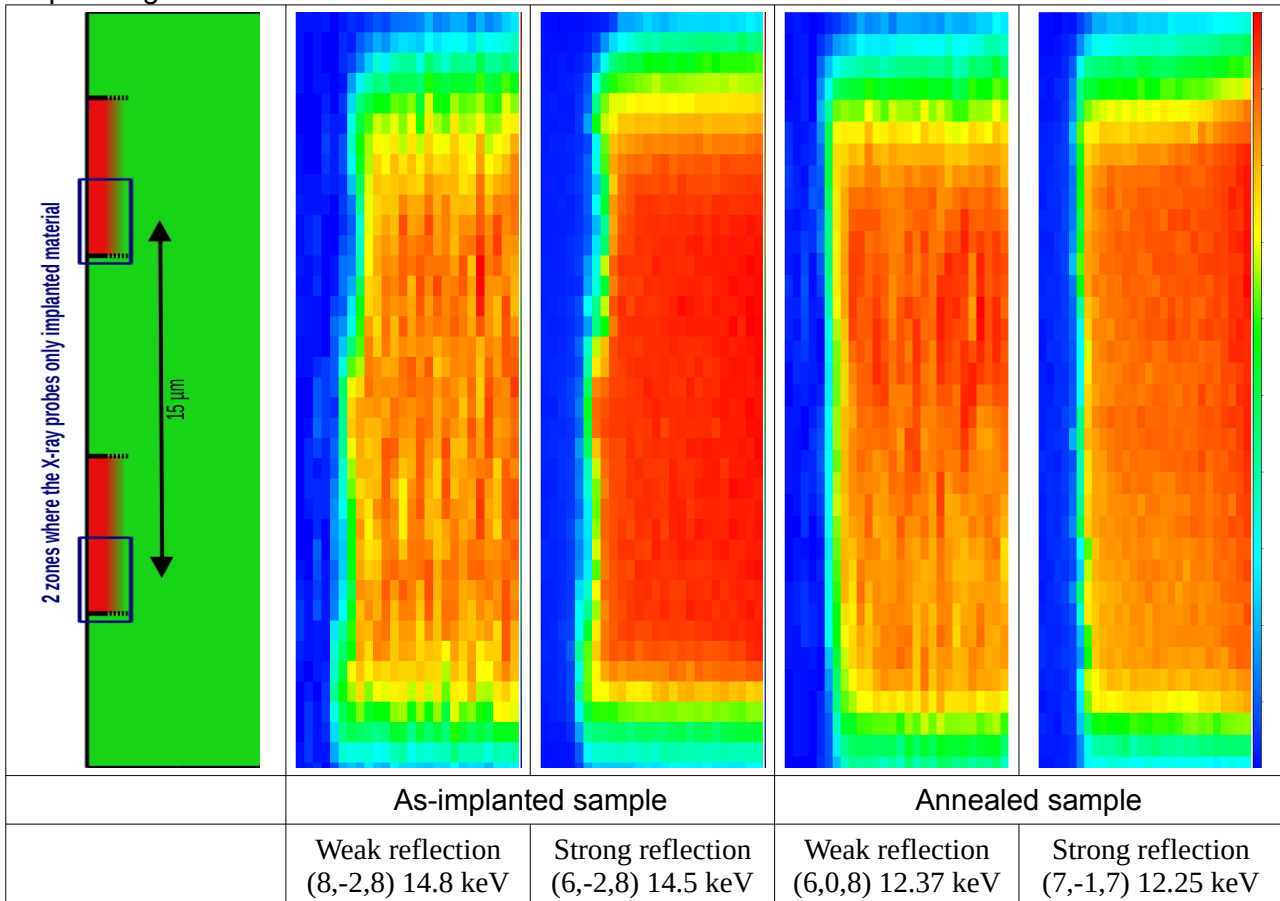


Table 10: Comparison between diffraction intensity repartition for as-implanted and annealed samples. For each sample, we compare the most intense weak reflection with the corresponding strongest one that is closest in energy to avoid any penetration length distortion. Intensity is coloured coded from blue to red as shown at the extreme right and the localisation of implanted pixels is shown on the left. X-ray beam was raster scan every $0.25 \mu\text{m}$ horizontally and $1 \mu\text{m}$ vertically.

Clearly on the as-implanted sample for both weak and strong reflections, there are two zones near the sample's surface where diffraction intensity is almost diminished to background. When comparing to the localisation of implanted pixel shown on the left, these zones correspond to position where the X-ray beam probes only implanted material: ion implantation creates extended defects inside the crystal [48] that diminishes diffraction intensity and this effect is logically maximum when the X-ray beam probes implanted pixels. By contrast once annealed, diffraction intensity weakening is no more visible: annealing has removed from crystal its implantation induced defects.

To be more quantitative, we have to raise the signal-to-noise ratio: we decided to average horizontal lines corresponding to X-ray beam going through either pixel or not-implanted zones and compare then as illustrated in figure 32. Looking at strong reflection, we observe that diffraction intensity is weakened at the surface and that annealing completely removes this weakening. The weakening extension is found to be $0.75\ \mu\text{m}$ and as such weakening is usually associated to implantation induced defects, those obtained through RBS measurement in channelling mode are also represented: satisfyingly, our results (of much lower depth precision though) clearly match those of the density of displaced atoms. Moreover, for the as-implanted sample, we observe that in the $0.5\ \mu\text{m}$ near the surface, the weak reflection is roughly two times less intense than the strong one! Therefore, we observe that reflections proportional to $(f_A - f_B)^2$ are much more weakened than reflections proportional to $(f_A + f_B)^2$.

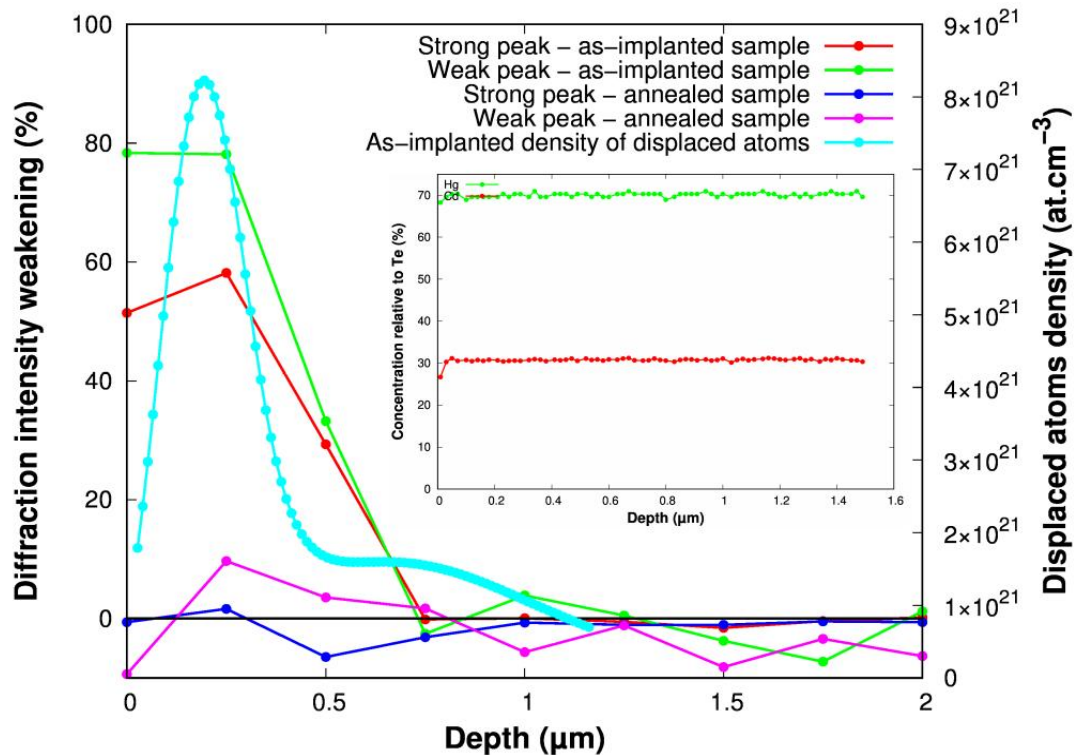


Figure 32: Comparison between strong and weak reflection for the pixel zone of both samples. Density of displaced atoms is also represented against the right scale. Insert: SIMS measurements of the concentration of cations Hg and Cd with depth

A first explanation would be that the local Hg concentration has diminished and calculating the structure factor, we quantitatively determine that the Hg concentration would have dropped from 70% to 63% on the first $0.5\ \mu\text{m}^6$. But this is in contradiction with SIMS measurements made on a fully-implanted plate that show there are no local concentration variation as illustrated in the insert of figure 32.

The proposed explanation is that — because of implantation damages — we have misfit dislocations inducing stacking fault in the crystal. And these stacking faults locally transform the Zinc-Blende AB atomic structure in a BA structure so that on the two fcc sub-lattices, we do not exclusively find cation or anion but a mixture of cation and anion in various proportions: f_A and f_B tend to become equal. Whatever the proportion of anion/cation mixing, this does not affect strong reflections but it will specifically decrease weak reflections and — in the limit case where anion and cation are completely mixed-up — weak reflection would become zero since we would have $f_A = f_B = ((1-x) \cdot f_{\text{Hg}} + x \cdot f_{\text{Cd}} + f_{\text{Te}}) / 2$.

6 Please note that the corresponding 7% decrease of Hg concentration gives rise to a 50% weakening of diffraction intensity thus illustrating the sensitivity to local Hg concentration

III.3 Strain

Of course to make a pixel detector, a p-n junction is not sufficient as shown on figure 33! In fact, once the HgCdTe layer has been epitaxially grown onto the CdZnTe, several technological steps are necessary: individual pixels must be etched into the material, a capping layer must be deposited, implantation occurs to create the p-n junction (as previously seen), annealing to ensure electrical activation and finally hybridation onto the readout chip.

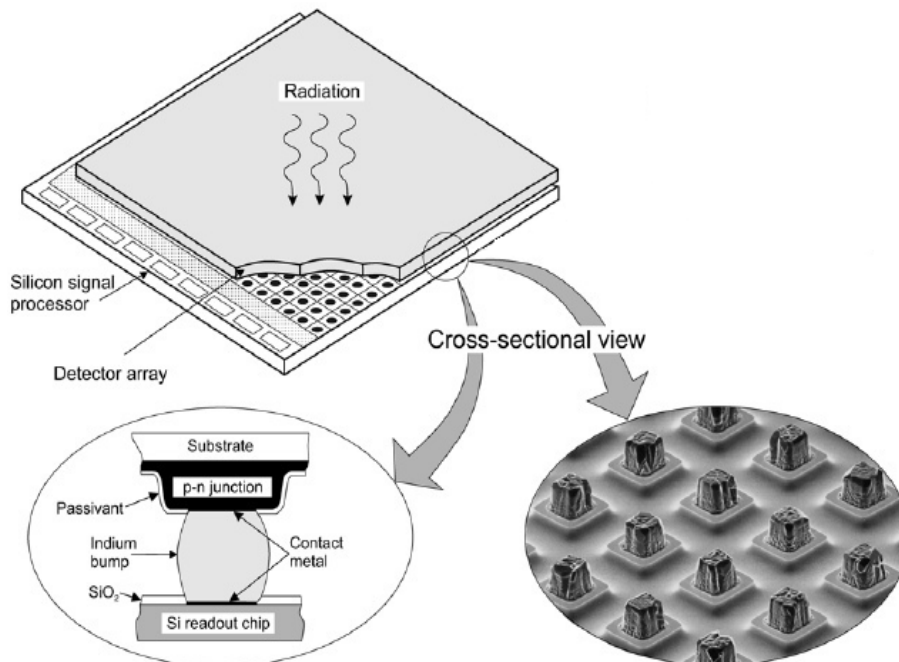


Figure 33: Hybrid IR focal plane array with independently optimised signal detection and readout using the indium bump technique (taken from [47])

Detection in the pixel detector is based on the electron-hole pair creation when a photon is absorbed inside the detection material and its subsequent collection by the p-n junction. But this is only possible if the lifetime of the carrier is sufficient to allow collection [49]: as this lifetime fastly drops with dislocation density, the latter must be as small as possible [50]–[52]. With its low elastic limit of 12-18 MPa equivalent to a $2.7\text{-}4.1 \cdot 10^{-4}$ deformation [53], HgCdTe is a brittle material which tends to easily grow dislocations when strained. Therefore, the final performance of HgCdTe/CdZnTe detectors are directly linked to both HgCdTe crystalline quality and strain, and a lot of efforts these years were devoted to minimise the residual strain in HgCdTe induced by these technological steps. The most important contribution to strain comes from the mismatch between substrate and layer. As lattice parameter evolution with Cd and Zn composition is known [54], it appears there is a theoretic lattice match between MWIR $\text{Hg}_{1-x}\text{Cd}_x\text{Te}$ with $x=30\%$ and $\text{Cd}_{1-y}\text{Zn}_y\text{Te}$ for $y=3.7\%$. Despite typical residual Zn concentration inhomogeneities of 0.5% in CdZnTe prevent from achieving a perfect match [53], we nevertheless benefit from the LETI's IR laboratory expertise and our sample's mismatch are excellent and $< 3 \cdot 10^{-4}$.

But to assess any progress in the field of a residual strain inferior to $4 \cdot 10^{-4}$ on a micrometric sized pixel, you need a high performance measurement tool: classical diffraction with its millimetric spot size is not relevant here. The ideal measurement tool will combine a very high deformation resolution in the 10^{-5} range and offer a sub-micrometric spatial resolution. If the μLaue tool naturally offers the sub-micrometric spatial resolution, performance of the setup must be stretched to its limits to reach the ambitious 10^{-5} range deformation resolution as we will now see.

III.3.1 Stretching the μ Laue to its limits

III.3.1.1 CCD positioning

As strain is deduced from the position of the diffraction peaks measured on the CCD, our first concern was to measure these positions as precisely as possible. Therefore, we started by moving the CCD camera as far as possible away from the beam spot. Consequently, diffraction peak intensity distribution became much more precise as shown on figure 34 and their centre could be more precisely determined. It also becomes clear that this repartition is asymmetrically both vertically and horizontally, with peaks more elongated and asymmetrical along y than x.

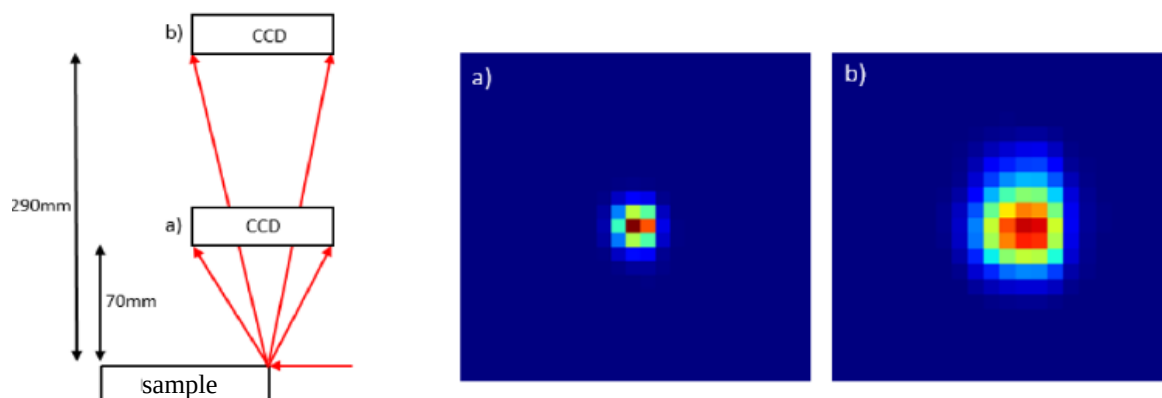


Figure 34: Effect of moving away CCD from sample on the same diffraction peak. With a 4 times better resolution, the asymmetric repartition of the peak's intensity becomes obvious

This is quite a logical finding since this intensity repartition is in the image of the X-ray beam angular intensity repartition that is rendered asymmetrical by the residual polishing and shape slopes error of our vertical and horizontal focalisation mirrors. Please note that our beam is reflected by 3 mirrors in the y direction but only one in the x direction with an ultra-low shape error mirror thus naturally inducing much less angular dispersion along x than y. And with an asymmetrical intensity distribution, both the reference μ Laue programs XMAS [42] and LaueTools [55] that use symmetric 2D Gaussian / Pearson / Pseudo-voigt functions cannot be used. Moreover, we observed quite a large variation of shapes depending both on chosen peak or measurement points. Therefore, we had to develop our own high resolution peak shape fitting routines able to adapt to peak shape.

III.3.1.2 Optimised fitting routine on asymmetrical peak

This routine independently takes care of the horizontal and vertical peak shape: 5 successive profiles of the peak intensity are taken centered on the peak's most intense profile. For each profile, we adjust 2 independent Gaussian functions and a background level. Once fitted, we calculate 5 central positions as barycentres of the profile while the final peak position is taken as the average of these 5 central positions weighted by the profile intensity.

As the peak is asymmetric, background evaluation must be made carefully to avoid any confusion between background and a very large low intensity off-centered Gaussian function. Therefore, we developed a specific tool to remove background noise on the CCD image prior to peak fitting. Background noise here corresponds to the camera's intrinsic noise (which is quite low) but also the fluorescence signal from various chemical elements from the sample that give rise to a non-uniform signal when intercepted by the plane of the CCD, not to mention any inhomogeneities in the CCD taper. This tool processes image as a whole and is based on the iterative Brückner algorithm that enables to robustly remove any smooth varying components as background for 1D 2θ XRD scans [56]. We have generalised it in 2D by taking sequentially 2 passes: the first treats vertical and the second horizontal lines. After these 2 passes, we keep for each pixel background value the minimum of the 2 values found, and we stop iteration when the maximum intensity correction of an iteration drops down below 1. Overall, figure 35 illustrates the efficiency of our background

removing routine that was able to divide background level by a factor of 10! We thus achieve an excellent final precision which is found to be $\pm 1/20^{\text{th}}$ and $\pm 1/10^{\text{th}}$ of pixel along x and y.

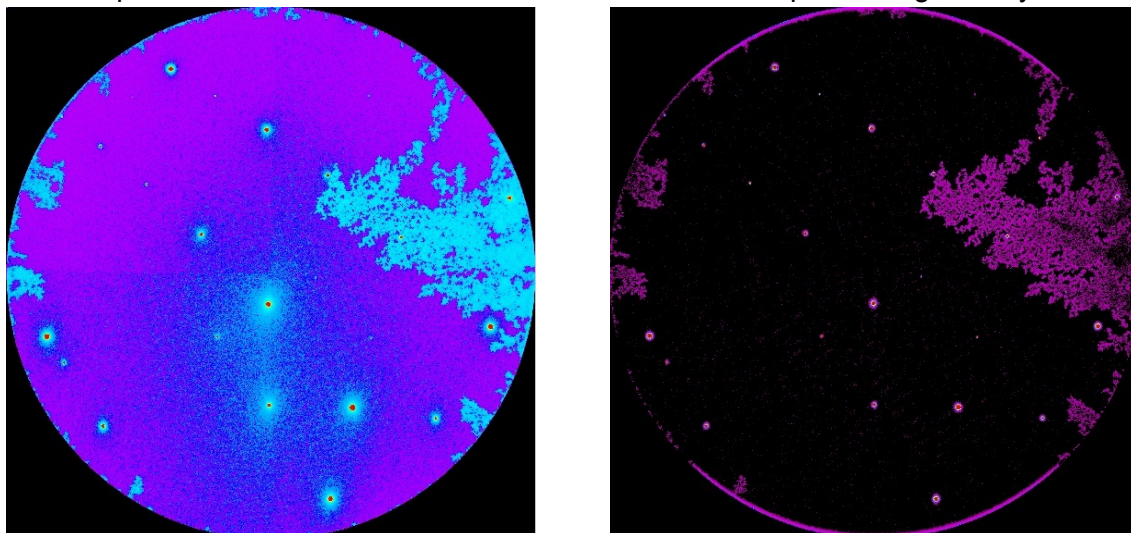


Figure 35: Comparison of the same image with the same logarithmic intensity scale before (left) and after (right) background removal thanks to the 2D generalised Brückner algorithm: background level estimated from signal between peaks goes from 66 initially down to 5.5!

And again in an effort to define at best the diffraction peak intensity repartition, we decided for each measurement point of the sample to record and average 4 images without changing any parameters, thus increasing by a factor of 2 the signal-to-noise ratio.

III.3.1.3 Sample positioning

For our sample, X-ray attenuation length varies from 2 to 150 μm with energy as shown on figure 36. As in the usual μLaue setup, the sample is placed at 40° relative to the beam (see II.1.1), we cannot keep a submicronic precision on the sample unless the sample is thin enough. But this is not possible here since our layer typical thickness is of 6.5 μm : consequently, we placed the sample perpendicular to the X-ray beam, thus keeping a submicronic X-ray beam positioning precision and recording data taking 2D raster scans as shown on figure 37. Please note that this argument is quite general for μLaue since — with our large incoming X-ray energy range [5-23] keV — whatever the detailed sample constituents, its attenuation length is typically larger than 1 μm and varies at least by a factor of 10 on the full energy range.

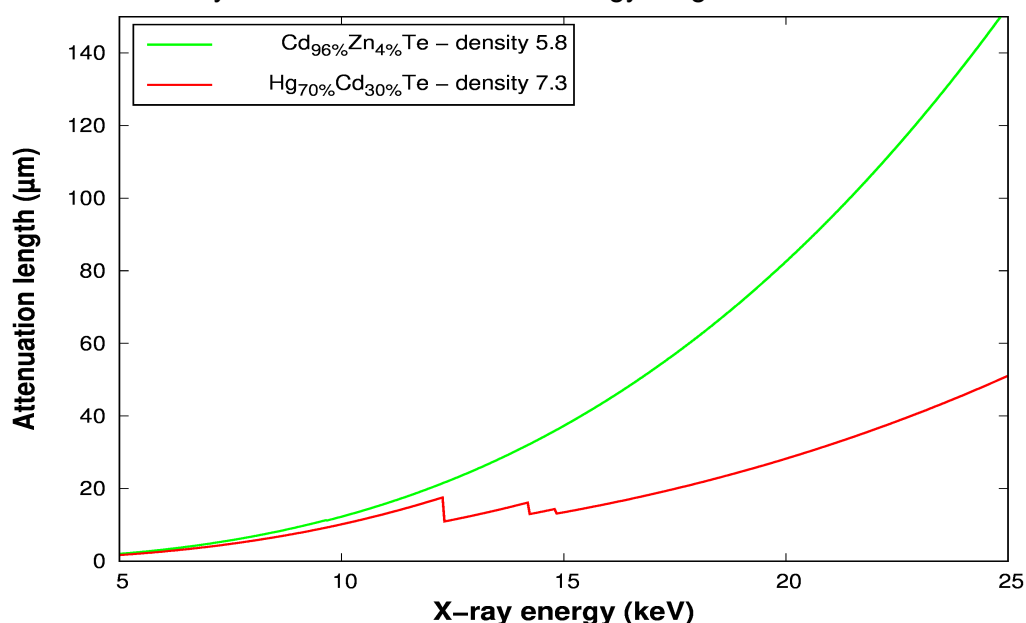


Figure 36: Attenuation length of X-ray in substrate ($\text{Cd}_{96\%}\text{Zn}_{4\%}\text{Te}$) or layer ($\text{Hg}_{70\%}\text{Cd}_{30\%}\text{Te}$) as a function of energy. Layer shows three drop-downs reflecting L_I , L_{II} and L_{III} absorption edge of Hg.

Consequently, all our samples must be cleaved before they are studied. Pressing with a diamond tip on the reverse side of the sample, we reveal easy cleavage directions: we then choose one that cleaves perpendicularly to the sample's plane. All our samples are thus cleave along the same plane and ensure to minimally disturb its strain state.

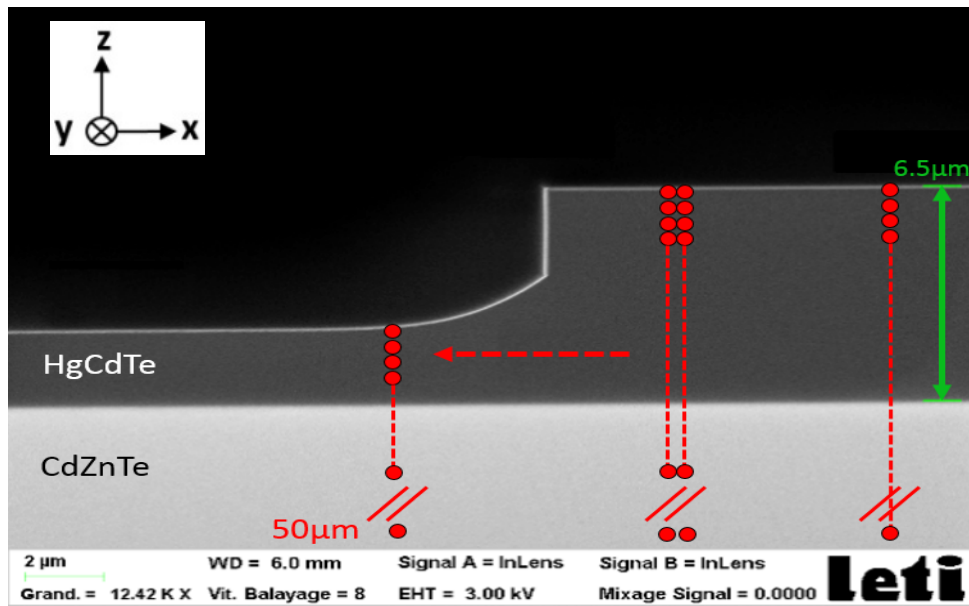


Figure 37: 2D raster scan shown in red dots on a 4 μm deep trench realised on a 6.5 μm HgCdTe layer grown on the CdZnTe substrate. The trench lower corner is rounded because the rotating 35° ion milling is partially shadowed by the deposited protection resin.

III.3.1.4 Camera calibration

The necessity to calibrate the CCD position (see II.1.3) is another source of precision loss. Indeed, to achieve this calibration, we use a dedicated reference sample of unstrained monocrystalline Germanium. But to get the X-ray beam on this reference sample, we have to move the ~2 kg of the sample holder on typically 10 mm. Well, despite this change seems neglectable compared to the ~150 kg mass that the anti-vibration table supports, it is no more the case when chasing 10^{-5} resolution. Indeed, the induced longitudinal and lateral angular inclinations of the table can't be neglected despite our high-performance 10nrad precision closed-loop feedback system on the longitudinal inclination: CCD camera relative position to sample and reference sample are not sufficiently close. We must find a reference much closer to the sample.

Dislocation density of our samples was measured using the etch pit density technique which consists in using a specific chemical solution whose etching speed is enhanced by dislocation thus converting them into holes. A subsequent counting under optical microscope shows that our substrate / layer possesses a very low 10^{4-5} cm^{-2} dislocation density. High Resolution X-Ray Diffraction (HRXRD) measurements shows that CdZnTe wafers possess a quite compact rocking-curve since its full-width at half-maximum (FWHM) is lower than 15 arcsec. Finally, as our 6.5 μm thick HgCdTe only supports low strain, we will reasonably assume that our substrate is completely unstrained sufficiently below the interface. Therefore, we will completely avoid having the sample holder travelling several millimetres by taking reference measurements made directly onto our sample, just 50 μm below the interface (see figure 37)!

III.3.1.5 The latest tweaks to achieve 10^{-5} resolution

Whatever precautions are taken (experimental room temperature regulated at $\pm 0.1^\circ\text{C}$, close-loop feedback on motor position using rotary encoder, anti-vibration support, longitudinal inclination stabilisation at 10 nrad ...), there will always be some long term drift. As reference measurements are taken very close to measurement zone, we decided to complete each vertical line measurements by a reference measurement. And indeed, the long-time drift is clearly visible on figure 38, where we have calculated at each recorded reference position the overall translation and rotation of diffraction peaks relative to the first measurement. Despite position and rotation drifts

are really small on this 10 H long experiment, they must be compensated for to achieve our goal: each measurement is referred to the corresponding interpolated reference point position. Finally, we have to make a strict selection on the diffraction peaks we take into account. Indeed, — and this is a specificity of synchrotron beam — because our X-ray beam contains a large [5-23] keV energy range, it is always possible that a diffraction peak is in fact the superposition of the lowest fundamental energy with its higher energy harmonics 2, 3 or even 4. When referring only to the Bragg law, harmonics are perfectly superimposed on the fundamental. But the dynamical theory of diffraction shows in fact that harmonics have lower Darwin width and do not exactly diffract at the same Bragg angle, this effect being currently used at ESRF to enhance monochromator's harmonics rejection using a slight angular detuning [57]. Consequently, diffraction peak with harmonics are in reality the superposition of peaks of different energies that are not exactly at the same position, not to mention the fact that high order peaks present higher sensitivity to strain than low order one: clearly, we must select only harmonics free diffraction peak.

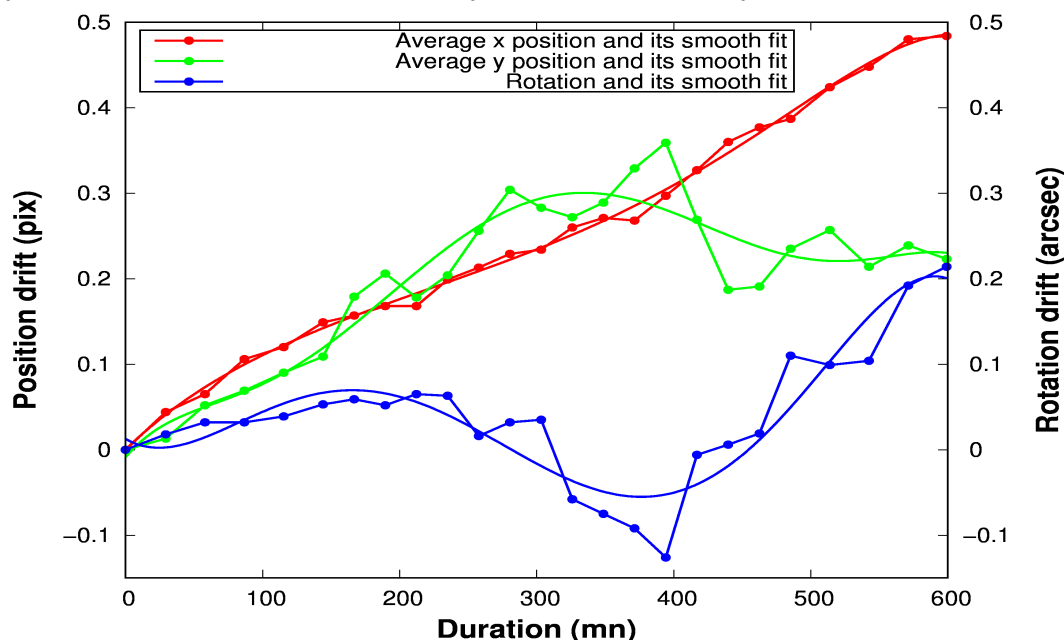


Figure 38: Evolution on reference measurements of the 10 recorded diffraction peaks average positions (x,y) and rotation with time on a typical 10 h long experiment (sample 16703-F). Smooth fits are used to compensate these drifts: difference with values is used to estimate our individual diffraction peak fitting precision, which is found to be $\pm 1/20^{\text{th}}$ and $\pm 1/10^{\text{th}}$ of pixel along x and y .

III.3.2 Validation of our strain measurement method

Now that we have clearly defined data treatment and the necessary steps in order to reach our 10^{-5} precision goal, we may proceed to determine the deviatoric strain tensor of our samples at each measurement point, thus showing a 2D map evolution of strain inside sample as was done in II.2.1 and II.2.2. This classical proceeding way has the undeniable advantage of making no assumption on the nature of strain in the sample. But it has the corresponding drawback: its precision is not sufficient for us. This comes from the fact that deviatoric tensor determination requires first to calibrate the CCD position (5 parameters) and this is far less precise than the peak position determination even if reference points are taken at a $50 \mu\text{m}$ depth inside substrate. Once CCD calibrated, we will have to compare calibration with current measurement: in this comparison, we cumulate a large imprecision that corresponds to the calibration of the camera from reference point measurement and the second from the measurement itself. The best we could do is to directly compare two measurements. Well, this is possible provided we first make a hypothesis on the nature of the strain. As our sample are made of an epitaxially deposited layer on top of substrate with a quite low mismatch ($< 3 \cdot 10^{-4}$), we will naturally assume that the strain is bi-axial as represented figure 39. Therefore, any strain in the layer will manifest itself as tensile or compressive depending on whether the layer unstrained lattice parameter a_0 is smaller or larger than the substrate lattice parameter a_{sub} : the mismatch between layer and substrate is defined as

$\varepsilon_{||} = \frac{a_0 - a_{\text{sub}}}{a_{\text{sub}}}$. Consequently, a positive (negative) mismatch will only affect the layer c'-axis that will be dilated (contracted) compared to the c-axis of the substrate (sample c-axis is identical to the z-axis of the sample referential as shown in figure 37), and we defined the strain along z as $\varepsilon_{zz} = \frac{c' - c}{c}$. Diffraction plane sees its angle relative to the interface plane (x,y) changed from α to α' , thus modifying the position of the corresponding diffraction peak on CCD camera. From simple geometrical considerations, we deduce that $\varepsilon_{zz} = \frac{d' - d}{d}$. This means that the strain may be deduced directly from relative diffraction position change without any need for CCD camera calibration, which is the best situation.

Diffraction peak position on CCD

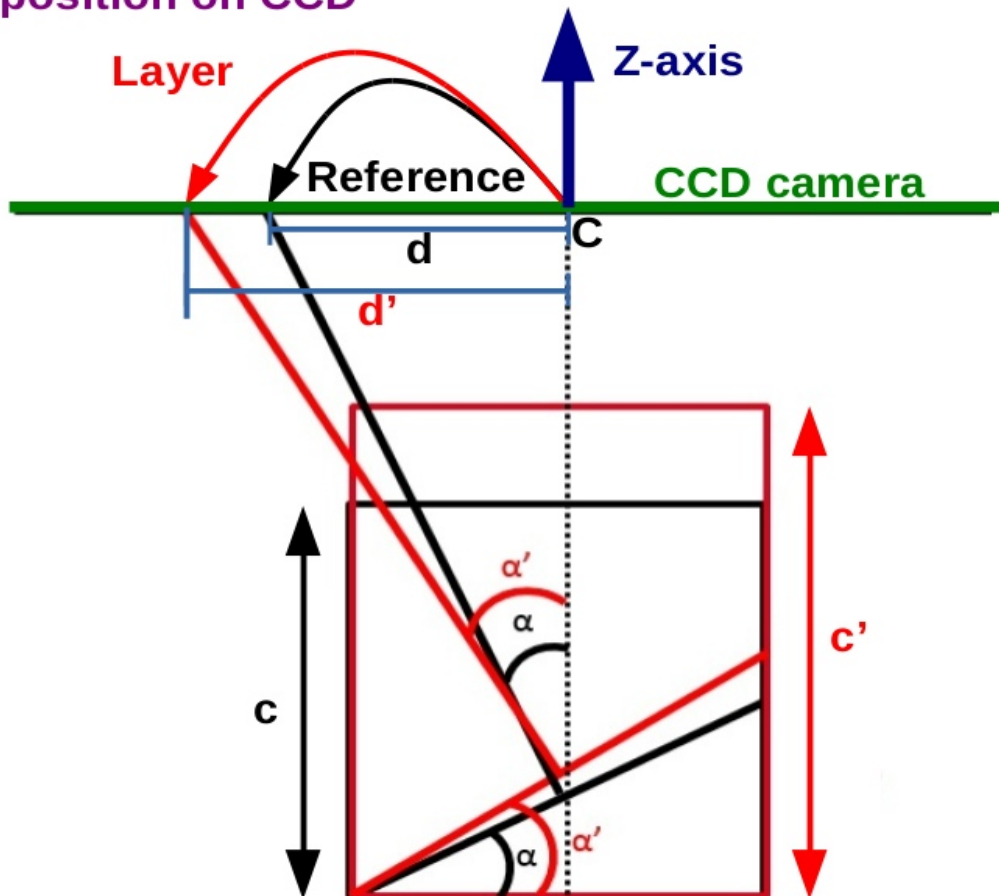


Figure 39: Bi-axial strain represented in the plane formed by the Z axis and the diffraction direction vector. The unit cell of layer (red) is stretched along z from c to c' compared to the substrate one (in black), leading to a diffraction plane angle that changes from α to α' .

Bi-axial figure 39 was represented as a projection in the plane defined by the Z axis and the diffraction direction vector but it is in fact valid whatever plane containing the Z-axis. Obviously, we will select the xz plane because our best diffraction peak positioning precision is along the x-axis. Consequently, for any depth in the sample, we simply evaluate $x_{\text{peak}} - x_{\text{ref}}$ as a function of x_{ref} for each diffraction peak. We logically found that these results are aligned and the slope gives us the local strain!

To check our method, we have compared its results to HRXRD. For that purpose, we have selected three reference samples of various positive and negative mismatches that have undergone no further processing than layer deposition. Because HRXRD is not depth resolved, we checked that peak x positions do not change in the whole layer thickness. We then estimated the slope average value on the whole layer thickness to deduce strain presented in table 11. Clearly, the

excellent agreement at $\pm 10^{-5}$ between the two methods validates ours and shows we were able to successfully combine depth resolution with strain resolution.

Sample	A	C	E
HRXRD (10^{-4})	2.1	-1.9	-1.0
Slope (10^{-4})	2.0	-1.7	-1.1

Table 11: Comparison between HRXRD measurements and our method on our three reference samples

III.3.3 Sb-doped and annealed sample

Let us now apply this method to a complex sample, the 27937-D. This sample is made of an $5.0 \mu\text{m}$ thick epi-layer of HgCdTe grown by MBE presenting a $3 \pm 0.5 \cdot 10^{-4}$ mismatch. It was implanted on an $8 \mu\text{m}$ width band with Sb^+ at 360 keV with a dose of $2 \cdot 10^{14} \text{Sb} \cdot \text{cm}^{-2}$ and underwent a 5 H activation annealing. Applying the method described previously using 11 diffraction peaks regularly spaced along x and averaging data on the central $6 \mu\text{m}$ (13 measurements lines), we finally obtain figure 40. And the strain evolution with depth in red presents a lot of interesting features that we will comment going from right to left.

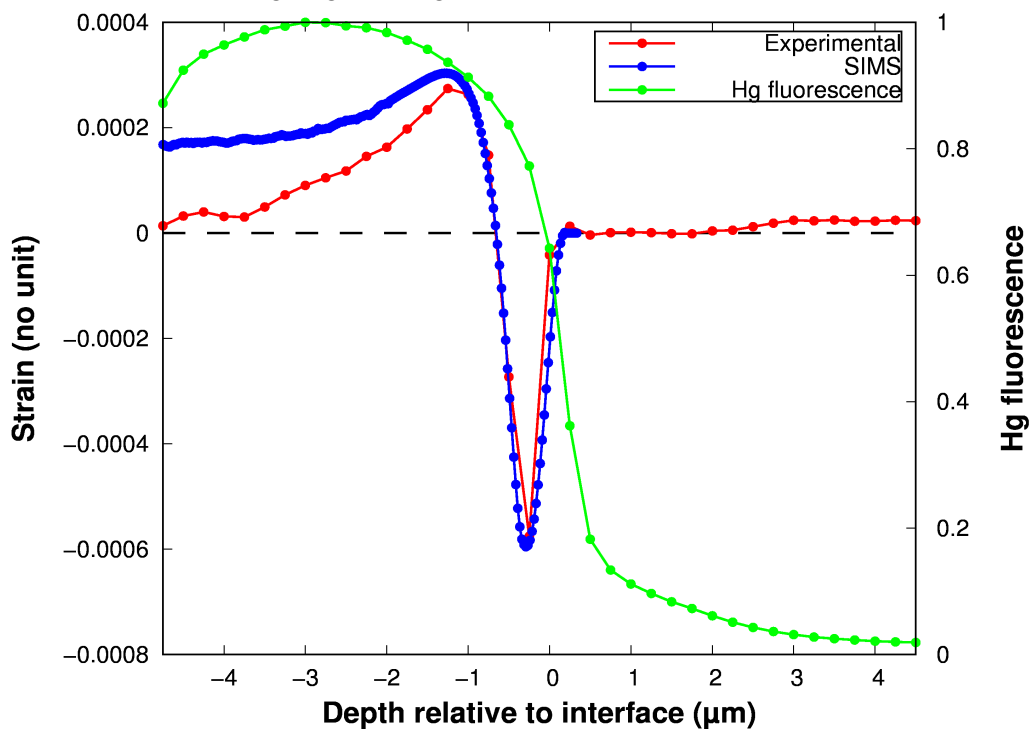


Figure 40: Evolution of strain as a function of depth as determined by μLaue (red). Comparison with expected strain from local composition of quaternary HgCdZnTe as determined by SIMS. Hg fluorescence shows interface position.

First in the substrate zone (positive depth), we expect a constant and null strain. And indeed, we find a $1.1 \pm 1.3 \cdot 10^{-5}$ strain, thus confirming the absence of strain inside substrate. Moreover, this shows that we have been able to reach our quite ambitious 10^{-5} precision determination of strain with a measured $\pm 1.3 \cdot 10^{-5}$ precision.

Secondly, with a positive $3.0 \pm 0.5 \cdot 10^{-4}$ mismatch, we would expect a positive strain inside the layer: the most spectacular feature is this unexpected huge negative strain found right onto the interface! Clearly a dedicated effect occurs specifically on the interface leading to a huge contraction of c-axis right at the interface while c-axis becomes positive again once outside this $1 \mu\text{m}$ thick interface zone as expected. Moreover, this strain is way too high compared to the elastic limit of HgCdTe ($3 \cdot 10^{-4}$) but could be easily supported by CdZnTe. This spectacular effect was caused by the 5 H annealing of the sample: it has induced a Hg exo-diffusion from layer to substrate and reciprocally the exo-diffusion of Zn from substrate inside layer, creating a quaternary HgCdZnTe

around interface. This seems promising since Zn replacing Hg will reinforce the elastic limit of layer and shorten its lattice parameter. Using the local composition of Hg, Cd, Zn and Te obtained thanks to SIMS measurements, we have estimated the local lattice parameter and therefore deduce the expected bi-axial strain evolution as represented in blue on figure 40: there is a remarkable matching between absolute values of strain as expected from local composition⁷ and measured with μ Laue. The huge negative strain found at interface comes from evolution of the local lattice parameter with sample composition.

Finally, we observe that the strain perfectly follows the compositional strain from substrate, through the interface until 1 μ m inside layer. But further away, strain is much smaller, goes down to zero and stays at zero as soon as 3 μ m after the interface. Clearly, a new effect is killing the strain, and we believe this is related to dislocation creation. And indeed with a $3 \cdot 10^{-4}$ mismatch, the critical thickness [58] of HgCdTe growth on CdZnTe may be estimated to 0.75-1 μ m (refer to [46], chapter 1.3.1.2 for a detailed calculus), a value coherent with our measurement. Please note that the critical thickness also clearly delimit the range of validity of our bi-axial hypothesis. We also see that 3 μ m in the layer, there is no more strain and therefore no more driving force for dislocation creation: the 1 μ m of epi-layer situated under the surface of the sample appears free of strain.

As a conclusion, we have been able to measure the local strain of our sample with a $\pm 1.3 \cdot 10^{-5}$ precision and a 250 nm depth resolution. Comparison between expected compositional strain and actual strain shows the sample is perfectly biaxial from substrate to interface and 1.0 micron inside layer, thus measuring our sample's critical thickness. Then follows a 3 μ m thick zone where strain induces the formation of dislocations which finally fully relaxes the epi-layer. Therefore, after 4 μ m, the epi-layer is fully relaxed and the 1 μ m of epi-layer situated under the surface of the sample are free of strain.

III.4 Local orientation

From a general point of view, the positions of the diffraction peaks measured by the μ Laue experiment provide information on both the local shape (deviatoric strain) and orientation of the unit cell. To locally measure the strain in the case of the bi-axial hypothesis, we have considered the xz plane and evaluated along the x-axis the difference between local and reference position $x_{\text{peak}} - x_{\text{ref}}$ for all diffraction peaks as a function of x_{ref} . These differences form a straight line whose slope is the local bi-axial strain. But we may also be interested in the evolution of the local average value of these positions.

Indeed, if locally the crystal is slightly rotated, all diffraction peaks will be displaced as a whole⁸. Consequently, evolution of the average diffraction peak position along x (respectively y) shows local crystal rotation inside the xz (respectively yz) plane. Please note that this measurement is naturally sensitive to long-term drift, making it mandatory to take regular reference measurements.

Along X

Along X, there are no specific corrections to be made.

Along Y

Along Y the situation is far more complicated than along X. If we consider the case of our sample where there is a good match between layer and substrate, we observe that the diffraction peak Y position changes brutally when going from substrate to layer. Photon diffraction occurs all along the trajectory of the X-ray inside sample and on average along Y, the corresponding diffraction peak will appear as emitted from a certain distance from the entrance which — by definition — is the attenuation length. Consequently, as the attenuation length depends not only on the energy but also on the nature of diffracting material (refer to figure 36), the Y position will vary brutally when going from substrate to layer, the awaited jump in Y position being the difference in attenuation length. And indeed this is what is found as shown on figure 41. Clearly, this effect leads to an

⁷ SIMS depth precision is 10 nm, data were convoluted with a 500 nm gaussian to match μ Laue beam size

⁸ If rotation is small enough, the parallax deformation is neglectable

important correction that must be precisely implemented if we want to get meaningful measurements.

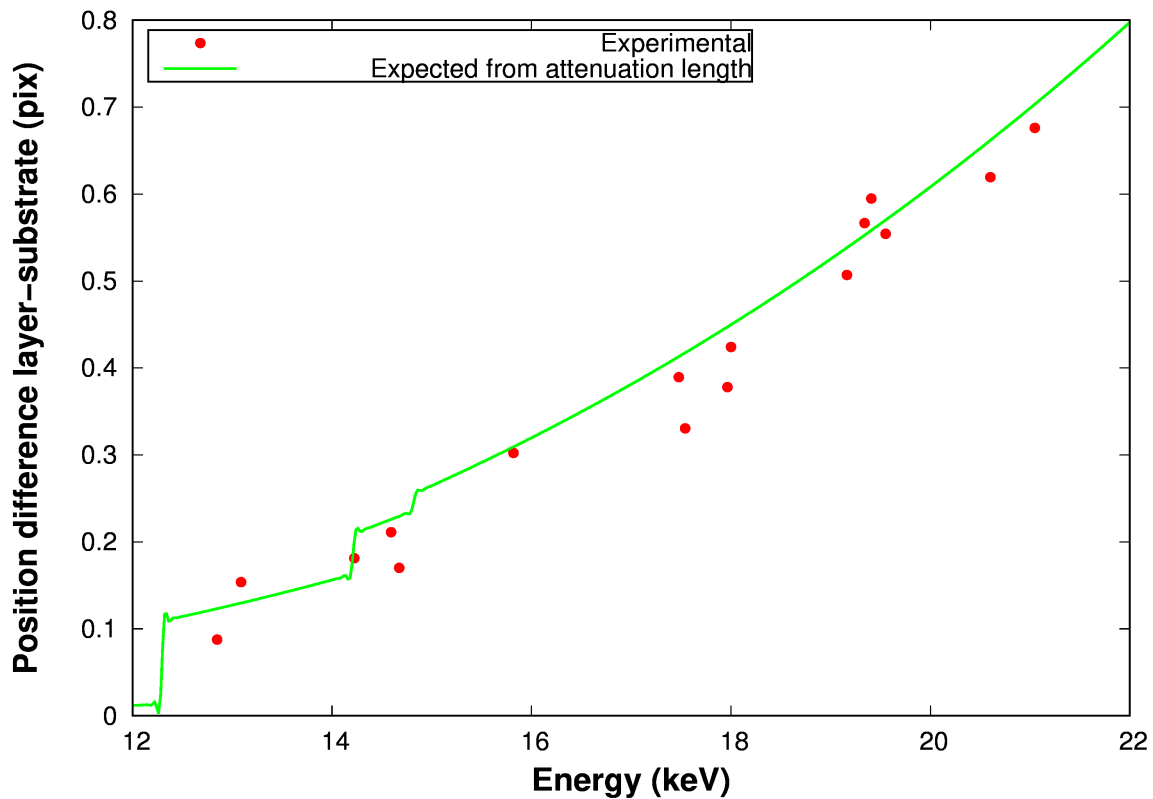


Figure 41: Origin of the position difference along y between layer and substrate for sample 27937-D

But it is not obvious to make precise correction since attenuation length are dependent on the precise composition of material that is on the sample's Zn, Hg and vacancies ratios. Moreover, these composition variations influence the density of the material, another value that is difficult to measure once sample is realised. Overall, I estimate this leads to a $\pm 5\%$ uncertainty on attenuation length. This partially explains why on figure 41, the foreseen correction (green line) doesn't nicely go through all the points but rather seems slightly above them. Nevertheless, the correction is quite efficient and satisfying.

Since position along Y depends on attenuation length, the interface region where we observe large variations of Hg and Zn fractions is sadly almost impossible to correct from the attenuation length effect.

And last but not least, because our sample is placed perpendicular to the incoming beam, diffraction peaks must be split into two different categories: direct and back-diffracted ones. Back-diffracted peaks are diffraction peak emitted in the opposite direction of the incoming beam while the direct ones go in the same direction as illustrated on figure 42. The X-ray beam attenuation length has been represented with a blue dashed line: photon diffraction occurs all along this line. If we now consider diffraction that occurs near the entrance, back-diffracted peak will escape throughout the entrance plane while direct peak still have to go through all the sample thickness until the sample's surface. Therefore, the output length of back-diffracted peak is considerably lower than the constant direct one and their intensity is therefore enhanced relative to the direct ones.

Consequently, for back-diffracted peak, there is an enhancement of the low penetration depth signal: back-diffracted peaks appear as if they had a smaller attenuation length than their direct counterparts. And this effect is all the more important that energy is low or the incoming beam is far from sample's surface. Simple 3D analytical trajectories calculations are necessary to really quantify this effect and — without giving any boring details here — they show that maximal correction occurs for our back-diffracted low-energy reference points measurements with a position correction of $15\ \mu\text{m}$, comparable to their $20\ \mu\text{m}$ attenuation length. And we expect to be able to take advantage of this property where — by varying the X-ray beam distance to the sample's surface — we may modulate at will the equivalent attenuation length.

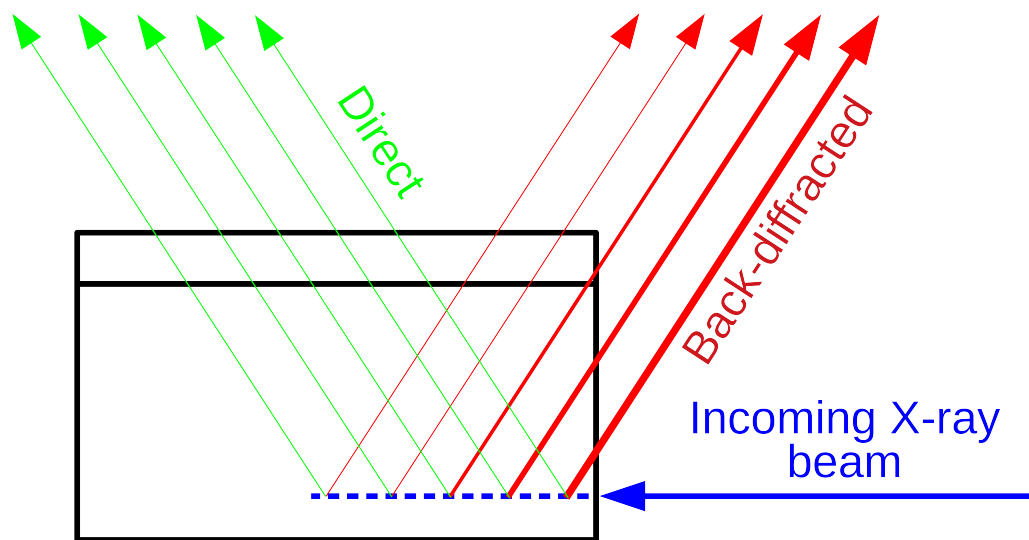


Figure 42: Diffraction peaks splitted into direct (green) and back-diffracted (red) categories, the output intensity being represented by line thickness. X-ray beam penetration length is represented with a blue dashed line.

Overall, we have identified two important corrections to be applied to the Y position of diffraction peaks. But these corrections are hard to be made precise: the first correction requires to precisely determine the attenuation length which varies with density as well as local Zn / Hg / vacancies fractions while the second one is highly dependent on an eventual angular tilt or raw of the sample relative to the incoming beam. Because of these specific difficulties, Y position corrections are not yet fully validated and made robust so that I choose not to present any results yet despite promising primary results on strain versus rotation repartition were obtained (please refer to chapter 5 of [46]).

III.5 Overall comparison between local strain and orientation

If along Y, data processing still requires some developments, it is not the case along the X direction where results are available. As local orientation using X position tells us about rotation in the (xz) plane, this measurement is perfectly fitted to study fully processed samples with etched pixels as shown on figure 37. More precisely, we decided to individually asses the influence of the three major technological processes that are sequentially applied to full-plate sample to obtain IR photodiodes: dry-etching, surface passivation and annealing.

To fulfil that goal, we decided to use the same $1.0 \cdot 10^{-4}$ matched full-sized $6.5 \mu\text{m}$ HgCdTe/CdZnTe plate (number 16703) to process our three samples. This plate was obtained using the reference process to produce IR photodetectors, that is the Liquid Phase Epitaxy (LPE). As LPE requires a much higher substrate temperature than MBE during growth, LPE samples always possess a graded compositional interface originating from thermally induced Zn and Hg exo-diffusion during growth, even in the absence of subsequent annealing. A $4 \mu\text{m}$ deep, $8 \mu\text{m}$ wide and $100 \mu\text{m}$ long trench was first etched to realise the 16703-G sample, etching was followed by the deposition around 80°C of a small passivation layer to make the 16703-A sample and finally a 400°C annealing⁹ was performed to obtain sample 16703-F, the sample that is closest to a photodiode.

Figure 43 shows obtained results on our three samples (one per column). Results are divided in two lines: the upper line shows the comparison of the 2D rotation repartition near the trench using the same ± 80 arcsec colour rotation scale as shown on the right while the lower line shows strain repartition using a $\pm 7 \cdot 10^{-4}$ strain scale.

⁹ Passivation is necessary prior to annealing to avoid any massive Hg exo-diffusion

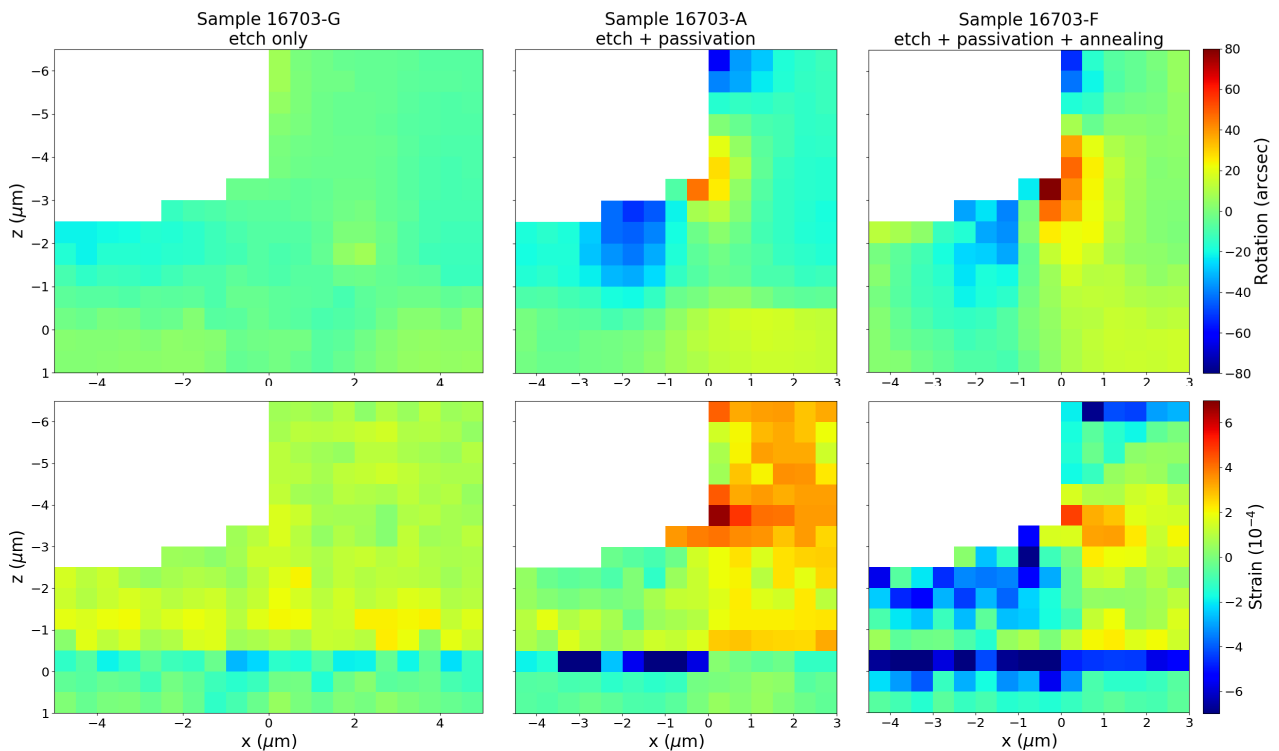


Figure 43: Comparison of the 2D repartition of the local (xz) orientation (upper line, rotation angle scale shown on the right) and local strain (lower line, strain scale on the right) of our three samples 16703-G, 16703-A and 16703-F to individually assess the effect of the three main technological processes of etching, passivation and annealing.

As LPE samples present a graded compositional interface originating from thermally induced Zn / Hg exo-diffusion during growth, their strain evolution around interface is quite similar to annealed MBE (see figure 40): interface (corresponding to $z=0$) appears as a large negative drop-down in strain that is visible on all three samples. After passivation, it is much more intense underneath the trench while annealing makes it perfectly visible on the full sample width with even an enlargement underneath the trench, this enlargement being attributed to a supplementary thermally induced Zn / Hg exo-diffusion.

Looking now to the non-etched part ($z=[-3;-6.5]$ μm), similar effects are found. Etching doesn't affect strain that is found constant at $1.0 \cdot 10^{-4}$ like in the full-plate sample. In contrast, passivation makes strain very high (on average we are near the upper elastic limit $3.5 \cdot 10^{-4}$) and clearly not homogenous with maximal strain observed at top and bottom corners of the side of the photodiode. Finally, annealing makes strain go down until recovering low strain level apart for the top and bottom corners of the side of the photodiode.

Overall, this clearly shows that etching the sample doesn't modify inner strain, that strain builds up into our sample because of the sole passivation while annealing enables most of the photodiode part to release this strain. Of course, passivation has long been known to induce strain because HgCdTe and passivation layers don't have the same coefficient of thermal expansion: during the cool-down following deposition, a differential contraction will occur, macroscopically bending the sample with a measured 1-10 μm deflection for 30 mm long slices. What is new here, is the quantitative local measurement of this strain, its non-homogeneous spatial repartition and most importantly its release by annealing. An annealing that seems to partially free the non-etched part from strain by sending it at the bottom corner. We also observe highly negative strain at the top of both non-etched and etched zones where passivation layer thickness is maximal: we may wonder whether this highly negative strain doesn't come from an interdiffusion between passivation and HgCdTe layer.

If we now look at the rotation graphs, we clearly see that there is no rotation when going from substrate to layer through the interface whatever the sample: a result perfectly coherent with our bi-axial hypothesis. It also appears that etching has no influence on rotation while passivation mainly reveals top and bottom corners with a large -60 arcsec counter-clockwise rotation at the top and a symmetrical +60 arcsec clockwise rotation at the bottom. Annealing seems to diminish the

counter-clockwise rotation of top corner (as well as the secondary rotation area in the trench region) but enhances the bottom rotation which coincides with maximal residual strain: clearly it is the bottom corner that is the main point of concern for IR photodiode since it cumulates both maximal strain and rotation.

To complete this study, we have recorded data situated 12 μm inside the non-etched zone in an attempt to measure our samples should there be no trench as presented figure 44.

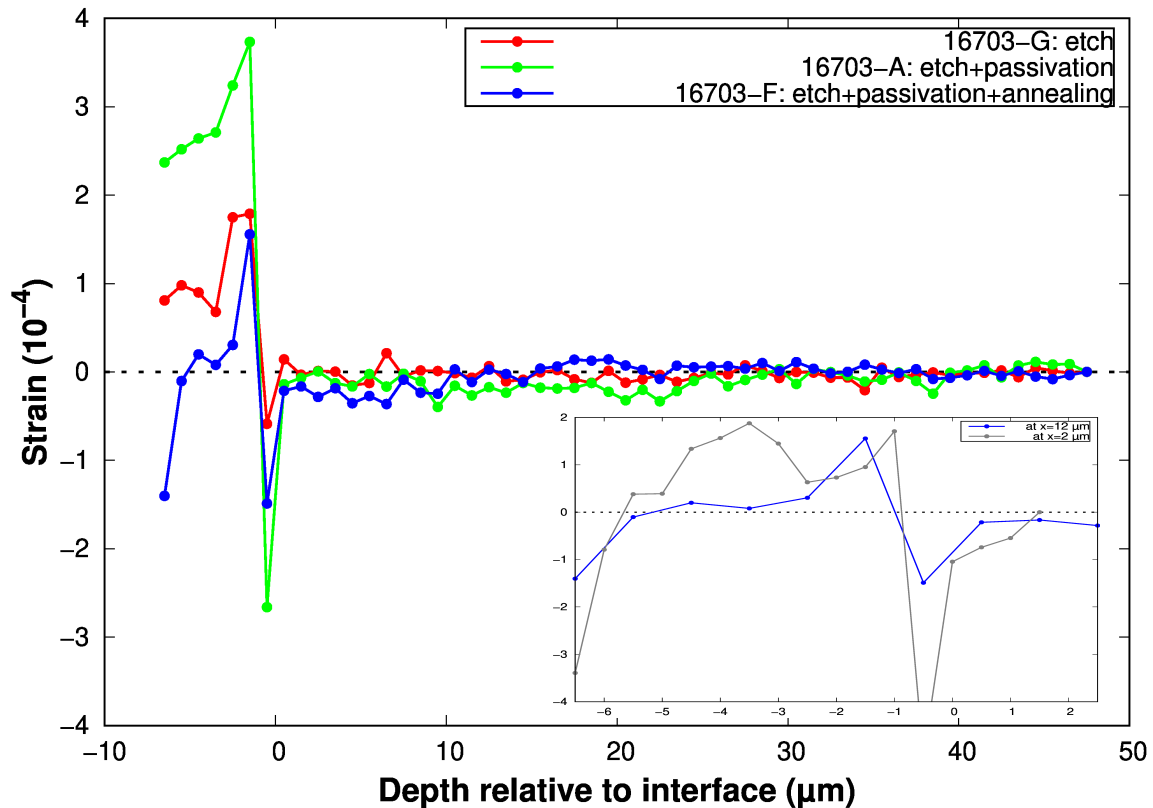


Figure 44: Main graph shows a strain measurement comparison 12 μm inside non-etched area for our three samples. The insert compares it to a closer 2 μm inside non-etched area for the 16703-F

The first striking feature is that as soon we are into the substrate, strain is found equal to 0 (at $\pm 1.4 \cdot 10^{-5}$) for our three samples: our substrate stays unstrained. The graded interface is also clearly visible under the form of a sequential large negative then positive strain as in the case of annealed MBE sample (see figure 40): graded interface is found to be 2-3 μm thick. Secondly, we clearly observe the huge raise in strain induced by passivation (green curve) as well as its zeroing by annealing (blue curve). This zeroing is only partial here since a large negative strain remains for the 1 μm situated underneath the passivation layer as already seen but also because a positive $1.8 \cdot 10^{-4}$ strain bump centered around $z = -4 \mu\text{m}$ exists at 2 μm inside non-etched zone as shown in the insert. Thirdly, strain inside layer becomes zero thank to the annealing (blue curve) while it had a constant value of $8.5 \pm 1.5 \cdot 10^{-5}$ at start (red curve). And this is quite a difference with MBE sample (see figure 40) since for MBE sample, the strain naturally goes down to zero. This indicates that strain generates far less if any dislocations in LPE grown sample compared to MBE which is a very favorable case for IR photodiodes.

Overall, these results enabled use to clearly separate the influences of each of the three main technological processes of etching, passivation and annealing. They showed that our substrate remains perfectly unstrained, that etching has no influence, that strain originates from passivation while annealing (whose primary goal is to electrically activate implanted dopants) tends to zero it in the final photodiode except in the vicinity of the bottom corner of the trench.

IV Research perspectives

One of the most promising axis of research for me is the study of the extrinsic p-type doping of HgCdTe. Indeed, the extrinsic p-type doping is still nowadays the main limiting factor for IR detector performances since this kind of doping would allow to rise the detector working temperature from liquid N₂ (77 K) to 150 K without impinging performances, thus matching requirements of the next third-generation detectors.

Discussing with C. Lobre from LETI with whom I had already cooperated on As implantation doping [48], it seems pretty obvious that the dopant of choice would be Sb, a dopant we have already studied in III.3.3 dedicated to sample 27937-D. Clearly in that study, μ Laue has provided highly valuable informations while opening the possibility to answer numerous interesting questions. With C. Lobre, we think it is pertinent to develop a collaboration with the aim to answer these questions that are still opened nowadays.

However, we still need an as much defect-free layer as possible to ensure optimal collection of charges so that no breakthrough can be made without a deeper understanding of the HgCdTe/CdZnTe material. A particular focus needs to be made on the strain gradient and critical thickness inside the HgCdTe layer. And speaking with P. Ballet from LETI who is a renown specialist of MBE grown samples and with whom I've been collaborating for more than 10 years now, it is almost impossible to measure the critical thickness of HgCdTe / CdZnTe with classical RHEED means because the mismatch is almost zero ($<3 \cdot 10^{-4}$). The μ Laue gives us a major advantage here since we may determine the critical thickness, that is the depth of the defect-free zone!

IV.1 Technical developments to study the relaxed zone

If we come back to chapter III.3.3 which is focused on the interpretation of figure 40, we have seen that the bi-axial hypothesis seems no more valid beside 1 μ m over the interface. Therefore, how do we interpret the null slope for the 1 μ m epi-layer at the surface of the sample? This indicates that the x position of the peaks at the surface of the epi-layer are the same that those of the unstrained substrate. μ Laue experiments being insensitive to any hydrostatic strain, we deduce that the surface of epi-layer is free from any deviatoric strain: epi-layer surface has the same crystal structure that unstrained substrate, only the lattice parameter may have changed. This probably indicates here that the epi-layer has reached its unstrained lattice parameter which — since the mismatch is $3 \cdot 10^{-4}$ — is expected to be $3 \cdot 10^{-4}$ larger than the lattice parameter of substrate.

Of course, we would like to check this hypothesis and for that purpose, we have to render μ Laue experiments sensitive to hydrostatic strain. If μ Laue is insensitive to hydrostatic strain, it is because the CCD camera does not determine peak energy. And when we build the μ Laue station, we kept the possibility to insert our beamline's monochromator in order to send a monochromatic beam through the μ Laue setup. But after numerous attempts, this solution was discarded as non-practical: when going from white beam to monochromatic, the mirror heat loads suddenly dropped down to almost 0 and the consecutive thermal drift prevented us for stabilising size and position of the microbeam even after several hours.

Another possibility would be to use an energy-resolved detector. But the required precision of typically 1 eV for 10 keV energy would require the use of analysing crystals or a dedicated specific monochromator which would look more like building a whole new setup instead of just adding an energy measurement possibility.

The favoured solution is a quite elegant one: it consists in putting in the white beam a rotating thin diamond blade, thus making a tunable multicolour 'rainbow' filter [59]. Because it is an unstrained monocrystal receiving a white beam, this diamond will induce several drop-downs (dips, see figure 45) of intensities in the incoming white beam whose well-defined energies may be calibrated as a function of the rotation angle. Rotating the filter, we watch for the apparition of dips in the diffraction peak intensities thus determining their energies. The main advantage here is that the thermal load

on mirrors doesn't really change with or without the diamond, thus preserving beam stability! This experiment has been successfully conducted several times already and may be considered as operational. Still, there is a non-neglectable difficulty in the fine energy calibration of the dips, the post-data treatment and most of all, this technique requires rotating on roughly a 5° range the crystal with a $1/100^\circ$ precision and taking images at each rotation angle of the diamond for each depth ... thus making it a very time-consuming experiment.

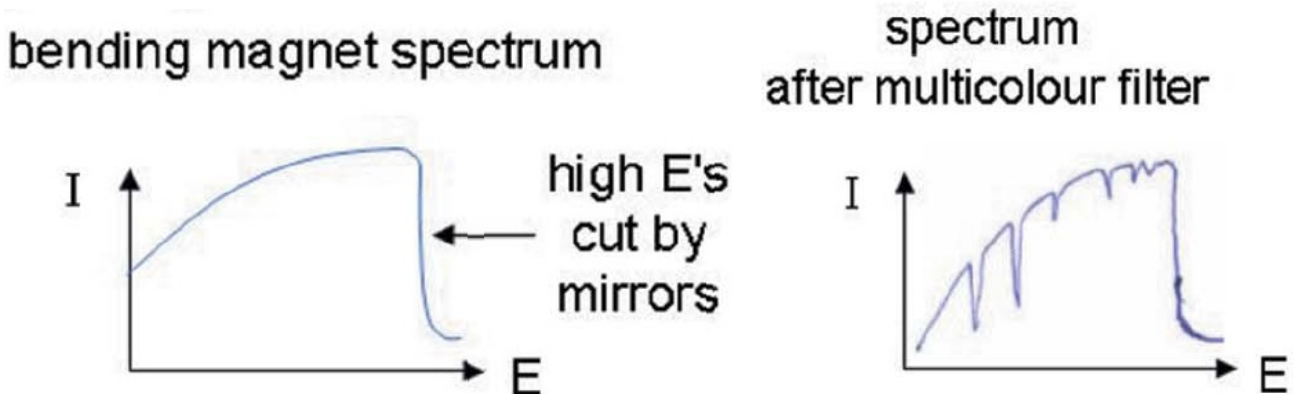


Figure 45: Effect of the diamond crystal (right) on the incoming X-ray beam energy spectrum (left)

In our case, we do not need to reach such a good precision as offered by the rainbow method but rather we only need to measure the *relative* change in energy of diffraction peaks going from substrate to the epi-layer. Indeed, the lattice parameter of substrate may be easily and very precisely determined before experiment using HRXRD and therefore it could serve as an energy calibration of peaks. The idea would then be to choose some diffraction peaks and record their energy spectra as a function of depth with our energy resolved detector [60]. Despite this detector cannot provide us with an absolute energy value, it may be sensitive enough to show a difference in the energy centre of spectra when scanning depth between substrate and layer. A second possibility would be to make these diffraction peaks go through the diamond crystal blade and simply scan it in rotation to measure the necessary angular rotation when going from substrate to sample's surface, this rotation measuring the energy offset.

IV.2 Defect-free and dislocation zones study

A nice asset of μ Laue is that it was able to show defects made to the crystalline structure. Indeed, μ Laue sees it through diffraction peak intensity reduction as we have very clearly seen on As-doped sample, see III.2.3 and figure 32. Moreover, thanks to weak diffraction peaks that are specifically sensitive to Zinc-Blende cfc sub-lattice mixing, we have interpreted the higher signal reduction of weak peaks compared to strong ones as the sign of the presence of misfit dislocation in the implanted zone. And we found out that both signal reductions disappeared after a 1 H activation annealing, thus showing the complete cure of epi-layer from implantation damages.

Now with strain, μ Laue provided a second tool to assess dislocation as we have seen on the Sb-doped and annealed sample, see III.3.3 and figure 40. Indeed, the difference between expected compositional and measured strain being null on roughly the first micron, this indicates that our $3 \cdot 10^{-4}$ mismatch sample presents approximatively a $1 \mu\text{m}$ critical thickness, beyond which in $3 \mu\text{m}$, the formation of dislocations will completely relax the epi-layer, thus leaving the last $1 \mu\text{m}$ at the surface completely free of strain, probably at its nominal lattice parameter, see figure 46.

Therefore, μ Laue provides us with the ability to study in details the evolution of both defect-free and dislocation zones as a function of any sample processing. And I think it is worth conducting these studies on both available type of samples, namely MBE and LPE since this will address different problematic either close to fundamental or applied research.

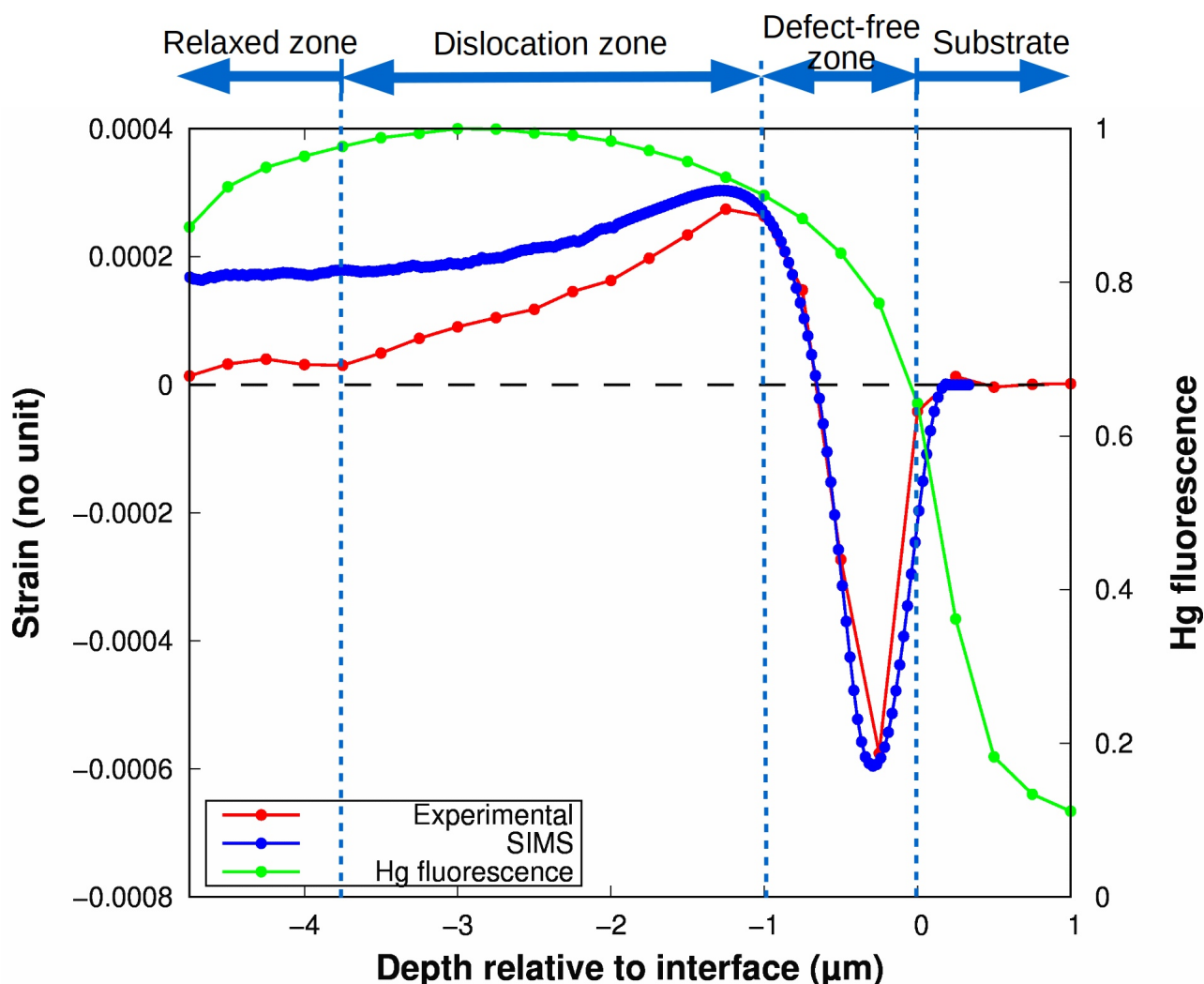


Figure 46: The successive zones constituting the Sb-doped annealed sample 27937-D

IV.2.1 MBE samples: fundamental research oriented

As already stated in the introduction, it is almost impossible to measure the critical thickness of HgCdTe / CdZnTe during growth using RHEED means since the mismatch is almost zero ($<3 \cdot 10^{-4}$), a 0.5% mismatch being at least necessary. Therefore, the μ Laue setup is a major asset here and it is really worth studying the critical thickness as a function of mismatch using the μ Laue setup. Nevertheless, when a sample is annealed, a compositional mixing appears. This compositional strain mainly comes from Zn exo-diffusing exponentially from 4% (SIMS shows this exo-diffusion concerns #250 nm in substrate) to 0% on a 1 μ m range. Thus, strain intermixing is superimposed on the defect free zone so that a precise measure of the defect free zone extension is difficult. Therefore, study of critical thickness requires that we work with not-annealed samples: this study is a fundamental research oriented one.

We will use MBE grown samples because we expect no composition inter-mixing between substrate and epi-layer, therefore the huge negative compositional strain should disappear. Consequently, the defect free zone would be made far more visible since it would not be superimposed with any compositional strain. And indeed, this is what we clearly see in figure 47! More precisely, we see at the interface a spectacular drop in strain (transition on 500 nm reflecting beam size), which goes from a constant 0 in the substrate to another constant $-1.95 \cdot 10^{-4}$ in the 2.5 first microns of the layer. This drop is followed by a rise of strain until reaching zero again when arrived at the free surface of the layer. This clearly shows that the substrate is indeed free of strain, that the critical thickness of a $-1.95 \cdot 10^{-4}$ strained epi-layer is 2.5 μ m, these 2.5 μ m being the defect-free zone of the layer. The defect-free zone is followed by a 1.75 μ m dislocation zone that releases strain until zero at the surface of the sample: μ Laue really provides us with extremely valuable and pertinent informations.

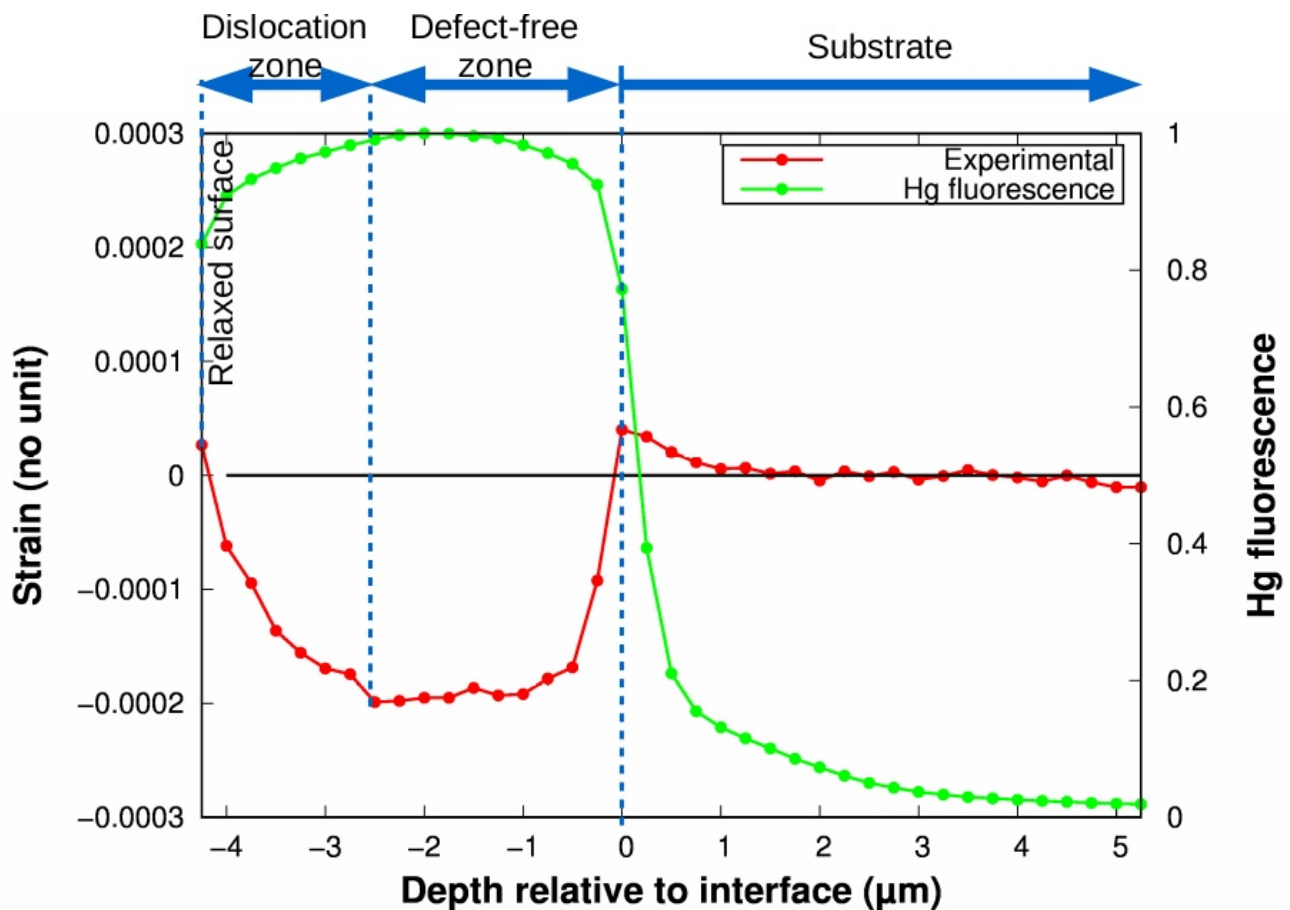


Figure 47: strain evolution as a function of depth for a 4.5 μm thick HgCdTe layer deposited by MBE, without any further processing (neither annealing nor implantation). The absence of compositional mixing at the interface enables to see very clearly the defect-free zone extension.

Looking deeper into details, we observe a very slight $4 \cdot 10^{-5}$ rise in strain that concerns the last 1.0 μm of substrate and symmetrically this effect is also visible in the first 1.0 μm of the layer: it is as if a slight drift in strain would occur specifically around the interface, a point worth looking into because if this drift wasn't present, the strain inside both substrate and layer would be absolutely perfectly flat.

Another interesting point arises when observing differences between figure 46 relative to a $2.5 \cdot 10^{-4}$ compressive strain and figure 47 relative to a $-1.95 \cdot 10^{-4}$ tensile strain. Despite a slightly larger strain, it seems that the critical thickness is much larger for tension than compression, which is a little surprising since elastic limits are larger for compression than for tension [53]: to get meaningful comparison, we must compare only not-annealed samples and check critical thickness evolution with strain. Once the relation established and compared with elastic limits, we may check on annealing effect on critical thickness and maybe confirm that annealing facilitates dislocation creation.

Concerning the dislocation zone, we logically observe that in both case, this zone has achieved the complete relaxation of strain. In the case of tension, we observe it is much shorter than in the case of compression. Nevertheless, the large critical thickness in the case of tension has made the free sample surface too close to the defect-free zone: we may logically infer that the close presence of the free surface has helped to release strain, thus considerably shortening the extension of the relaxation zone. To check that point, we need to work with dedicated not-annealed samples of high layer thickness (typically 10 μm).

Working with not-annealed samples, we could first study how the variation of the extension of this zone depends on the mismatch. In particular, the overall extension of the defect free and dislocation zones may well be only very slightly dependent of mismatch. Indeed, for high (respectively low) mismatch, we expect a shorter (longer) critical depth followed by a dislocation zone starting with a high (low) dislocation density. And if the dislocation driving force is the local strain, high mismatch sample will start with high density dislocations thus inducing a rapid fall-of of

strain compared to low mismatch. We may also wonder if this overall extension is smaller or larger than the epi-layer thickness. To that purpose, we will also compare its evolution either with or without any implantation. Indeed, as implantation generates a lot of damages in the first 500 nm, we may wonder whether these surface implantation dislocations either help, limit or are neutral regarding the strain transition zone. If independent, this would confirm that the dislocation generation is strain driven.

IV.2.2 LPE samples: applied research oriented

As already stated, the reference process to produce IR photodetectors is the Liquid Phase Epitaxy (LPE). As LPE requires a much higher substrate temperature than MBE during growth, LPE samples always possess a graded compositional interface originating from thermally induced Zn and Hg exo-diffusion during growth, even in the absence of subsequent annealing. Therefore, critical thickness cannot be directly measured on LPE sample in contrast with MBE samples. Moreover, making a photodetector always requires implantation and subsequent annealing which will add to the graded interface, a thermally induced compositional mixing. Nevertheless, measuring until which depth, the compositional strain deduced from SIMS measurements is indistinguishable from strain measured by μ Laue, enables to estimate the potentially defect-free zone extension. Following the defect-free zone, is a transition zone where strain relaxes to finally reach an unstrained zone, a transition we have attributed to dislocation generation which are really to be avoided as much as possible since they cause recombinations outside of the p-n junction. Therefore, being able to measure both the potentially defect-free and transition zone extensions would enable us to check whether any processes, sample treatment or elaboration technique (duration of annealing, temperature, doping ...) tends to extend or shrink those two zones thus providing very precious informations: LPE sample study is clearly applied research oriented.

The dislocation zone could be specifically studied since the expected created dislocation are misfit dislocations ([61] and [62]), and more precisely dislocations with Burgers vector at 60° [63]. Therefore, we expect — as for As implantation III.2.3 — a characteristic difference in intensity evolution between weak and strong diffraction peak and finally we expect to determine from the strong/weak ratio, the local misfit dislocation density with depth. And it will be very interesting to compare such density with the 10^{4-5} cm^{-2} density of emerging dislocations measured using the etch pit technique.

Table 12 compares evolution of strong and weak peak before and after annealing on the $4 \mu\text{m}$ situated underneath the surface (this includes dislocation and relaxed zone of the epi-layer). Before annealing, the weak and strong integral signal repartition clearly look similar. Like with As-implanted sample (see table 10), the diffraction signal clearly goes down to background level in a 500 nm deep and $8 \mu\text{m}$ wide zone situated at the centre of the image, thus perfectly localising the Sb implantation zone. This indicates that the epi-layer is so badly damaged by implantation that diffraction intensity becomes zero and that zone is $250\text{-}500 \text{ nm}$ thick, perfectly corresponding to expected penetration length of 360 keV Sb ions!

In fact, we may even have two sub-zones in the damaged region that would need a separated treatment. Indeed, figure 48 presents the Bright-field STEM image of Arsenic implanted sample at the same $2 \cdot 10^{14} \text{ at.cm}^{-2}$ dose and energy which shows that two different types of dislocation are present: from 0 to 250 nm , we get long dislocation lines while short dislocation loops are seen in the range $250\text{-}450 \text{ nm}$. Knowing that the projected range of implantation at 360 keV for As is 150 nm and only 90 nm for Sb, we may expect that the two sub-zones for Sb are respectively $0\text{-}150 \text{ nm}$ and $150\text{-}250 \text{ nm}$. With our 250 nm resolution, we cannot resolve these two sub-zones for Sb-implanted, but we may be able to do so for As-implanted ones.

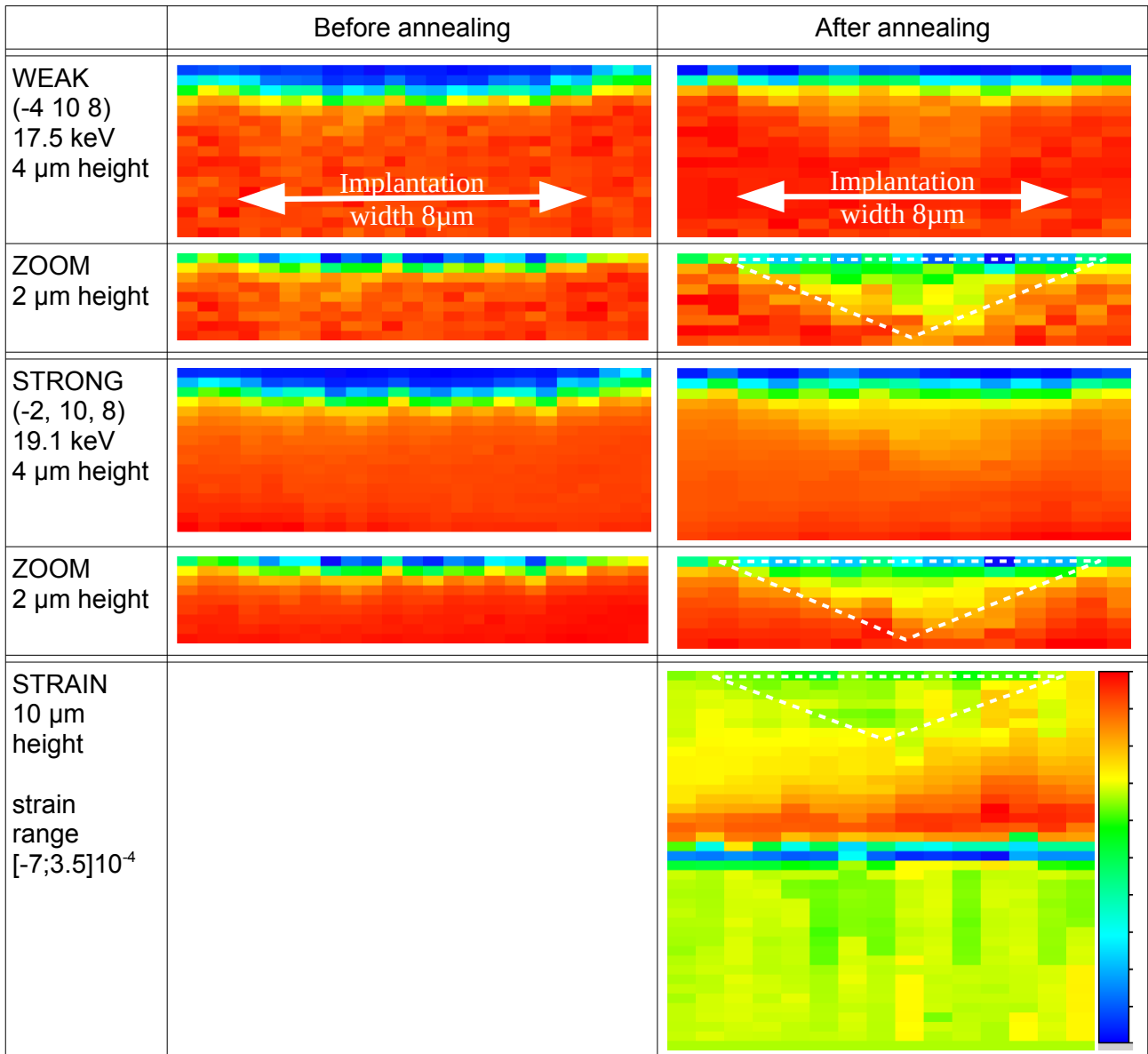


Table 12: Comparison of strong and weak peak intensity repartitions in the 4 μm surface of the epi-layer, both in the as-implanted and annealed case. The 2D strain mesh is also presented.

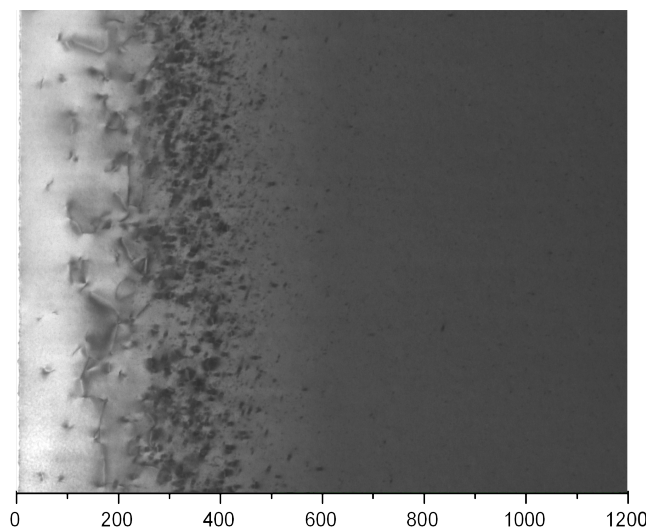


Figure 48: Bright-Field STEM images obtained along the $\langle 110 \rangle$ zone axis of As-implanted sample at 360 keV with a $2 \cdot 10^{14} \text{As.cm}^{-2}$ dose.

When taking a zoom on the 2 μm zone situated underneath the surface (see zoom zones of table 12), there is indeed a difference in the signal repartition between weak and strong peaks. But this difference is small with Sb while it was large with As (see table 10). We think this point must be looked into more precisely using no bigger than 100 nm steps for Sb since the damaged zone extension is of 250 nm depth only: we could take advantage of our newly installed piezo cube that enables us to take nanometric steps and show a more detailed evolution despite our beam spot of 500 nm remains quite large compared to 100 nm. And once the ESRF has been upgraded (foreseen restarting date is September 2020), we may expect a microbeam down to $\varnothing 100$ nm so that this study would become more easily feasible.

After annealing, we observe a restoration of the diffraction signal in the implanted zone but this restoration is quite incomplete since the implanted zone is still visible. This clearly contrasts with As where after annealing, the epi-layer was completely cured. We think this may be linked to the apparition of nanometric voids in the last 500 nm epi-layer with a 10 times larger density for Sb ($65.5 \mu\text{m}^{-2}$) than for As ($6.4 \mu\text{m}^{-2}$) [48], see table 13.

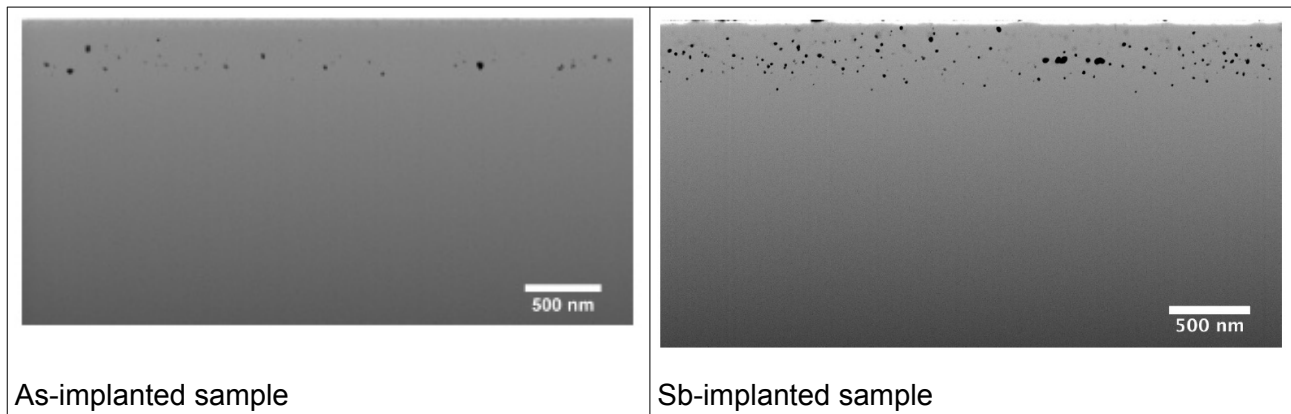


Table 13: FIB-3D tomography image for As and Sb implanted samples at the same $2 \cdot 10^{15}$ dose at 360 keV after 1 H annealing showing voids in black.

Finally, we specifically observe for the annealed sample — thanks to the zoom of table 12 — that a triangular zone appears (shown in dashed white line) where we observe a 35% reduced diffraction intensity that exists both of weak and strong peak. This is quite a non-expected phenomenon since it seems to be anisotropic and to the author's knowledge, it is an unknown phenomenon. We also see such an effect on the 2D strain repartition as illustrated. Therefore, if we are first able to reproduce and confirm this effect, this would be worth developing a new axis of research. Another important aspect here is that this phenomenon is width limited by the implantation: despite SIMS, RBS and MEIS have much better adapted depth resolution in the 1 nm range, their millimetric beam size is a redhibitory drawback here because it would require to make an as-large implantation, and we would probably loose the width limiting phenomena. This probably explains why this phenomenon has never been seen before. To confirm this effect, we may benefit from LETI's recently developed high resolution 3D-SIMS. This apparatus uses oxygen and cesium etching beam which are spatially confined to a $\varnothing 1 \mu\text{m}$ beam spot. We are currently mapping our sample on a $15 \times 15 \mu\text{m}^2$ surface and therefore if the sensitivity is good enough, we should be able to determine the 3D spatial repartition of all chemicals elements. Hopefully, we will be able to record good quality data which will be meaningfully compared to the μLaue ones to try to understand the nature and the origin of this triangular zone.

CONCLUSION

In chapter I which covers the 1999→2012 period, we focused on phase-change materials, which are key technological materials since they constitute the active layer of yesterdays CD and DVD, present days Blu-ray and future days Super-RENS disks or PRAM. We have been investigating — thanks to the emblematic synchrotron EXAFS technique — the evolution of the local atomic environment when GeTe and GST are commuted between their amorphous and crystalline phase. As GeTe and GST are fast switching PCMs, we could logically expect a similar local atomic environment between crystalline and amorphous phase, the most favourable case between a simple density change. Surprisingly, for both materials, we found that the amorphous↔crystalline cycle is not a simple density change since Ge-Ge bonds are only present in the amorphous phase: disappearance of Ge-Ge bonds is something costly in energy since Ge-Ge bonds must first be broken (Ge-Ge are the most stable bonds), and costly in time since Ge atoms must diffuse through the surrounding [Sb|Te] shell. As GST contains a smaller percentage of Ge than GeTe, amorphous↔crystalline cycle requires less Ge diffusion, and we believe this explains why GST commutes faster than GeTe. Therefore, adding Sb to binary GeTe to make GST does not accelerate crystallisation but rather prevents the formation of speed limiting Ge-Ge bonds.

Chapter II was devoted to the μ Laue setup that enabled us to conduct submicronic Laue diffraction studies, another emblematic synchrotron technique. μ Laue was used in chapter III (which covers the 2006→2018 period) on HgCdTe, another key technological material since it is the active part of IR pixel of high-performance photodetectors. We have studied the four main technological processes applied to raw material in order to obtain a pixelized photodetector. The first process creates a p-n junction using As dopant implantation and μ Laue measures implantation damages through diffraction intensity weakening. Moreover, by comparing weak and strong diffraction peak intensity weakening, we are specifically sensitive to misfit dislocations. The second process uses dry-etching to create individual pixels: μ Laue showed that this process has no noticeable impact on either local strain or crystalline orientation. By contrast, local strain builds up inside pixels and disorientation appears at pixel side because of surface passivation which is the third process. And finally, strain and disorientation are highly reduced thanks to annealing (the fourth process) but did not completely disappear, being concentrated on the top surface and low corner of pixel side. If Sb instead of As is implanted, we observed that after annealing, a strange triangular zone corresponding to the implantation width exists on the top surface of pixels, a zone where diffraction intensities stay weakened and strain is affected. This unknown width-limited phenomenon induced by implantation would clearly constitute a nice Ph-D research subject (chapter IV).

Speaking from a more personal point of view, I would say — in an analogy with key technological material — that I found in fundamental research a key research material which is the astonishment! Indeed, it is surprising that the fastest PCM doesn't possess the same local structure between amorphous and crystalline phase! It seems counter-intuitive that the crystalline phase is made of fully randomised rigid blocks, a characteristic we would rather expect for the amorphous phase! It is an unforeseen asset that the difference between strong and weak diffraction intensity weakening correlates to the fraction of dislocations that are misfit ones. And we unexpectedly observed that MBE layers present a strain that is not constant on their whole thickness while LPE samples — despite their graded interface — present a constant strain.

To conclude, I must say that among all scientific results obtained and some shown here, those that offer me astonishment generate a lot of curiosity thus providing me with the necessary motivation to work until reaching a satisfying explanation. Finally, they constitute the Ariadne's thread of my professional career and are the foundation of my taste for fundamental research.

Let me thank my family who has always been caring and supportive during my high degree studies and helped me became aware of my appetite for understanding, the CEA for providing the means to pursue a rich scientific career starting with my Ph-D under supervision of Jean-Paul V. and Jean-Pierre M., to my colleagues (too numerous to cite them all!) Denis J., Alain F., Frédéric G., Olivier U., Jean-Louis H., Olivier P., François R., Bérange H., Henri M., Joël C., Alexander K., Bruno D., Katharina L., Philippe B. and Aymeric T. with whom it was so interesting and exciting to work, and finally to my children whose constant questionings forced me to clarify my understanding in order to be able to answer them and therefore transmit to others.

Bibliography

- [1] B. Hyot, 'Étude physique et théorique des matériaux à changement de phase pour disques optiques', phdthesis, Grenoble INPG, 2001.
- [2] J.-C. Bastien, 'Étude des matériaux à changement de phase pour application dans le domaine des PCRAM : verres infrarouges pour l'optique spatiale', phdthesis, Université Rennes 1, 2011.
- [3] A. Bastard, 'Analyse théorique et physique de nouveaux matériaux à base de chalcogénures convenant aux Mémoires à Changements de Phases', phdthesis, Grenoble, 2012.
- [4] S. R. Ovshinsky, 'Electrical control device and process', 3052830, 04-Sep-1962.
- [5] S. R. Ovshinsky and H. Fritzsche, 'Amorphous semiconductors for switching, memory, and imaging applications', *IEEE Trans. Electron Devices*, vol. 20, no. 2, pp. 91–105, Feb. 1973.
- [6] M. Chen, K. A. Rubin, and R. W. Barton, 'Compound materials for reversible, phase change optical data storage', *Appl. Phys. Lett.*, vol. 49, no. 9, pp. 502–504, Sep. 1986.
- [7] S. Raoux, W. Welnic, and D. Ielmini, 'Phase Change Materials and Their Application to Nonvolatile Memories', *Chem. Rev.*, vol. 110, no. 1, pp. 240–267, Jan. 2010.
- [8] P. Bright, 'Intel's first Optane SSD: 375GB that you can also use as RAM', *Ars Technica*, 19-Mar-2017. [Online]. Available: <https://arstechnica.com/information-technology/2017/03/intels-first-optane-ssd-375gb-that-you-can-also-use-as-ram/>. [Accessed: 25-Apr-2018].
- [9] B. Tallis, 'Intel Launches Optane Memory M.2 Cache SSDs For Consumer Market', 2017. [Online]. Available: <https://www.anandtech.com/show/11227/intel-launches-optane-memory-m2-cache-ssds-for-client-market>. [Accessed: 25-Apr-2018].
- [10] D. C. Koningsberger, 'X-Ray Absorption: Principles, Applications, Techniques of EXAFS, SEXAFS and XANES', *Wiley.com*, 1987. .
- [11] H. Winter, 'Hollow atom spectroscopy', *Phys. Scr.*, vol. 1997, no. T72, p. 18, 1997.
- [12] X. Biquard *et al.*, 'Local Structure and Valence State of Mn in Ga_{1-x}Mn_xN Epilayers', *J. Supercond.*, vol. 16, no. 1, pp. 127–129, Feb. 2003.
- [13] B. Ravel and M. Newville, 'ATHENA, ARTEMIS, HEPHAESTUS: data analysis for X-ray absorption spectroscopy using IFEFFIT', *J. Synchrotron Radiat.*, vol. 12, no. 4, pp. 537–541, Jul. 2005.
- [14] M. Newville, 'IFEFFIT : interactive XAFS analysis and FEFF fitting', *J. Synchrotron Radiat.*, vol. 8, no. 2, pp. 322–324, Mar. 2001.
- [15] M. Wuttig and N. Yamada, 'Phase-change materials for rewriteable data storage', *Nat. Mater.*, vol. 6, no. 12, p. 1004, Dec. 2007.
- [16] T. Matsunaga *et al.*, 'From local structure to nanosecond recrystallization dynamics in AgInSbTe phase-change materials', *Nat. Mater.*, vol. 10, no. 2, pp. 129–134, Feb. 2011.
- [17] Y. Maeda, H. Andoh, I. Ikuta, and H. Minemura, 'Reversible phase change optical data storage in InSbTe alloy films', *J. Appl. Phys.*, vol. 64, no. 4, pp. 1715–1719, Aug. 1988.
- [18] E. Huber and E. E. Marinero, 'Laser-induced crystallization of amorphous GeTe: A time-resolved study', *Phys. Rev. B*, vol. 36, no. 3, pp. 1595–1604, Jul. 1987.
- [19] B. Hyot, X. Biquard, and L. Poupinet, 'Local structure of amorphous and crystalline GeTe and GeSbTe', presented at the EPCOS 2001, Säntis in Switzerland, 2001.
- [20] E. Gourvest *et al.*, 'Evidence of Germanium precipitation in phase-change Ge_{1-x}Te_x thin films by Raman scattering', *Appl. Phys. Lett.*, vol. 95, no. 3, p. 031908, Jul. 2009.
- [21] J.-Y. Raty, J.-P. Gaspard, C. Bichara, C. Bergman, R. Bellissent, and R. Ceolin, 'Re-entrant peierls distortion in IV–VI compounds', *Phys. B Condens. Matter*, vol. 276–278, pp. 473–474, Mar. 2000.
- [22] M. Delheusy, J. Y. Raty, R. Detemple, W. Welnic, M. Wuttig, and J.-P. Gaspard, 'Structure of liquid Te-based alloys used in rewritable DVDs', *Phys. B Condens. Matter*, vol. 350, no. 1, Supplement, pp. E1055–E1057, Jul. 2004.
- [23] A. Schlieper, Y. Feutelais, S. G. Fries, B. Legendre, and R. Blachnik, 'Thermodynamic evaluation of the Germanium — Tellurium system', *Calphad*, vol. 23, no. 1, pp. 1–18, Mar. 1999.
- [24] H. Okamoto, 'Ge-Te (Germanium-Tellurium)', *J. Phase Equilibria*, vol. 21, no. 5, p. 496, Sep. 2000.
- [25] T. Chattopadhyay, J. X. Boucherle, and H. G. vonSchnering, 'Neutron diffraction study on the structural phase transition in GeTe', *J. Phys. C Solid State Phys.*, vol. 20, no. 10, p. 1431, 1987.
- [26] T. Nonaka, G. Ohbayashi, Y. Toriumi, Y. Mori, and H. Hashimoto, 'Crystal structure of GeTe and Ge₂Sb₂Te₅ meta-stable phase', *Thin Solid Films*, vol. 370, no. 1, pp. 258–261, Jul. 2000.

- [27] P. Fons *et al.*, ‘Phase transition in crystalline GeTe: Pitfalls of averaging effects’, *Phys. Rev. B*, vol. 82, no. 15, p. 155209, Oct. 2010.
- [28] T. Matsunaga, P. Fons, A. V. Kolobov, J. Tominaga, and N. Yamada, ‘The order-disorder transition in GeTe: Views from different length-scales’, *Appl. Phys. Lett.*, vol. 99, no. 23, p. 231907, Dec. 2011.
- [29] S. Hosokawa, N. Happo, and K. Hayashi, ‘Reconciling the Pauling bond length picture and Vegard’s law in a mixed crystal: An x-ray fluorescence holographic study’, *Phys. Rev. B*, vol. 80, no. 13, p. 134123, Oct. 2009.
- [30] D. A. Baker, M. A. Paesler, G. Lucovsky, S. C. Agarwal, and P. C. Taylor, ‘Application of Bond Constraint Theory to the Switchable Optical Memory Material Ge₂Sb₂Te₅’, *Phys. Rev. Lett.*, vol. 96, no. 25, p. 255501, Jun. 2006.
- [31] A. V. Kolobov, P. Fons, A. I. Frenkel, A. L. Ankudinov, J. Tominaga, and T. Uruga, ‘Understanding the phase-change mechanism of rewritable optical media’, *Nat. Mater.*, vol. 3, no. 10, pp. 703–708, Oct. 2004.
- [32] N. Yamada and T. Matsunaga, ‘Structure of laser-crystallized Ge₂Sb_{2+x}Te₅ sputtered thin films for use in optical memory’, *J. Appl. Phys.*, vol. 88, no. 12, pp. 7020–7028, Nov. 2000.
- [33] A. V. Kolobov, J. Tominaga, P. Fons, and T. Uruga, ‘Local structure of crystallized GeTe films’, *Appl. Phys. Lett.*, vol. 82, no. 3, pp. 382–384, Jan. 2003.
- [34] K. Ohara *et al.*, ‘The Roles of the Ge-Te Core Network and the Sb-Te Pseudo Network During Rapid Nucleation-Dominated Crystallization of Amorphous Ge₂Sb₂Te₅’, *Adv. Funct. Mater.*, vol. 22, no. 11, pp. 2251–2257, Jun. 2012.
- [35] V. L. Deringer, R. Dronskowski, and M. Wuttig, ‘Microscopic Complexity in Phase-Change Materials and its Role for Applications’, *Adv. Funct. Mater.*, vol. 25, no. 40, pp. 6343–6359, Oct. 2015.
- [36] M. Jafari, L. J. Guo, and M. Rais-Zadeh, ‘An ultra-fast optical shutter exploiting total light absorption in a phase change material’, in *Optical Components and Materials XIV*, 2017, vol. 10100, p. 101000I.
- [37] B. Chen, G. H. ten Brink, G. Palasantzas, and B. J. Kooi, ‘Crystallization Kinetics of GeSbTe Phase-Change Nanoparticles Resolved by Ultrafast Calorimetry’, *J. Phys. Chem. C*, vol. 121, no. 15, pp. 8569–8578, Apr. 2017.
- [38] P. S. Branicio, K. Bai, H. Ramanarayan, D. T. Wu, M. B. Sullivan, and D. J. Srolovitz, ‘Atomistic insights into the nanosecond long amorphization and crystallization cycle of nanoscale Ge₂Sb₂Te₅: an ab initio molecular dynamics study’, *Phys. Rev. Mater.*, vol. 2, no. 4, p. 043401, Apr. 2018.
- [39] B. Hyot, A. Bernard, P. Desre, and X. Biquard, ‘Super-resolution optical recording medium’, European Patent EP1978517, 12-May-2010.
- [40] D. Hepper *et al.*, ‘4GOOD - Technology and Prototype for a 4th-Generation Omni-Purpose Optical Disc System’, in *2008 Digest of Technical Papers - International Conference on Consumer Electronics*, 2008, pp. 1–2.
- [41] O. Ulrich *et al.*, ‘A new white beam x-ray microdiffraction setup on the BM32 beamline at the European Synchrotron Radiation Facility’, *Rev. Sci. Instrum.*, vol. 82, no. 3, p. 033908, Mar. 2011.
- [42] N. Tamura, ‘XMAS: A Versatile Tool for Analyzing Synchrotron X-ray Microdiffraction Data’, in *Strain and Dislocation Gradients from Diffraction*, IMPERIAL COLLEGE PRESS, 2014, pp. 125–155.
- [43] O. Sicardy, F. Rieutord, and J. S. Micha, ‘Macro contraintes et micro déformations d’interconnexions en cuivre pour circuits intégrés’, in *17ème congrès Français de mécanique*, Troyes, 2005.
- [44] O. Sicardy *et al.*, ‘Détermination de contraintes résiduelles locales par micro-diffraction en faisceau blanc et monochromatique sur la ligne CRG IF-BM32 de l’ESRF’, in *18ème Congrès Français de Mécanique*, Grenoble, 2007.
- [45] 2.0 ITRS, ‘International Technology Roadmap for Semiconductors: More Moore’. 2015.
- [46] A. Tuaz, *Investigations structurales haute-résolution de photodiodes infrarouges de nouvelle génération*. Grenoble Alpes, 2017.
- [47] A. Rogalski, ‘HgCdTe infrared detector material: history, status and outlook’, *Rep. Prog. Phys.*, vol. 68, no. 10, p. 2267, 2005.
- [48] C. Lobre, ‘Compréhension des mécanismes de dopage arsenic de CdHgTe par implantation ionique’, phdthesis, Grenoble, Grenoble, 2014.
- [49] B. Delacourt *et al.*, ‘Temperature and Injection Dependence of Photoluminescence Decay in Midwave Infrared HgCdTe’, *J. Electron. Mater.*, vol. 46, no. 12, pp. 6817–6828, 2017.
- [50] G. Destefanis and J. P. Chamonal, ‘Large improvement in HgCdTe photovoltaic detector performances at LETI’, *J. Electron. Mater.*, vol. 22, no. 8, pp. 1027–1032, Aug. 1993.

- [51] K. Jówickowski and A. Rogalski, 'Effect of dislocations on performance of LWIR HgCdTe photodiodes', *J. Electron. Mater.*, vol. 29, no. 6, pp. 736–741, Jun. 2000.
- [52] M. A. Kinch, F. Aqariden, D. Chandra, P.-K. Liao, H. F. Schaake, and H. D. Shih, 'Minority carrier lifetime in p-HgCdTe', *J. Electron. Mater.*, vol. 34, no. 6, pp. 880–884, Jun. 2005.
- [53] P. Ballet, X. Baudry, B. Polge, D. Brellier, J. Merlin, and P. Gergaud, 'Strain Determination in Quasi-Lattice-Matched LWIR HgCdTe/CdZnTe Layers', *J. Electron. Mater.*, vol. 42, no. 11, pp. 3133–3137, Nov. 2013.
- [54] T. Skauli and T. Colin, 'Accurate determination of the lattice constant of molecular beam epitaxial CdHgTe', *J. Cryst. Growth*, vol. 222, no. 4, pp. 719–725, Feb. 2001.
- [55] J. S. Micha, 'LaueTools download at SourceForge.net', 2018. [Online]. Available: <https://sourceforge.net/projects/lauetools/>. [Accessed: 13-Jun-2018].
- [56] S. Brückner, 'Estimation of the background in powder diffraction patterns through a robust smoothing procedure', *J. Appl. Crystallogr.*, vol. 33, no. 3, pp. 977–979, Jun. 2000.
- [57] H. Schulte-Schrepping and W. Drube, 'Properties of a detuned non-dispersive double crystal monochromator', *Nucl. Instrum. Methods Phys. Res. Sect. Accel. Spectrometers Detect. Assoc. Equip.*, vol. 467–468, pp. 396–399, Jul. 2001.
- [58] J. W. Matthews, Ed., 'CONTENTS OF PART B', in *Epitaxial Growth*, Academic Press, 1975, p. xii.
- [59] O. Robach *et al.*, 'A tunable multicolour 'rainbow' filter for improved stress and dislocation density field mapping in polycrystals using X-ray Laue microdiffraction', *Acta Crystallogr. A*, vol. 69, no. 2, pp. 164–170, Mar. 2013.
- [60] O. Robach, J.-S. Micha, O. Ulrich, and P. Gergaud, 'Full local elastic strain tensor from Laue microdiffraction: simultaneous Laue pattern and spot energy measurement', *J. Appl. Crystallogr.*, vol. 44, no. 4, pp. 688–696, Aug. 2011.
- [61] M. A. Berding, W. D. Nix, D. R. Rhiger, S. Sen, and A. Sher, 'Critical thickness in the HgCdTe/CdZnTe system', *J. Electron. Mater.*, vol. 29, no. 6, pp. 676–679, Jun. 2000.
- [62] J. H. Basson and H. Booyens, 'The introduction of misfit dislocations in HgCdTe epitaxial layers', *Phys. Status Solidi A*, vol. 80, no. 2, pp. 663–668.
- [63] M. Yoshikawa, 'Dislocations in Hg_{1-x}CdxTe/Cd_{1-z}ZnzTe epilayers grown by liquid phase epitaxy', *J. Appl. Phys.*, vol. 63, no. 5, pp. 1533–1540, Mar. 1988.
- [64] V. M. Glazov, A. A. Aivazov, and S. N. Kol'tsov, 'InSb', *Sov Phys Semicond*, vol. 14, no. 8, p. 909, 1980.
- [65] R. Beneyton and G. Hollinger, 'Sur l'incorporation du thalium dans une matrice III-V: Préparation de GaTIAs et InTIAs par épitaxie par jets moléculaires', phdthesis, Ecole centrale de Lyon, Ecully, 2004.

Index of Tables

Table 1: Data adjustment of amorphous GeTe at Te K-edge. r-factor of fit indicates a good quality data adjustment. ΔE_0 range of value includes 0 eV, which is perfectly reasonable for neutral Te. page 9
Table 2: Data adjustment of amorphous GeTe at Ge K-edge. r-factor of fit indicates a good quality data adjustment. ΔE_0 overall value of 1.29 ± 2.11 eV is coherent with neutral Ge. page 10
Table 3: Short-range ordering evolution of GeTe during amorphous \leftrightarrow crystalline cycle page 13
Table 4: Amorphous GST chemical environment.** denotes large data uncertainty page 13
Table 5: Chemical environment of an amorphous Sb-[Sb Te] phase present in GST sample page 14
Table 6: Short-range ordering evolution of GST during amorphous \leftrightarrow crystalline cycle page 15
Table 7: Diffraction studies results on 20 nm InSb layer sandwiched between ZnS-SiO ₂ layers. page 17
Table 8: Diffraction studies results on 20 nm InSb layer sandwiched between ZrO ₂ layers. page 18
Table 9: IR application domains page 26
Table 10: Comparison between diffraction intensity repartition for as-implanted and annealed samples. For each sample, we compare the most intense weak reflection with the corresponding strongest one that is closest in energy to avoid any penetration length distortion. Intensity is colored coded from blue to red as shown at the extreme right and the localisation of implanted pixels is shown on the left. X-ray beam was raster scan every 0.25 μm horizontally and 1 μm vertically. page 29
Table 11: Comparison between HRXRD measurements and our method on our three reference samples page 37
Table 12: Comparison of strong and weak peak intensity repartitions in the 4 μm surface of the epi-layer, both in the as-implanted and annealed case. The 2D strain mesh is also presented. page 48
Table 13: FIB-3D tomography image for As and Sb implanted samples at the same $2 \cdot 10^{15}$ dose at 360 keV after 1 H annealing showing voids in black. page 49

Illustration Index

- Figure 1: Example of recorded EXAFS spectra (K-edge of Mn) page 3
- Figure 2: The radar effect: once incident photon (yellow) is absorbed, ejected photo-electron wave (red) is backscattered (blue) by neighbouring atoms and interferes with emission thus modulating the absorption. page 3
- Figure 3: Recorded EXAFS spectra (here 2% Mn dopant inside GaN) along with the modulus of its FT. Comparison of experiment with data simulation is also provided page 4
- Figure 4: PCM commutation mechanism principle page 6
- Figure 5: Ternary phase diagram depicting different phase-change alloys, discovery year and use in different optical storage products page 7
- Figure 6: Comparison of optics, recording densities, capacities and disk structures used for CD, DVD and BD. Recording density increased by a factor of 7 going from CD to DVD (2.8 Gb/in²) and a factor 5 going to BD (14.7 Gb/in²). Active PCM layer is 20 nm thick. page 7
- Figure 7: Data adjustment (blue) of amorphous GeTe EXAFS (red) at the Te K-edge page 8
- Figure 8: Calculated backscattering amplitude and phase-shift of Ge and Te as backscatterer for Te. For a meaningful comparison, the same 3 Å distance was chosen for the two backscatterers. page 9
- Figure 9: Check of the data adjustment (blue) of amorphous GeTe back-transformed EXAFS (green, $R \in [1.8-3.9] \text{Å}$) at Ge K-edge. Original signal (dashed) displayed for comparison. page 9
- Figure 10: Ge-Te phase diagram with detailed view around congruent Ge₅₀Te₅₀ stoichiometry page 11
- Figure 11: Left: α -GeTe (RT) rhombohedral unit cell with rhombohedral parameter (subscript R) and corresponding hexagonal ones (subscript H). Right: β -GeTe (HT) classical cubic four cfc unit-cell structure, with corresponding rhombohedral unit cell in green. page 11
- Figure 12: Data adjustment of crystalline GeTe EXAFS signal collected at the Ge K-edge with α -GeTe crystal: first neighbours are 3 Te at 2.84 Å + 3 Te at 3.16 Å. page 12
- Figure 13: Comparison of GeTe distance as measured directly by EXAFS [27] and as inferred from neutron diffraction [25]. Both methods see the same average distance evolution with temperature, but diffraction wrongly sees short and long bond length becoming the same while EXAFS shows they remain different. page 12
- Figure 14: Data adjustment on the high-k part of the EXAFS of GST at the Sb K-edge. page 14
- Figure 15: Left: evolution of InSb carrier density near fusion point from [64]. Right: improvement of the CNR with the number of reads realised at optimum power page 16
- Figure 16: The super-resolution effect: using an optical non-linear active InSb layer, central zone with modified optical properties boosts optical resolution beyond the resolution limit page 16
- Figure 17: Crystallite perpendicular (left) and radial (right) sizes deduced from the integral width of [111] diffraction peaks. Sample is made of 50 nm InSb sandwiched between ZnS-SiO₂ layers. Crystallite sizes increase with the number of read, perpendicular and radial sizes are found equal at $\pm 10\%$ page 17
- Figure 18: Demonstration of a super-RENS single-face Blu-ray disc of 50Gb capacity in 2009. page 18

Figure 19: Principe of a μ Laue experiment page 19
Figure 20: Diffraction image of 1 μ m wide interconnect. Left insert shows a zoom of the central part: Si elongated spots are evidenced with light magenta and Cu round spots with black. page 21
Figure 21: At high 21 keV energy, we observe that Ge diffraction spot (right) stays nicely round while Si spot (left) is highly elongated. page 21
Figure 22: The presence of a highly intense Si spot near the Cu spot makes its position artificially drift towards the Si spot, an artefact suppressed when a reference Si image is subtracted first page 22
Figure 23: Normal orientation of the grains constituting a 1 μ m wide and 60 μ m long copper interconnect line (not represented to scale). Mapping was conducted every 2 μ m. page 23
Figure 24: Von Mises stress of individual grains of the 1 μ m wide interconnect line page 23
Figure 25: Normal orientation of the grains constituting a 250x260nm ² interconnect line page 23
Figure 26: Views of the updated μ Laue setup with X-ray beam coming from the right. The left part shows an overall view while the right part shows a detailed view of the KB system. Both perpendicular KB mirrors are mounted on ultra-precise encoded hexapods. page 24
Figure 27: Scan of a 2 μ m wide interconnection Cu line to evaluate our white X-ray beam size. Interconnect line was considered as a boxcar function while X-ray beam was modelled as a Gaussian. Data adjustment gives a 2.08 μ m wide interconnect line with a beam FWHM of 190 nm in horizontal and 285 nm in vertical with a more than 50 signal-to-noise ratio. page 25
Figure 28: IR atmospheric transmission windows and corresponding absorption molecules page 26
Figure 29: Band gap and cut-off wavelength of various semiconductors and their alloys as a function of lattice parameter (from [65]) page 27
Figure 30: Four top-left images show FIB extraction of a slice containing two pixels and its welding on a dedicated support. Bottom-left image shows implanted spots with contrast obtained through a chemical revelation of the implantation-induced extended defects. Right: X-ray beam trajectories inside sample showing zones where only implanted or not-implanted material is probed. page 28
Figure 31: ZincBlende structure of the ternary alloy Hg _{1-x} Cd _x Te page 28
Figure 32: Comparison between strong and weak reflection for the pixel zone of both samples. Density of displaced atoms is also represented against the right scale. Insert: SIMS measurements of the concentration of cations Hg and Cd with depth page 30
Figure 33: Hybrid IR focal plane array with independently optimised signal detection and readout using the indium bump technique (taken from [47]) page 31
Figure 34: Effect of moving away CCD from sample on the same diffraction peak. With a 4 times better resolution, the asymmetric repartition of the peak's intensity becomes obvious page 32
Figure 35: Comparison of the same image with the same logarithmic intensity scale before (left) and after (right) background removable thanks to the 2D generalised Brückner algorithm: background level estimated from signal between peaks goes from 66 initially down to 5.5! page 33
Figure 36: Attenuation length of X-ray in substrate (Cd _{96%} Zn _{4%} Te) or layer (Hg _{70%} Cd _{30%} Te) as a function of energy. Layer shows three drop-downs reflecting L _I , L _{II} and L _{III} absorption edge of Hg. page 33

Figure 37: 2D raster scan shown in red dots on a 4 μm deep trench realised on a 6.5 μm HgCdTe layer grown on the CdZnTe substrate. The trench lower corner is rounded because the rotating 35° ion milling is partially shadowed by the deposited protection resin.

..... page 34

Figure 38: Evolution on reference measurements of the 10 recorded diffraction peaks average positions (x,y) and rotation with time on a typical 10 h long experiment (sample 16703-F). Smooth fits are used to compensate these drifts: difference with values is used to estimate our individual diffraction peak fitting precision, which is found to be $\pm 1/20^{\text{th}}$ and $\pm 1/10^{\text{th}}$ of pixel along x and y.

..... page 35

Figure 39: Bi-axial strain represented in the plane formed by the Z axis and the diffraction direction vector. The unit cell of layer (red) is stretched along z from c to c' compared to the substrate one (in black), leading to a diffraction plane angle that changes from α to α' .

..... page 36

Figure 40: Evolution of strain as a function of depth as determined by μLaue (red). Comparison with expected strain from local composition of quaternary HgCdZnTe as determined by SIMS. Hg fluorescence shows interface position.

..... page 37

Figure 41: Origin of the position difference along y between layer and substrate for sample 27937-D

..... page 39

Figure 42: Diffraction peaks splitted into direct (green) and back-diffracted (red) categories, the output intensity being represented by line thickness. X-ray beam penetration length is represented with a blue dashed line.

..... page 40

Figure 43: Comparison of the 2D repartition of the local (xz) orientation (upper line, rotation angle scale shown on the right) and local strain (lower line, strain scale on the right) of our three samples 16703-G, 16703-A and 16703-F to individually assess the effect of the three main technological processes of etching, passivation and annealing.

..... page 41

Figure 44: Main graph shows a strain measurement comparison 12 μm inside non-etched area for our three samples. The insert compares it to a closer 2 μm inside non-etched area for the 16703-F

..... page 42

Figure 45: Effect of the diamond crystal (right) on the incoming X-ray beam energy spectrum (left)

..... page 44

Figure 46: The successive zones constituting the Sb-doped annealed sample 27937-D

..... page 45

Figure 47: strain evolution as a function of depth for a 4.5 μm thick HgCdTe layer deposited by MBE, without any further processing (neither annealing nor implantation). The absence of compositional mixing at the interface enables to see very clearly the defect-free zone extension.

..... page 46

Figure 48: Bright-Field STEM images obtained along the $\langle 110 \rangle$ zone axis of As-implanted sample at 360 keV with a $2 \cdot 10^{14} \text{As.cm}^{-2}$ dose.

..... page 48